A&A 476, 1161–1178 (2007)
DOI: 10.1051/0004-6361:20078179

Astronomy & Astrophysics

Star formation in M 33: *Spitzer* photometry of discrete sources⋆

S. Verley[1], L. K. Hunt[2], E. Corbelli[1], and C. Giovanardi[1]

[1] Osservatorio Astrofisico di Arcetri, Largo E. Fermi 5, 50125 Firenze, Italy
e-mail: [simon;edvige;giova]@arcetri.astro.it
[2] INAF - Istituto di Radioastronomia-Sezione Firenze, Largo E. Fermi 5, 50125 Firenze, Italy
e-mail: hunt@arcetri.astro.it

Received 28 June 2007 / Accepted 12 September 2007

ABSTRACT

Aims. Combining the relative vicinity of the Local Group spiral galaxy M 33 with the *Spitzer* images, we investigate the properties of infrared (IR) emission sites and assess the reliability of the IR emission as a star formation tracer.
Methods. The mid- and far-IR emission of M 33 was obtained from IRAC and MIPS images from the *Spitzer* archive. We compared the photometric results for several samples of three known types of discrete sources (HII regions, supernovae remnants and planetary nebulae) with theoretical diagnostic diagrams, and derived the spectral energy distribution (from 3.6 to 24 μm) of each type of object. Moreover, we generated a catalogue of 24 μm sources and inferred their nature from the observed and theoretical colours of the known type sources. We estimated the star formation rate in M 33 both globally and locally, from the IR emission and from the Hα emission line.
Results. The colours of the typical IR emissions of HII regions, supernovae remnants and planetary nebulae are continuous among the different samples, with overlapping regions in the diagnostic diagrams. The comparison between the model results and the colours of HII regions indicates a dusty envelope at relatively high temperatures ~600 K, and moderate extinction $A_V \lesssim 10$. The 24 μm sources IR colours follow the regions observationally defined by the three classes of known objects but the majority of them represent HII regions. The derived total IR luminosity function is in fact very similar to the HII luminosity function observed in the Milky Way and in other late type spirals. Even though our completeness limit is 5×10^{37} erg s^{-1}, in low density regions we are able to detect sources five times fainter than this, corresponding to the faintest possible HII region. The 8 and 24 μm luminosities within the central 5 kpc of M 33 are comparable and of order 4×10^{28} erg s^{-1} Hz^{-1} ($\nu L_\nu(8) = 1.5 \times 10^{42}$ and $\nu L_\nu(24) = 4.4 \times 10^{41}$ erg s^{-1}). We estimate the total IR emission in the same region of M 33 to be 10^9 $L_\odot$. The discrete sources account for about one third of the 24 μm emission while the rest is diffuse. From the IR emission, we derive a star formation rate for the inner disk equal to 0.2 $M_\odot$ yr^{-1}, consistent with the star formation rate obtained from the Hα emission.

Key words. galaxies: individual: M 33 – galaxies: ISM – galaxies: Local Group – galaxies: spiral

1. Introduction

The interstellar medium (ISM) in galaxies provides the raw material from which stars form, and is the repository of the products of stellar evolution. Stars form in condensations of cool molecular gas, eventually destroying their birth sites through energetic photons, massive stellar winds, and supernova (SN) explosions. Dust is formed through coagulation in stellar winds and supernova ejecta, and over time, becomes an integral part of the ISM. Radiative and mechanical energy are input to the ISM through massive star formation and evolution, in the form of ionising photons, supernova explosions, and magnetic fields. The ISM properties, such as magnetic field, gas, and dust, affect star formation processes on all scales. At the same time, star formation drives the evolution of the ISM. On the long term, local processes of star formation can influence large-scale structure in the ISM and determine how galaxies evolve. Ultraviolet and optical wavelengths are not the best wavelengths for SF studies, because dust can hide massive star formation, mask the effects of feedback, and redistribute the ISM energy and radiation. However, first *IRAS* (Neugebauer et al. 1984), then *ISO* (Kessler et al. 1996), and now *Spitzer* (Werner et al. 2004) have been able to penetrate the dust in the ISM, and thus better study the interaction among its constituents.

In this series of papers, we examine star formation properties of the Local Group late type spiral M 33. The proximity of Local Group members together with *Spitzer* resolution makes possible the resolution of structures on spatial scales of 5–10 pc, and enable us to effectively study individual star forming sites and their surrounding environment in a galaxy different from our own. M 33, is at a distance of 840 kpc (Freedman et al. 1991), its mass and apparent size are smaller than that of M 31 but M 33 hosts the brightest HII complex in the Local Group. This, together with its blue colour assures us that star formation is still very active throughout its disk. M 33 bears no signs of recent mergers and therefore gives us a unique opportunity for investigating the interplay of gas, dust, and star formation in isolated galaxy disks. This is possible thanks also to high resolution and sensitive observations now becoming available for this nearby galaxy at all wavelengths. Chemical abundances have been measured in stellar populations of different ages (e.g. Magrini et al. 2007a,b), and surveys of atomic and molecular hydrogen point out the location of massive gas clumps (Engargiola et al. 2003; Heyer et al. 2004). Through detailed dynamical mass modeling of the galaxy we can now trace the mass distribution of visible and dark matter (Corbelli & Salucci 2000; Corbelli 2003).

⋆ Tables 2 and 3 are only available in electronic form at http://www.aanda.org

Our focus here is first on M 33's population of discrete known type of point sources: HII regions, supernova remnants (SNRs), and planetary nebulae (PNe). In principle, these sources track different phases of the star formation process, from the generation of ionising photons and stellar winds in massive stars, to subsequent explosion as SNe and finally to the more evolved stage of PNe. Hence, our immediate goal is to assess the physical conditions of the stellar environment at different stages. The second purpose of this paper is the generation of an IR source catalogue from the *Spitzer* MIPS observations at 24 μm. Here we shall use IRAC-MIPS diagnostic diagrams of known sources to better understand the nature of these sources. In a subsequent paper we will relate the IR properties with detailed observations of the surrounding ISM at other wavelengths and to the disk large-scale structure. *Spitzer* data and the vast multi-wavelength dataset available for M 33 will help understand how star formation proceeds in low luminosity spiral galaxies and how this relates to other global galaxy properties.

The present paper is structured as follows: in Sect. 2, we present the *Spitzer* IRAC and MIPS data and their reduction process. The large scale structure of the dust emission in M 33 is investigated through colour images in Sect. 3. We analyse the IRAC and MIPS 24 photometry of discrete type-known sources (HII regions, PNe, SNRs) in Sect. 4 and compare their colours to theoretical diagnostic diagrams in Sect. 5. In Sect. 6, we present a catalogue of the sources emitting in the 24 μm MIPS band and interpret their nature in light of the results obtained in the previous Section. The reliability of the IR emission as a star formation tracer, through comparison with Hα, is investigated in Sect. 7. Finally, the summary and conclusions of our study are given in Sect. 8.

2. Observations and data reduction

We retrieved images from the Guaranteed Time Observations (PID 5, PI R. Gehrz) in the *Spitzer* Space Telescope (Werner et al. 2004) data archive. The *Spitzer* Space Telescope carries two photometric cameras: the Infrared Array Camera (IRAC) and the Multiband Imaging Photometer (MIPS).

2.1. IRAC data

The Infrared Array Camera (Fazio et al. 2004) is equipped with two detector arrays of 256 × 256 pixels. The field of view of a single array is 5.′2 × 5.′2. We analyze here eight sets of IRAC observations of M 33 (AORs 3636224, 3636480, 3637760, 3638016, 3638784, 3639040, 3640320, 3640576) in all four IRAC bands. The Basic Calibrated Data (BCD) were created by the *Spitzer* Science Center (SSC) pipeline, version S14.0.0 for all AORs. As the first data frame of each observation sequence has a shorter integration time than the regular exposure time (10.4 s), we discarded those frames. A more complete description of the observations is given by Hinz et al. (2004), McQuinn et al. (2007), and Tabatabaei et al. (2007a).

The mosaics were assembled gathering all the BCDs for each wavelength. The individual calibrated frames were processed using Mopex (Makovoz & Khan 2005), with a cosmic-ray rejection and a background matching applied between overlapping fields of view. During the reduction, we used a common value of the pixel size equal to 1.″20. The final number of individual BCDs used is about 1700, in each IRAC channel. The final dimension of the mosaics is approximately 62.′4 × 91.′7. Because of the overlap between adjacent BCDs, the mean redundancy is 12 (from 6 to 30).

The obtained IRAC mosaics were background subtracted, estimating 20 sky levels (the median values in 5 × 5 pixels boxes) near the edges of the mosaics, the farthest from the galaxy centre. The 5.8 and 8.0 μm channels presented a gradient in the background, and we removed it using a fitted surface with the IRAF task imsurfit (images.imfit). In each channel, the final background value subtracted is the mean of the 20 median values: 0.059 at 3.6 μm, 0.146 at 4.5 μm, 1.475 at 5.8 μm, and 5.389 at 8.0 μm. The mosaics were then aligned using the IRAF tasks geomap and geotran (in immatch) using 15 point sources.

Because of the diffraction limit of the telescope, the images have a resolution of 1.″7 to 2.″0 (see IRAC Observing Manual) which translate into 6.7 to 8 pc at the distance of M 33. The final IRAC mosaics at 3.6, 4.5, 5.8, and 8.0 μm are shown in Fig. 1.

2.2. MIPS data

Images of M 33 at wavelengths 24, 70, and 160 μm (with bandwidths of 5, 19, and 35 μm, respectively) were obtained using data collected by the Multiband Imaging Photometer (Rieke et al. 2004). MIPS uses true detector arrays: 128 × 128 pixels at 24 μm (Si:As detector), 32 × 32 pixels at 70 μm (Ge:Ga device) and 2 × 20 pixels at 160 μm (Ge:Ga device). The nominal fields of view are 5′ × 5′ at 24 and 70 μm and 0.′75 × 5′ at 160 μm. The resolution of the instrument is diffraction limited to 6″, 18″, and 40″ at 24, 70, and 160 μm, respectively. The operating modes of all the observations were "scan map", the telescope scanning the sky at a constant rate.

As for IRAC, we retrieved eight MIPS datasets from the archive (AORs 3647744, 3648000, 3648256, 3648512, 3648768, 3649024, 3649280 and 3649536). The 24 μm BCDs were created by the SSC pipeline version S16.1.0. The exposure times of the DCEs were 3.67 s (except for the first frames of each series, where the integration time per pixel is lower and which consequently were not used in the further reduction steps). Since the observations were acquired over two epochs, the respective mosaics were assembled separately using Mopex. For consistence with the IRAC reduction, the pixel size was chosen to be 1.″20. The first epoch includes 4199 frames, and the second one includes 4500 frames. This latter map is displayed in Fig. 2. The mean redundancy per sky position is 22 (varying from 10 to 40), in each mosaic. This high level of redundancy removes any spurious effects such as cosmic-ray hits and provides more reliable measurements. In the present article, as we plan to focus on point sources (HII regions, SNRs and PNe) located near the centre of the galaxy, we chose to concentrate, for each epoch, on the two central AORs. These two images were then aligned with the reference of the coordinates of 8 point sources and combined together by keeping the average of the pixel values. A small background gradient was still visible in the combined image and was removed by fitting a surface to selected regions (IRAF task: imsurfit). The zone defined by the superposition of the two central AORs of each epoch is marked on the 24 μm image (see Fig. 2). The resolution measured on the final image is 6″.

The 70 and 160 μm MIPS observations were acquired with the same AORs as the 24 μm observations. The version S16.1.0 of the SSC pipeline was also used to create the BCDs. The integration times of the DCEs is 4.19 s, both for the 70 and 160 μm observations. We used Mopex to create the final mosaics (again the pixel sizes were chosen to be 1.″2), including 8750 individual frames at each of the two wavelength channels. The mean redundancy is about 20 (from 8 to 42) and 6 (from 2 to 10) at 70 and 160 μm, respectively. The final images show some striping along the scan direction that is a residual instrumental artifacts due to

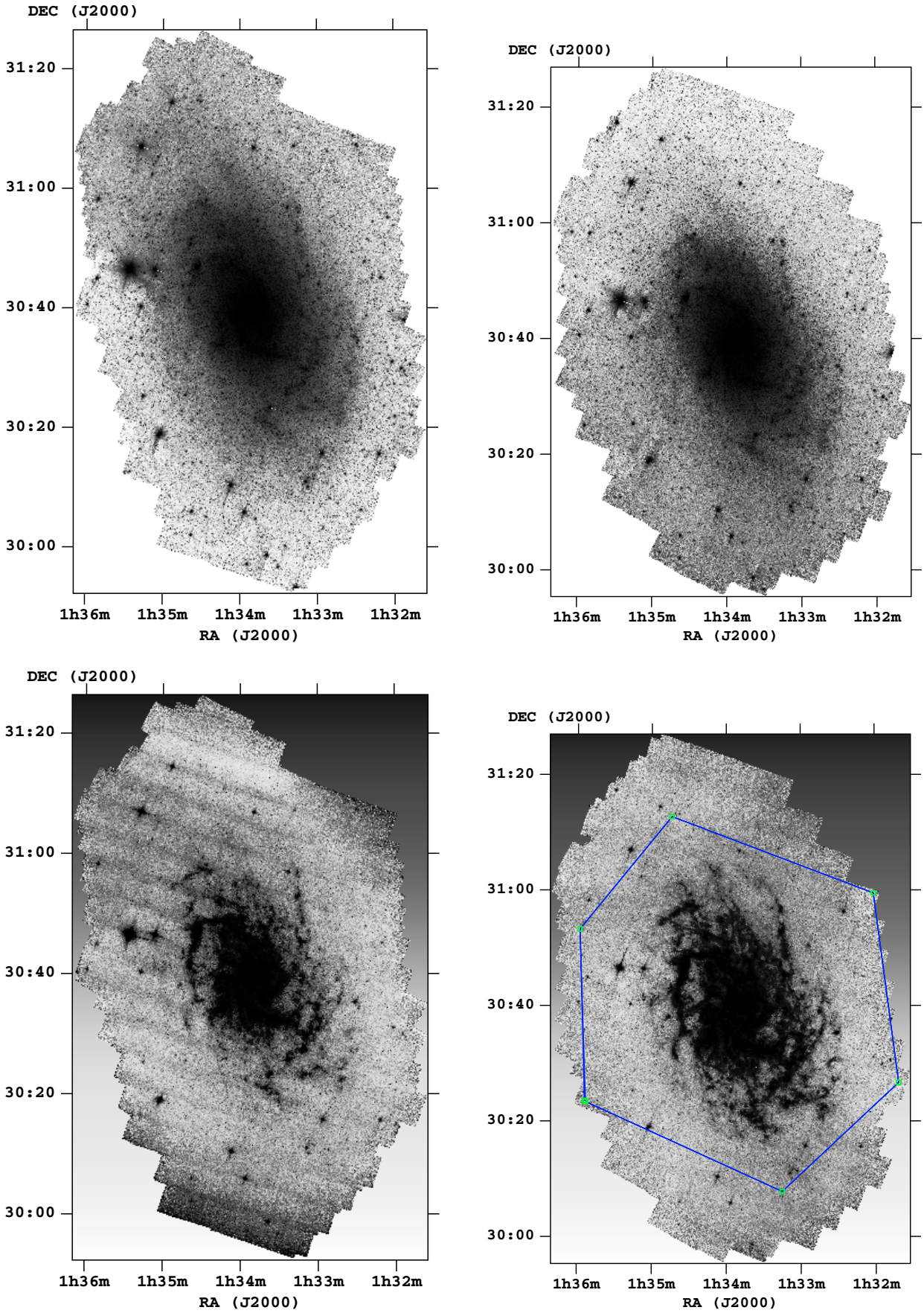

Fig. 1. Final IRAC mosaics of M 33. The upper left image displays the 3.6 μm, the upper right 4.5 μm, the lower left 5.8 μm and the lower right the 8.0 μm channel. The images are about 1° by 1.5°, north is up and east is to the left. The region enclosed by the continuous line will be further investigated in the present paper.

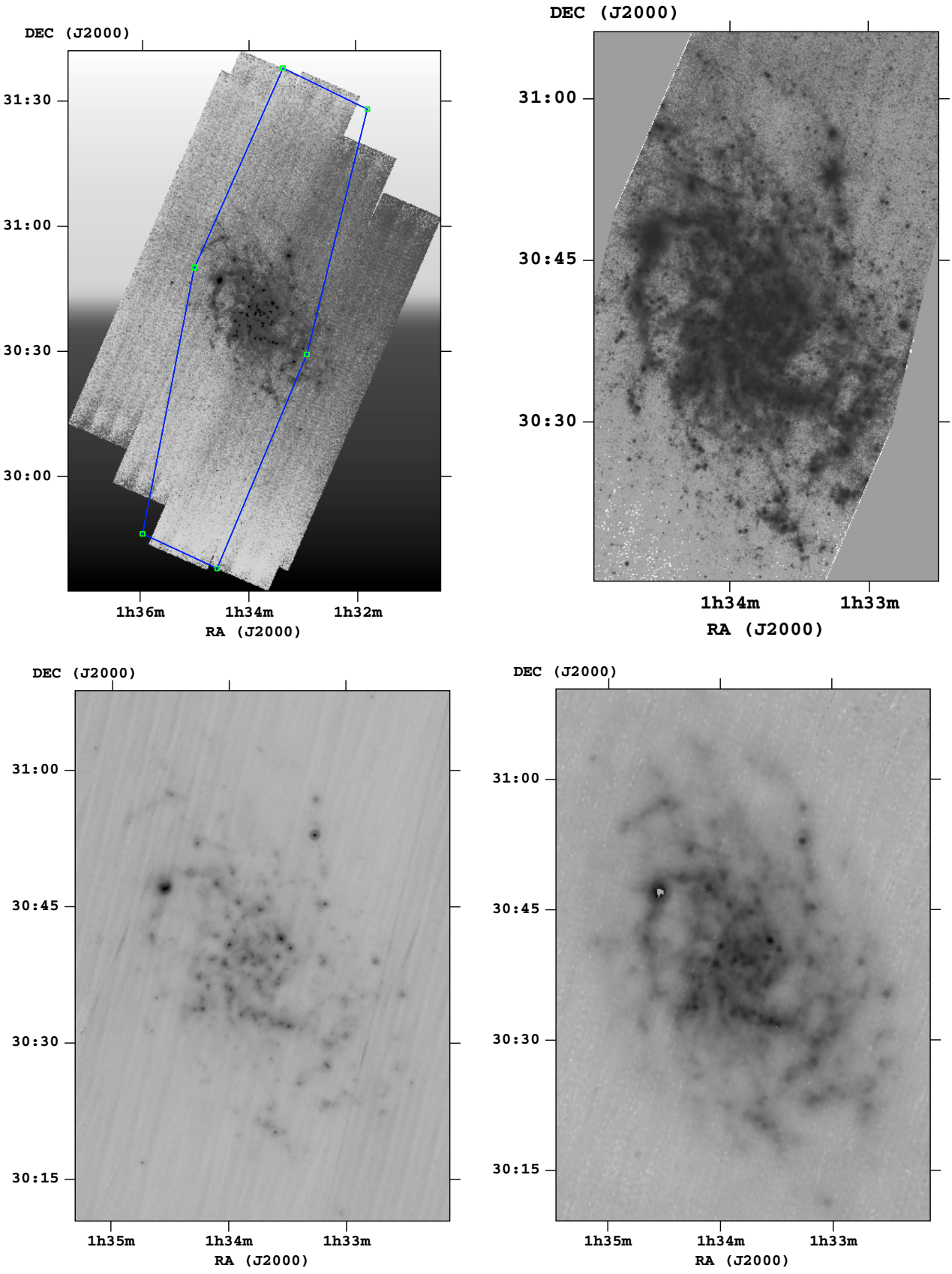

Fig. 2. MIPS images of M 33. The upper panels display the 24 μm images: the full image (one single epoch) is on the left. The inner region enclosed by the continuous line will be further investigated in the present paper, and is shown in the upper right panel after overlapping the data from two different epochs. The bottom left panel shows the 70 μm channel, and the lower right the 160 μm channel. The images are about 30′ × 50′, north is up and east is left.

the time-dependent responsivity of the Ge:Ga detectors (Helou et al. 2004; Hinz et al. 2004). The final resolution is about 16″ and 40″ for the 70 and 160 μm images, respectively. The final MIPS images (24, 70, and 160 μm) are shown in Fig. 2.

2.3. Hα image

We also include in our analysis an optical narrow-band Hα image, a standard star formation indicator. The M 33 Hα emission was observed at the Kitt Peak National Observatory (NOAO). The dimensions of the CCD are 2048 × 2048 with pixels of 2.″03 and a total field of view of about 70′ × 70′. More details of the observations and reduction process can be found in Hoopes & Walterbos (2000); the estimated [N II] contamination accounts for at most 5% of the measured flux. The total Hα luminosity of M 33 is about 7×10^6 $L_\odot$ and is dominated by HII regions (Devereux et al. 1997). The optical extinction in M 33 is found to be globally low, $A_V < 0.4$ mag. Towards HII regions $A_V \sim 1$ mag on average even though it can reach values as high as 2 mag towards high surface brightness cores (e.g. Israel & Kennicutt 1980; Devereux et al. 1997). The moderate values of extinction imply that Hα can be used as an SF tracer globally, but towards individual sources an extinction correction can become necessary.

3. Large scale structure of stars and dust

In the present paper, we concentrate on the inner region of M 33 as defined by the *Spitzer* inner AORs which is outlined by the continuous line in Figs. 1 and 2 for the IRAC and MIPS data, respectively.

In order to help the interpretation of *Spitzer* data, we first review briefly which are the main emission phenomena that dominate each IRAC and MIPS waveband.

3.1. Origin of the emission detected by Spitzer

The stars (mainly Red Giant Branch and/or Asymptotic Giant Branch, according to the age of the population) account for most of the emission in the 3.6 μm IRAC band. A mix of stars and very hot dust continuum contribute to the emission in the 4.5 μm band. Nevertheless, in discrete sources with negligible continuum (see Sect. 4), the emission seen in both these bands can have a strong component of ionic and molecular lines (e.g., Reach et al. 2006; Williams et al. 2006). In the 5.8 μm IRAC band, the stellar contribution decreases and the dust continuum component gets stronger. The longest-wavelength 8.0 μm IRAC band still traces hot dust continuum but in most cases, the polycyclic aromatic hydrocarbons (PAH) dominates. If there are no PAHs and low continuum, however, in discrete sources there can be a sizable contribution from two H_2 lines and the [Ar III] at 8.9 μm (e.g., Hora et al. 2004).

The PAH emission features (mainly concentrated at 3.3, 6.2, 7.7, 8.6, and 11.3 μm) are the optically active vibrational modes of PAH molecules (Leger & Puget 1984; Allamandola et al. 1989), resulting from internal conversions of energy following absorption of an optical or UV photon. The IRAC bands 3.6, 5.8, and 8.0 μm contain PAH emission features at 3.3, 6.2, and 7.7 & 8.6 μm, respectively (Draine 2003; Churchwell et al. 2004). The 4.5 μm channel is the only one with no PAH features, although it contains the bright hydrogen recombination line Brα (4.05 μm).

We investigate the far-infrared (FIR) emission with the MIPS images. The 24 μm emission is contributed partly by thermal emission of classic (large) dust grains and partly by very small grains (VSGs). Indeed, VSGs were introduced by Desert et al. (1990) as the carrier of the emission in the 25 μm IRAS band. The 70 μm emission traces cooler dust, and the 160 μm one shows the diffuse cold dust component.

3.2. Structure of infrared emission in M 33

Figure 1 shows that the stellar component is smoothly distributed everywhere in the disk of M 33. The warm and hot dust traced by the 5.8 μm channel smoothly follow the morphological patterns (spiral arms and flocculent structures) of M 33 with a higher concentration in the inner part of the galaxy. Compared with the other components, the 8.0 μm contribution shows most clumpy distribution; evidently PAHs are preferentially located along the spiral arms and flocculent structures, rather than being uniformly distributed in the ISM. The very centre of the galaxy gathers all the three contributions: stars, dust and PAHs.

3.3. The colour images

To help investigate the large scale structure of M 33 as seen by *Spitzer* we made two sets of colour images: one degraded to the worst resolution of the IRAC channels, and a second set degraded to the resolution of the MIPS 24 μm image. We approximated the PRF with a Gaussian and convolved both sets to the resolution of the worst image in the set (8 μm and 24 μm, respectively).

Figure 3 shows the 3.6/4.5 ratio (left panel) and 4.5/8.0 ratio (right) of M 33. The 3.6/4.5 shows a remarkably constant ratio (∼1.7) over almost the entire galaxy, confirming the statement by Pahre et al. (2004), who find that for each galaxy, the [3.6]−[4.5] colour is nearly constant with radius and consistent with stellar photospheric emission. The 5.8/8.0 ratio (not shown in Fig. 3) is also approximately constant (∼0.5), similarly to other galaxies such as NGC 300 by Helou et al. (2004), even though it might not be a general feature. In both the 5.8 and 8.0 μm bands there is an increase of the diffuse emission relative to the 3.6 and 4.5 μm bands, as in our Galactic plane. The 8.0/24 colour (not shown) also does not show any evident radial gradient or prominent structure and is practically constant across the disk. Similarly to the 5.8/8.0 ratio, this result points out the overall constancy in the ratio of PAHs and warm dust emission in this galaxy.

On the other hand, the 4.5/8.0 images (right panel of Fig. 3) and the 3.6/5.8 ratio (not shown) both retain the structural pattern of M 33, tracing the inner features, the two main spiral arms and the filamentary structure of the disk. In the first case, this is probably due to the predominant PAH features in the spiral arms and filaments; in the second, the ISM as reflected in the 5.8 μm band is emerging relative to the stars at 3.6 μm. The 8.0 μm emission along the spiral arms and along filaments surrounding the dimmer star forming regions at large galactocentric distances become prominent.

We also constructed an IRAC three colour image of M 33 by subtracting the stellar component in the shorter-wavelength images from the 5.8 and 8.0 μm ones. To remove the stellar contribution from the 5.8 and 8.0 μm images, we used the recipe by Helou et al. (2004); Pahre et al. (2004); Calzetti et al. (2005); Perez-Gonzalez et al. (2006). The 3.6 and 4.5 μm images were combined assuming colours appropriate for an M0 III star ([3.6]−[4.5] = −0.15 in Vega mag). The final combination is shown in Fig. 4 and displays the stars in blue, the star-subtracted

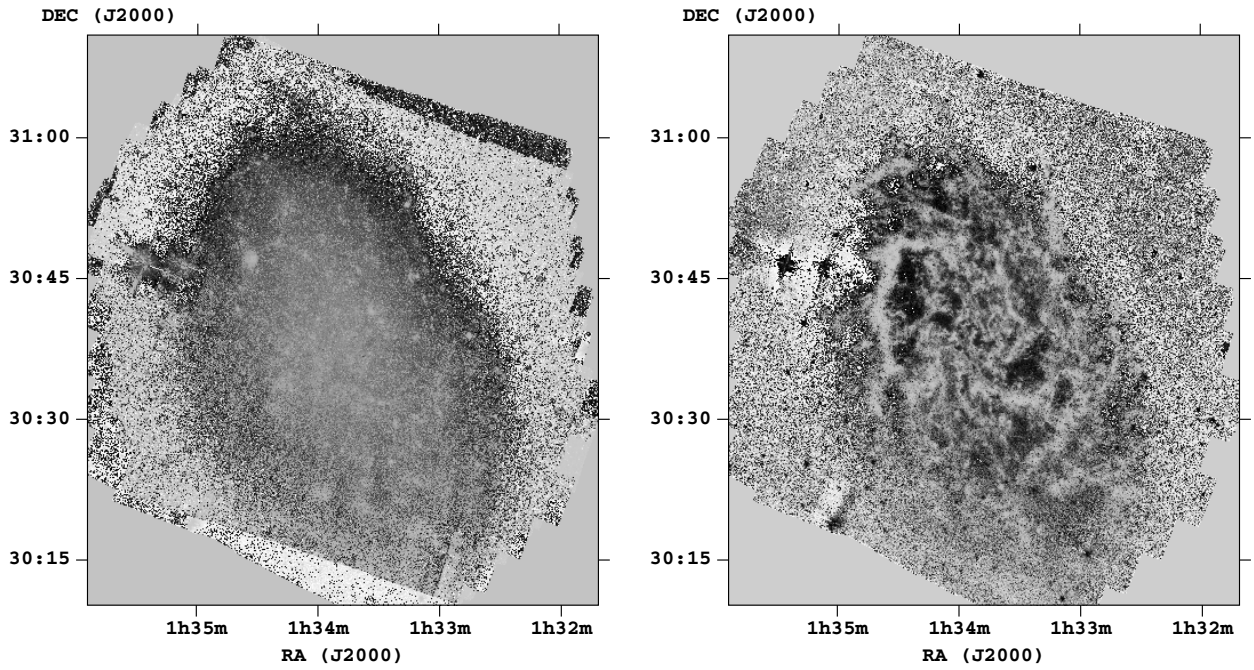

Fig. 3. Colour images representing the ratio of the 3.6 over 4.5 μm images (*left*) and 4.5 over 8.0 μm (*right*). These images have a common resolution roughly equivalent to that in the 8.0 μm image. White corresponds to low colour ratios, and black to high ones.

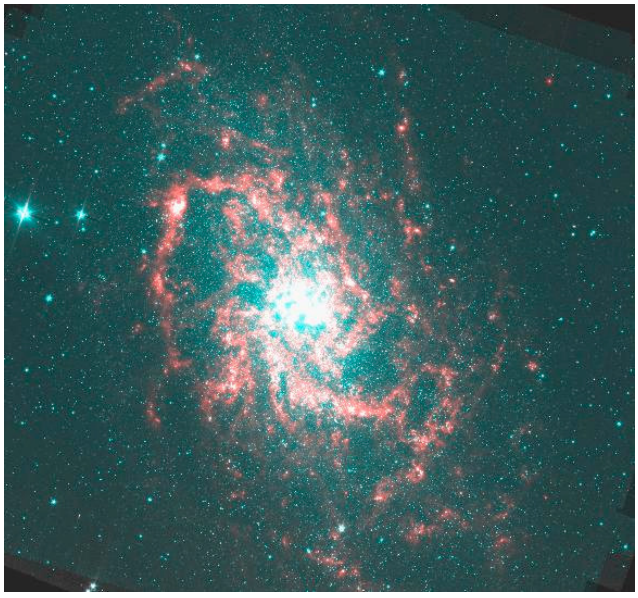

Fig. 4. M 33 three colour image, composite of the central region of the complete IRAC data. Blue is a weighted mean of 3.6 and 4.5 μm, representing the evolved stellar population. Green depicts the 5.8 μm light after removal of stellar emission, and red traces the 8.0 μm channel also corrected for stellar emission. (See the electronic edition of the Journal for a colour version of this figure.)

5.8 μm in green and the star-subtracted 8.0 μm in red. The dominance of the 8 μm emission in the spiral arms is clearly revealed by Fig. 4. The underlying stellar disk is also evident; the excess of stellar light in the centre has been pointed out by previous near-infrared ground observations (Regan & Vogel 1994), and is related to the possible presence of a bulge or bar component.

3.4. Distribution of cool dust

Over the last fifteen years, many studies have been devoted to the FIR emission of M 33 using IRAS and ISO. Rice et al. (1990) observed M 33 with IRAS at 12, 25, 60, 100 μm and found a striking correlation between the spatial IR structure and the HII regions. They estimated that 75% of the integrated IR emission arises from stars younger than a few times 10^8 yr. The close correspondence between the Hα image and the FIR (60 and 100 μm) morphology was also noted by Devereux et al. (1997). Hippelein et al. (2003) studied M 33 with ISOPHOT at 60, 100 and 170 μm, and concluded that the FIR emission is composed of a superposition of two components: i) a warm one, found in spiral arms and SF regions, heated by UV radiation from OB stars, contributed by dust at about 45 K; and ii) a cold one around 16 K which is smoothly distributed over the disk and heated by diffuse interstellar radiation.

More recently, Hinz et al. (2004) used MIPS observations of M 33 to investigate the origin of the FIR emission, and found that the emission in the 24 and 70 μm MIPS images follows closely the structure of the ionised gas, suggesting heating by hot, ionising stars. The overlays of Fig. 6 (see Sect. 3.5) show the link between 24 and Hα, i.e. between the hot dust emission and the formation sites of massive stars (see also Tabatabaei et al. 2007a). This link is also evident by comparing the Hα and 70 μm emission maps. Moreover, comparing thermal and non-thermal radio images of M 33 with MIPS suggests that the 24 and 70 μm emission is more closely associated with the thermal radio component than with the non-thermal one (Tabatabaei et al. 2007a). Both the 24 and the 70 μm emission originates in fact from warm dust associated with massive star formation. We discuss in more detail the connection between 24 μm discrete sources and Hα knots below.

A more diffuse component emission at 160 μm is evident when comparing it with the 24 μm map. Cold dust heated by a diffuse interstellar radiation field clearly contributes to the longer wavelength MIPS band.

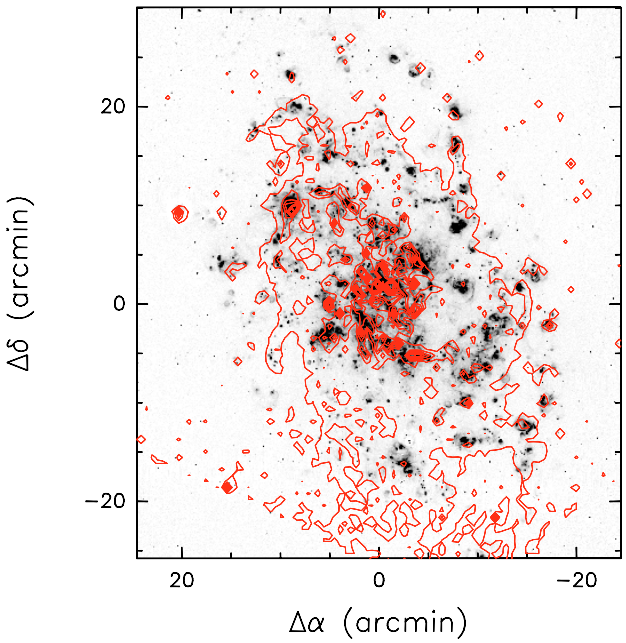

Fig. 5. Hα image of M 33 with the over-plot of 8.0 μm contours.

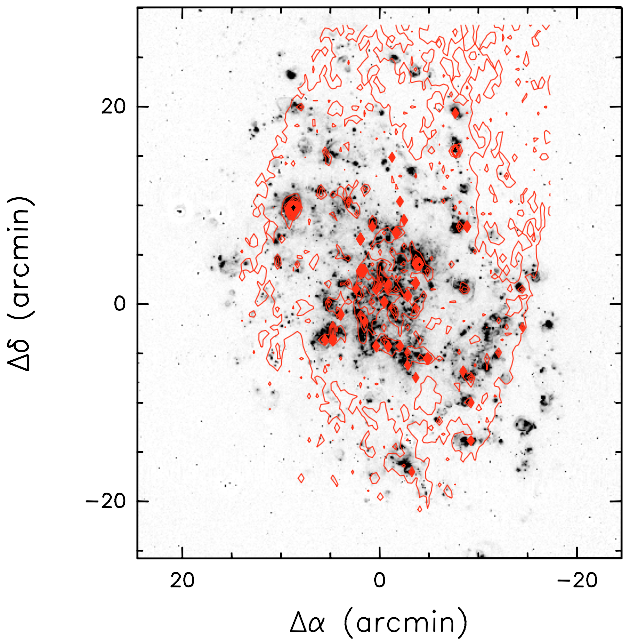

Fig. 6. Hα image of M 33 with the over-plot of 24 μm contours.

3.5. Comparison with Hα

In Figs. 5 and 6, we show the 8.0 and 24 μm contours on the Hα image. Other than the two brightest HII regions (NGC 604 and IC 133), the highest levels of 24 μm emission are concentrated in the inner part of the galaxy, and the 24 μm emission mainly follows the spiral arms. Notably, not all the Hα bright spots have bright 24 μm counterparts. Moreover, the centre of the 24 μm emitting sites can be shifted with respect to the centre of the Hα emission sites. This might indicate that some of the optical emission from the HII regions is obscured by dust or may be due to different intrinsic structures related to the evolution of HII regions. Of particular interest are the 24 μm emission spots not associated with Hα emission, which could trace deeply embedded HII regions, or a different population of objects. In Fig. 5, we can see the same general trends with a concentration of the 8 μm emission in the centre and along the spiral arms of the galaxy. At larger radii, the 8 μm emission becomes more diffuse respect to the 24 μm component which matches better the bright Hα knots. At 8 μm, the southern arm shows a much more concentrated emission than the northern arm. A similar trend has also been found for the molecular gas: giant molecular clouds and diffuse molecular gas emission follow the pattern of the arm in the south as traced by Hα much more closely than in the north (Engargiola et al. 2003; Heyer et al. 2004).

4. The IR emission of nebulae in M 33

We used six catalogues of three classes of known-type sources in M 33: three catalogues of HII regions selected at different wavelengths, two catalogues of SNRs, and one catalogue of PNe:

1. IR HII regions: 28 sources, Giveon et al. (2002), Willner & Nelson-Patel (2002);
2. Radio HII regions: 40 sources, Gordon et al. (1999);
3. Optical HII regions: 78 sources, Magrini et al. (2007b);
4. Optically selected SNRs: 98 sources, Gordon et al. (1998);
5. Radio selected SNRs: 30 sources, Duric et al. (1995), Gordon et al. (1999);
6. PNe: 152 sources Ciardullo et al. (2004).

The properties of these will be compared to our catalogue of 24 μm-selected sources in Sect. 6.

We have selected our sample of HII regions from three different catalogues, which include HII regions of different morphologies, locations within the galaxy, and brightness. Our IR sample was obtained by merging the sources observed by Willner & Nelson-Patel (2002) and Giveon et al. (2002). It includes in total 28 sources located in three chains, to the east, west, and south of the galaxy nucleus. Our radio sample comprises 40 HII regions with 20−6 cm spectral index (ν^{α}) $\alpha > -0.2$ as catalogued by Gordon et al. (1999), and extends out to 20′ galactocentric radii. A list of 78 optically selected HII regions, from narrow band images and with known optical spectra, was kindly provided to us by L. Magrini (Magrini et al. 2007b). Such regions are in general much fainter than the IR or radio selected regions and are located preferentially at large galactocentric radii.

To probe dust emission during the final stages of stellar evolution, we selected two samples of SNRs, one defined optically and one defined in the radio. The optical sample (Gordon et al. 1998) contains 98 SNR candidates selected primarily on the basis of optical emission-line ratios. The radio sample of SNRs contains 30 (radio-bright) sources appearing both in Duric et al. (1995) and Gordon et al. (1999). Their selection criteria are effective at finding middle-aged remnants. In fact, since their SNRs have diameters in the range 20−48 pc, most of the SNRs should be in the Sedov-Taylor expansion stage. The contamination in their sample is estimated to be less than 1, but there are 20 SNRs embedded within HII regions. Still, several remnants are associated with nearby HII regions and some are embedded in them.

Finally, we adopt the catalogued PNe of Ciardullo et al. (2004). As a result of a photometric and spectroscopic survey, they identified 152 PNe candidates in M 33. By comparison with Magrini et al. (2001), the contamination by HII regions or SNRs is estimated at ∼22%.

4.1. Photometric methodology

We have six source lists of known type, for a total of more than 400 objects distributed over the entire disk of M 33. Our aim is to use the IRAC/MIPS-24 colours of these as empirical diagnostics to infer the dust properties in various kinds of nebulae. This is done by comparing their IR colours with the theoretical colour diagrams (see Sect. 5).

To these source lists we then add the 24-μm selected sample and we shall infer the nature of these sources by comparing their IR colours with those of known-type of sources (see Sect. 6). We are also interested in the Hα emission of our objects, in particular for the 24-μm selected sample and therefore we need to perform photometry on the Hα image. Therefore, we must perform photometry in a total of six bands (4 IRAC, MIPS-24, and Hα). We merge the IR photometry, and consider only those sources which have measurable emission in all the IR bands examined, in order to place them on our diagnostic colour diagrams.

The proximity of M 33 combined with the superb resolution of *Spitzer* makes photometry of individual sources in the galaxy challenging. Isolating sources is difficult, because of the extremely crowded fields, especially the inner disk and circumnuclear regions. Moreover, we expect that many of the objects (e.g., HII regions and SNRs) will be extended, so that we cannot accurately perform point-source fitting and subtraction with point-response functions. In addition, many classes of sources are not prodigious emitters in the mid-infrared (MIR), which further complicates the automatization of the photometric procedures. Hence, we investigated many photometric schemes before finally arriving at a reliable solution.

Following Calzetti et al. (2005), we first attempted aperture photometry of the sources in our lists. The initial centres were taken from the source lists described in Sect. 4, and the centre of the virtual aperture was then allowed to vary up to a certain distance from the initial position. While this is a viable solution in other situations, it turned out not to be feasible in M 33. First, the definition of the fiducial aperture should depend on source extent, but this differs among the source classes, so it was not clear how to define the limiting aperture. This was an especially vexing problem for the wavelengths in which a given source does not have measurable emission, since the automatic centring routines did not converge. Second, the determination of the background was extremely problematic because of the variable degree of crowding and the variable degree of diffuse emission. It was also unclear how to define either "regional" or "global" backgrounds in the case of M 33. Thus, we were forced to find another solution.

We then attempted elliptical cross-section Gaussian fitting of sources (e.g., Calzetti et al. 1995). The fitting box was fixed to a series of dimensions (from 25 to 10 pixels), and the centre, the orientation, the width, and a constant background level were left free to vary. As before, the initial centres were taken from the source lists. The larger fitting boxes allowed the centre to wander too much from the initial position. Hence, the source identified by the fitting routine frequently did not correspond to the source in the list, although reasonably accurate backgrounds were obtained when checked against the source surroundings. The smaller fitting boxes better constrained the centre, but in crowded fields gave a background which was much too high. This resulted in gross underestimations of the total flux, especially when the source was rather faint and comparable to the estimated background. An additional problem encountered with Gaussian fitting was its unsuitability for multiple sources. Many of the sources in our lists are in truth "clusters" of smaller sources when examined with the *Spitzer* spatial resolution and at wavelengths different from those in which the sources were defined. These problems taken together led us to distrust this method for a large fraction of sources in our lists.

To overcome these shortcomings, we finally devised a "hybrid" solution, which optimally combines the photometry from Gaussian fitting and that from isophotal photometry. This last was accomplished with SExtractor (Bertin & Arnouts 1996) which is able to deal with very large images automatically, and handles reasonably accurately a wide variety of object shapes and sizes. The idea was to calculate the total flux integrated over an irregularly shaped aperture containing flux levels above some isophotal limit. The hybrid method consists of three steps: (1) perform Gaussian fitting of all sources as described in the previous paragraph; (2) perform SExtractor photometry as described below; (3) merge the two sets of photometry according to an algorithm which decides which photometric measurement to prefer, in order to have one measurement per source.

For (1), we adopted a fitting box of 10 pixels; this was the best compromise between centre wandering and background level, as the photometry was typically centred on a position relatively close to the initial one, although with a potentially spuriously low flux because of the background determination.

In practice, for (2), we used the ASSOCIATIVE feature of SExtractor, and input our source lists with initial positions. The initial SExtractor photometry consisted in those sources extracted at a 10σ level above the background, at a distance within 15 pixels ($\equiv\Delta r$) from the initial position. These two values resulted to be the best compromise between source association and source identification. Lower values of signal-to-noise ratio ($<10\sigma$) resulted in more sources being identified, but were in the mean farther away. The background for the SExtractor photometry was defined to be the local median of the image in a 64-pixel box centred on the source.

Step (3), the merging of the Gaussian fitting and SExtractor photometry, was accomplished by examining the radial distance of each measurement from the initial position. When the SExtractor centre was within Δr of 5 pixels (in radius), and as long as it was within a factor of two of the Gaussian fitting centre, it was preferred over the Gaussian method. We experimented with a few values of Δr and a few values of the relative ratio of the radial distances, and concluded that this gave the best results overall. Indeed, it appears that this hybrid approach overcomes the problems of underestimating source fluxes because of background estimates, and successfully calculates the total flux even when sources are in fact multiple. Indeed, the SExtractor photometry and the Gaussian fitting results are fairly well correlated except for low fluxes with high background where Gaussian fitting tends to underestimate the true flux, and high fluxes for extended or clustered sources.

4.2. Detection rates

The detection statistics are illustrated in Fig. 7 and Table 1. The matching radius $\Delta r_{\rm max}$ for the coincidence of sources, was determined by examining the scatter on the diagnostic diagrams, see Sect. 5. In the end we adopted a value $\Delta r_{\rm max} = 3$ pixels (about 14 pc), which is sufficiently large to accommodate possible astrometric uncertainties.

The positions of catalogued sources with photometry in all four IRAC bands are shown in Fig. 8, on the IRAC 4.5 μm image of M 33. The upper panel refers to HII regions and we note that the optically selected sample is mainly in the outer regions of the galaxy, while the IR and radio selected HII regions are in

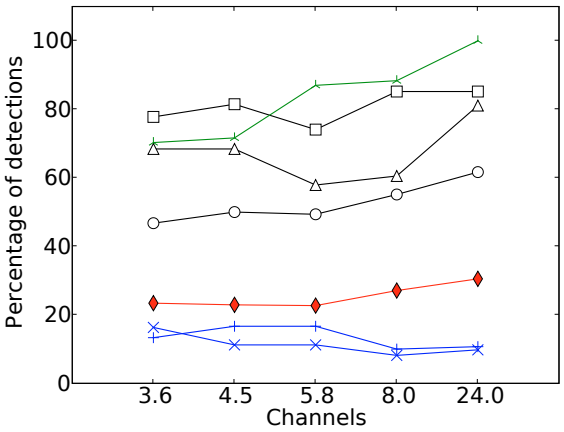

Fig. 7. Detection rate in the different wavebands. Open symbols represent the HII regions selected in IR (squares), radio (triangles) and optical (circles). The (blue) crosses represent the optically selected SNRs and the (blue) plus signs the radio selected SNRs. The filled (red) diamonds represent the PNe. The (green) tripods represent our 24 μm sources.

Table 1. Detection rate in all four IRAC and IRAC+MIPS-24 bands.

	IRAC	Total	%	IRAC+MIPS-24	Total	%
ISO	17	27	61%	15	27	54%
Hra	18	38	45%	18	37	45%
HII	27	77	35%	19	60	32%
SNo	3	98	3%	2	92	2%
SNR	1	30	3%	1	28	3%
PNe	9	141	6%	4	118	3%
24Ss	306	515	59%	306	515	59%

the inner parts of M 33. The lower panel shows the locations of PNe and SNRs. The single detection of the radio-selected SNR coincides with an optically-selected one.

4.2.1. HII regions

The detection rate of HII regions depends on the waveband and on the catalogue. As expected, the brighter HII regions (radio and IR sample) are detected at a higher rate than the faint ones (optically selected catalogue). The detection rate for bright regions increases even more if we loosen the strict requirement about the centre displacement. For large HII regions in fact the centre of the IR emission can be displaced by more than 3 pixels from the nominal position, and hence not accepted as coincident. The lower resolution in the 24 μm band makes objects rounder, and the Gaussian fitting is often more accurate than in the 5.8 and 8.0 μm band. This partly accounts for the higher detection rate in the 24 μm MIPS wavelength. But, there is a general tendency for the HII regions to be less visible in the shortest wavelengths (3.6 and 4.5 μm) than in the 8.0 and 24.0 μm channels. The detection rate at 5.8 μm always shows a drop, with respect to the adjacent channels (see Fig. 7).

4.2.2. Supernovae remnants

We found a low rate of IR counterparts for the SNRs identified in optical and in radio. The percentage of detections is about 15% for both samples. Four SNRs were detected in at least one band: two were detected at all wavelengths, and other two only at 4.5 μm. The four detected SNRs have radii of ~8−16 pc, while the two undetected ones have radii greater than 20 pc

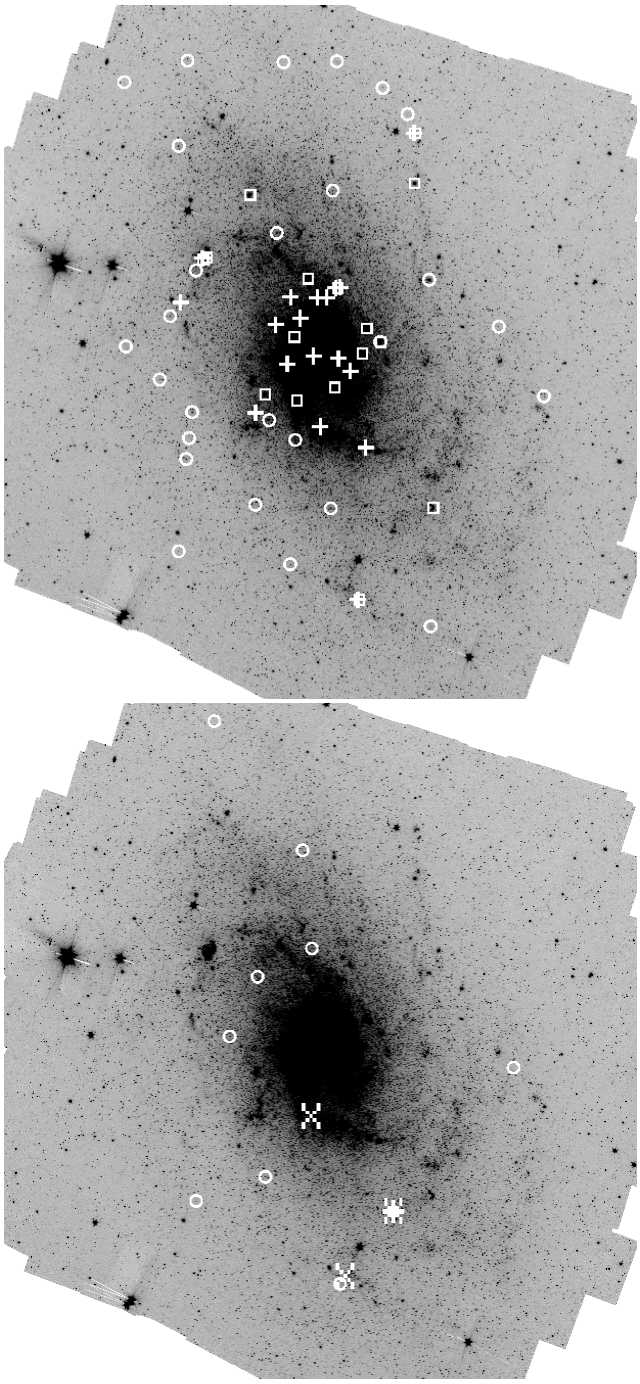

Fig. 8. The position of catalogued sources with photometry in all four IRAC bands superimposed on the 4.5 μm IRAC image. The upper panel shows the IR selected (open squares), radio selected (pluses) and optically selected (open circles) HII regions. The lower panel shows the locations of the PNe (open circles), optically selected (crosses) and radio selected (pluses) SNRs. The images are about 1° on a side, north is up and east to the left.

and may be of a lower surface brightness. The low number of SNR detections is consistent with previous IRAS studies trying to find Galactic SNR counterparts in the IR: 17% (Arendt 1989) and 18% (Saken et al. 1992). Also, using IRAC, Reach et al. (2006) found only 18 IR counterparts out of 95 SNRs in the inner Galaxy. Very few Galactic SNRs were detected by MSX, the Midcourse Space Experiment (Cohen et al. 2006). In the Large Magellanic Cloud, Borkowski et al. (2006) found no emission

from type Ia SNRs and Williams et al. (2006) did not detect the two largest SNRs of their sample in any of the IRAC or MIPS wavebands.

In our samples, the detection rate is also about 30% less in the 8.0 and 24 μm bands with respect to the shorter IRAC wavelengths. This might be due to the destructive effect of the blast wave on the smaller grains; PAHs can already be razed in slow shocks and they are never detected in dense, shocked clumps (Reach et al. 2002). The emission seen at 3.6 and 4.5 μm is likely due to ionic and molecular lines, such as Brα 4.1 μm (Reach et al. 2006; Williams et al. 2006). The environment of the SNRs should have a strong influence on their IR detection rate: remnants interacting with a denser external medium should be more easily detectable. If PAHs in the surrounding ISM are destroyed by nearby supernova events (Gorjian et al. 2004), they will not emit at 8.0 μm (nor contribute to 3.6 and 5.8 μm), which could explain the quite low rate of detection of a remnant in all 4 bands.

4.2.3. Planetary nebulae

The detection rate of PNe is about 25% for the three shorter IRAC wavelengths and then rises steeply to reach more than 50% in the 24 μm band. This is consistent with the result by Cohen & Barlow (2005) who detect PAH emission in less than half of a sample of 43 Galactic PNe. In addition, Hora et al. (2004) claim that the IRAC colours of PNe are red; despite typically negligible continua, they are bright in the 8.0 μm band probably because of a sizable contribution from the two H_2 lines and an [Ar III] line at 8.99 μm.

4.3. Spectral energy distributions

The average IR Spectral Energy Distribution (SED) for our different lists of objects is shown in Fig. 9. HII regions, either IR or radio selected, display the highest fluxes, about two order of magnitudes above the faintest in the list, that is the PNe. The HII optical sample instead, largely consisting of quite faint regions, sits at lower values, in between the two samples of SNRs. The steep rise between 8.0 and 24 μm of all the HII regions samples, implies that HII regions are invariably associated with warm dust. SNRs and PNe show milder slopes, their SEDs being almost flat, or even declining as for optically selected SNRs. This last feature reveals changes of the ISM characteristics related to SN events.

In HII regions, the drop between 3.6 and 4.5 μm can be accounted for by the photospheric contribution of young stars in the two shortest wavelength IRAC channels or perhaps line emission. Candidate lines in the 3.6 μm band include [Fe III] 3.229 μm, and [Co III] 3.492 μm (Gerardy et al. 2007), but line emission can be important in other bands as well as long as there is little continuum emission. This drop has also been detected by Mercer et al. (2004); Gorjian et al. (2004); Jones et al. (2005); Williams et al. (2006); Gerardy et al. (2007). The absence of the 4.5 μm drop in the means of radio selected HII's is due primarily to a single object with a high 4.5 μm flux.

5. Diagnostic diagrams

5.1. Theoretical diagnostic diagrams for IRAC and IRAC/MIPS flux ratios

To better understand the IRAC/MIPS colour diagrams of discrete sources, we assembled a series of models with different physical parameters, as described more in detail below. The IR colours

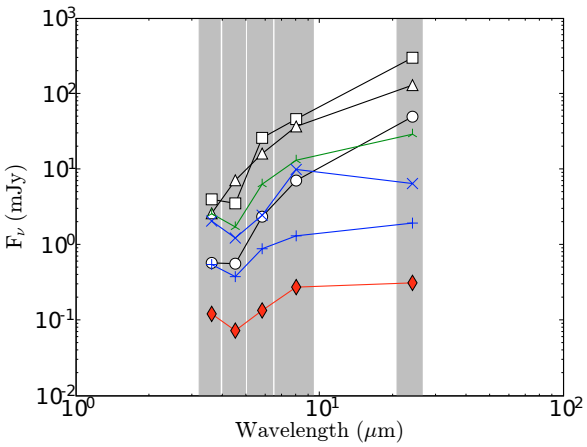

Fig. 9. Mean IR SEDs of the different kind of sources. Open symbols represent the HII regions selected in IR (squares), radio (triangles) and optical (circles). The (blue) crosses represent the SNRs optically selected and the (blue) pluses the SNRs radio selected. The filled (red) diamonds represent the PNe. The (green) tripods represent the 24 μm unknown sources. The grey vertical stripes depict the widths of the IRAC and MIPS-24 filters.

are derived by convolving the model spectra with the IRAC and MIPS-24 filter response curves, as provided by the *Spitzer* Science Center web page. The colours are here computed as ratio of flux densities (in Jy, i.e. per unit frequency).

5.1.1. HII regions with Cloudy

HII regions are possibly the most prominent class of sources in our images. We modelled them with version 05.07 of Cloudy, last described by Ferland et al. (1998) (see also Ferland 2003). The central star was taken to be a $\log g = 4$ Kurucz model (Kurucz 1979) at $T_{\rm eff} = 37\,000$ K, as modified by Rubin to better account for the stellar flux in the model atmospheres between 41 eV and 54 eV. In all cases, we assumed a stellar ionising luminosity of 10^{49} s^{-1}, spherical geometry, constant gas density, a covering factor of 0.005, and a metal abundance of 50% solar.

Grains were "turned on" in the Cloudy models so that heating and cooling of the grains and the gas are calculated in a self-consistent way. A standard PAH distribution is included in the grain population, with treatment of photoelectric heating and collisional processes (see Ferland et al. 1998). We did not explicitly introduce a photo-dissociation region (PDR) in the calculations.

We accounted for the range in typical HII region parameters by varying the outer radius and the total hydrogen density so as to roughly follow the well-known size-density $n_e \sim D^{-1}$ relation for HII regions (Garay & Lizano 1999; Kim & Koo 2001). Four models were calculated with the following pairs in size-density space with density given first in cm^{-3} followed by outer radius in pc: (1000,2); (100,10); (20,30); (10,60).

The resulting spectra are shown in Fig. 10, where the (blue) short-dashed line shows (100,10); the (cyan) dotted line (20,30); the (green) long-dashed line (10,60); and the (red) solid line (1000,2). It can be seen from the figure that varying the density by a factor of 100 drastically changes the PAH emission and its dominance relative to the continuum. Since the PAHs in most HII regions originate in the surrounding PDR rather than in the ionised region itself (e.g Whitney et al. 2004; Churchwell et al. 2004; Dopita et al. 2006), the simulations may not be truly representative of HII regions unless a PDR is absent. However,

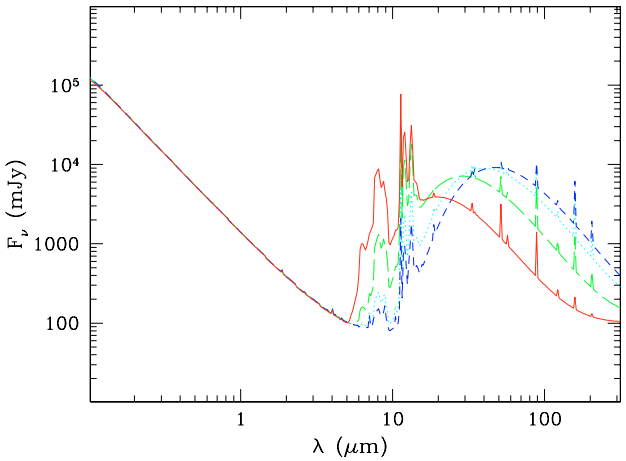

Fig. 10. Spectra obtained with Cloudy code, for the four models. The parameter pairs in size-density space with density given first in cm^{-3} followed by outer radius in pc are represented by the (blue) short-dashed line for (100,10); the (cyan) dotted line (20,30); the (green) long-dashed line (10,60); and the (red) solid line (1000,2).

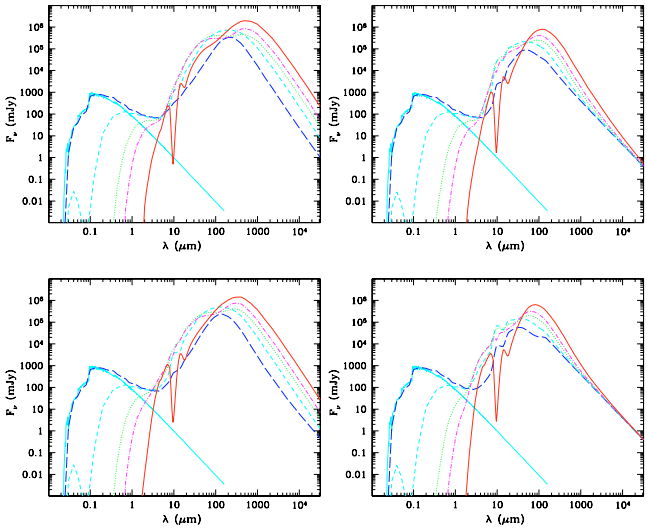

Fig. 11. The resulting *DUSTY* spectra. We plot only 5 values of A_V, namely 0.1, 2.15, 10.0, 21.5, and 100 (shown as long-dashed, short-dashed, dotted, dot-dashed, and solid lines, respectively). Also shown (as a heavy solid line which ends at $\lambda \sim 100$ μm) is the input stellar spectrum of a 3 Myr starburst from SB99. The *upper panels* show $T_{\rm in}$ = 300 K, and the *lower ones* $T_{\rm in}$ = 600 K. The *left panels* show thick shells ($R_{\rm out}$ = 10 000), and in the *right panels* thin ones ($R_{\rm out}$ = 100).

they clearly span a wide range in IR peak wavelength and PAH strength, so should be adequate for helping to interpret the IRAC/MIPS24 diagnostic diagrams.

5.1.2. Embedded HII regions with *DUSTY*

The HII regions we have modelled with Cloudy are basically optically thin, because we have not performed multiple iterations on the solution. Moreover, even with iteration, optical depth effects in the dust itself are not taken into account in the Cloudy formalism. Hence, to better model compact and ultra-compact HII regions which are expected to be embedded in an opaque dust cocoon, we have run a series of models with *DUSTY* (Ivezic & Elitzur 1997). *DUSTY* solves semi-analytically the radiative transfer physics in a dust envelope by exploiting the self-similar nature of the problem. The dust is located in a shell external to the HII region itself. The program allows for a variety of spherical shell configurations, and provides a realistic spread of dust temperatures as the radiation field changes with distance from the source. At the same time, this code suffers from some limiting assumptions, such as spherical symmetry, no treatment of stochastic processes for PAH emission, and the decoupling of the gas from dust. Nevertheless, for our purposes, it is a powerful tool with which to investigate the dust continuum emission from young dust-enshrouded stars and star clusters.

With *DUSTY*, it is necessary to specify the temperature at the inner radius of the dust shell, $T_{\rm in}$ which, for a given incident radiation field, determines the inner radius of the region, $R_{\rm in}$. The radial distribution of the dust is described through the ratio of the outer radius to the inner one, $Y_{\rm out}$ ($\equiv R_{\rm out}/R_{\rm in}$), and the power-law exponent p describing the radial fall-off R^p. In all cases, we adopted a standard "MRN" size distribution (Mathis et al. 1977), and a standard dust composition (Draine & Lee 1984). Finally, we must specify the radial optical depth A_V which, for a given geometry, fixes the dust mass. The *DUSTY* models were calculated for 10 values of A_V, ranging logarithmically from 0.1 to 100 (specifically 0.1, 0.215, 0.464 for each decade in A_V). We adopted single-zone models, with only one stratum in the shell.

Two temperatures were input for $T_{\rm in}$, 300 K and 600 K, which correspond roughly to the range observed in extragalactic HII regions (Hunt et al. 2005). Because of the non-negligible thickness of the dust shell, such relatively high temperatures at its inner rim are also required to explain the *average* temperatures observed in Galactic HII regions (Conti & Crowther 2004; Giveon et al. 2007). We fixed the power-law exponent p to −0.2 as a compromise between uniform regions and those with a steeper fall-off. This exponent strongly affects the amount of cool dust in the shell, but does not significantly influence the MIR portion of the spectrum that we are examining with the IRAC/MIPS-24 diagnostic diagrams. The thickness ratio $Y_{\rm out}$ varied from 10 to 10 000; $Y_{\rm out}$ also controls the amount of cool dust in the shell as thicker shells have proportionately more cool dust.

To model the exciting star cluster input to *DUSTY*, we incorporated the Starburst 99 simulations (SB99, Leitherer et al. 1999). Because we are interested in *young, dusty* star clusters, a single age of 3 Myr was used. SB99 takes into account the nebular continuum emission which can dominate the near-infrared (2 μm−4 μm, NIR) spectral range, and thus could in principle significantly influence our IRAC colour diagrams (see below). In practice, the slope of the input spectrum of a 3 Myr starburst is quite similar to the star used for the Cloudy simulations, at least down to 0.1 μm, so we expect few systematic differences in the dusty star clusters modelled with *DUSTY* relative to the Cloudy models. The metallicity of the input spectrum was taken to be 20% solar; this was to better account for possible lower-metallicity embedded sources in the outer disk. However, as illustrated below, this choice of metallicity does not significantly affect the resulting IRAC/MIPS-24 colours.

We show examples of the resulting *DUSTY* spectra in Fig. 11. Here we plot only 5 values of A_V, namely 0.1, 2.15, 10.0, 21.5, and 100 (shown as long-dashed, short-dashed, dotted, dot-dashed, and solid lines, respectively). Also shown (as a heavy solid line which ends at $\lambda \sim 100$ μm) is the input stellar spectrum of a 3 Myr starburst from SB99. The figure clearly shows the importance of nebular continuum emission and the onset of warm dust in the spectral region sampled by IRAC.

5.1.3. Blackbodies

To illustrate the similarity between the emission from stellar populations and blackbodies in the IRAC bands, we also calculated blackbody spectra at temperatures ranging from 100 000 K to 300 K. In the IRAC/MIPS spectral region, there is virtually no difference among the blackbodies from 100 000 K to 3500 K. As expected, their colours are also very similar to the SB99 simulations of the stellar populations in a 3 Myr cluster.

5.1.4. Interstellar medium with PAH features

An example of the spectrum of the diffuse ISM at high Galactic latitudes was also included in the diagnostics. The spectrum was taken from Fig. 8 of Li & Draine (2001), and the digital version was kindly provided by B. Draine. In the IRAC/MIPS-24 spectral range, the diffuse high-Galactic latitude ISM shows extremely strong PAH emission, superimposed on a rising continuum.

5.1.5. Reflection nebula NGC 7023

NGC 7023 is a well-studied PDR that, because of its proximity, is an excellent source to study the physical processes occurring in such regions. It is a reflection nebula illuminated by a B3Ve star, and is located in a cavity of the molecular cloud. This cavity hosts a dense PDR with its peak located away from the star itself (Fuente et al. 2000). We obtained the short-wavelength portion of the ISO spectrum of this object from the uniform database published by Sloan et al. (2003). Like the diffuse ISM, NGC 7023 also shows relatively strong PAH features superimposed on a rising continuum.

5.1.6. Results

The IRAC and IRAC/MIPS-24 diagnostic diagrams relative to the models described above are shown in the bottom panels of Figs. 12−14. Blackbodies are depicted by filled black circles. NGC 7023 is represented by a (yellow) triangle, the diffuse high-latitude ISM by an inverted (cyan) triangle, the SB99 simulations by (grey) diamonds. The Cloudy HII region is represented by filled green squares. Finally, the *DUSTY* models are represented by filled ($T_{\rm in}$ = 300 K) and empty ($T_{\rm in}$ = 600 K) circles, for a variety of shell thickness $Y_{\rm out}$ = 10 (solid), 100 (dashed), 1000 (dash-dot) and 10 000 (dotted line).

There are several interesting features that can be noticed in the plots. First, a PAH-dominated spectrum such as the diffuse ISM, the small dense Cloudy HII region, and the reflection nebula have virtually identical IRAC colours to some of the $T_{\rm in}$ = 300 K *DUSTY* models. The implication here is that strong PAH features can be easily confused with a rising continuum in the MIR. The only way to resolve the ambiguity is through detailed spectral information *or by using the 24 μm filter in conjunction with the IRAC 8 μm one*. Indeed, our plots show that only 2 IRAC filters, together with MIPS-24, are sufficient to separate strong continuum emission in the MIR from strong PAH features. Second, Fig. 12 shows that strongly embedded sources (e.g., $A_V \sim 100$) occupy a well-defined region in the IRAC colour diagram. This may potentially be useful for singling out ultra-compact dusty HII regions from our 24 μm source catalogue. Third, stars (roughly equivalent to 3500 K blackbodies) occupy a well-defined region in both diagrams, and should therefore be easily separable from other classes of objects.

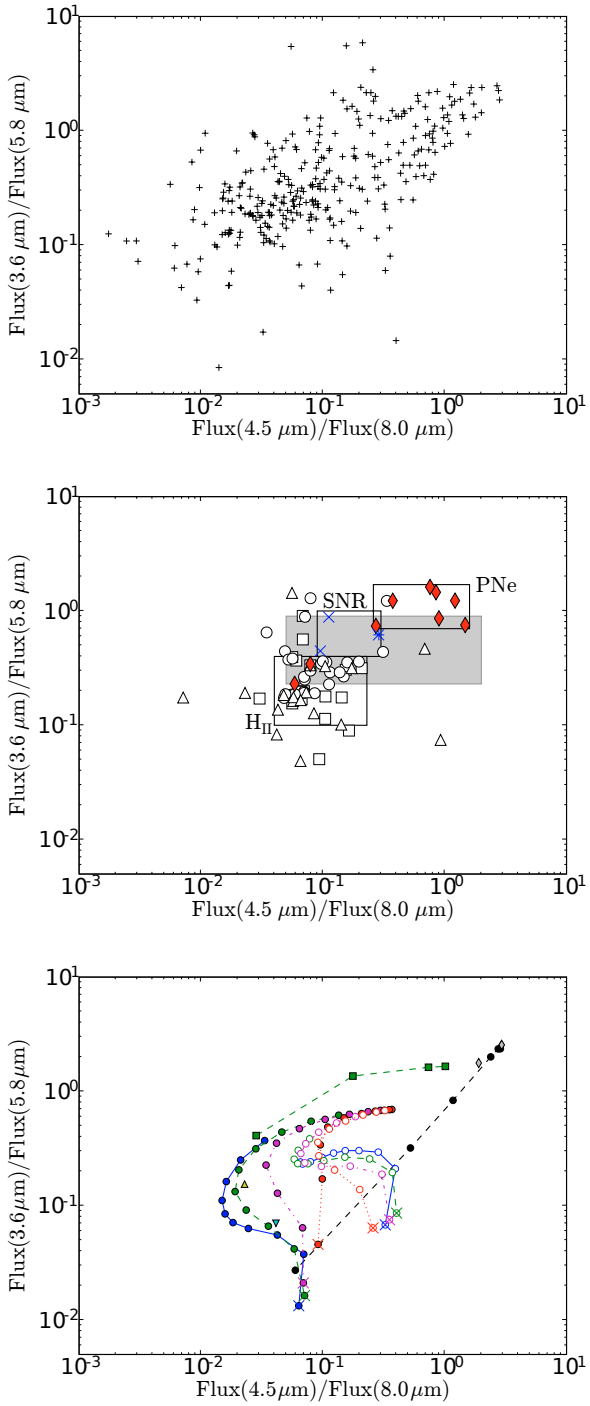

Fig. 12. *Bottom panel*: blackbodies are depicted by filled (black) circles. NGC 7023 is represented by a (yellow) triangle, the ISM by Draine by an inverted (cyan) triangle, the SB99 simulations by (grey) diamonds. The Cloudy HII region is represented by filled (green) squares. Finally, the *DUSTY* models are represented by filled ($T_{\rm in}$ = 300 K) and empty ($T_{\rm in}$ = 600 K) circles, for a variety of shell thickness $Y_{\rm out}$ = 10 (solid), 100 (dashed), 1000 (dash-dot) and 10 000 (dotted line). Different values of A_V (logarithmically from 0.1 to 100 mag) for a given $T_{\rm in}$ and $Y_{\rm out}$ are connected by the different lines; the highest value of A_V is marked by ×. *Middle panel*: the open symbols represent the HII regions selected in IR (squares), radio (triangles) and optical (circles). The (blue) crosses represent the SNRs optically selected and the (blue) plus the SNRs radio selected. The filled (red) diamonds represent the PNe. The open rectangles delineate the zones occupied by the majority of sources of a given type. The grey rectangle delimits the zone of molecular shocked SNRs (Reach et al. 2006). *Top panel*: the 24 μm sources are depicted by (black) pluses.

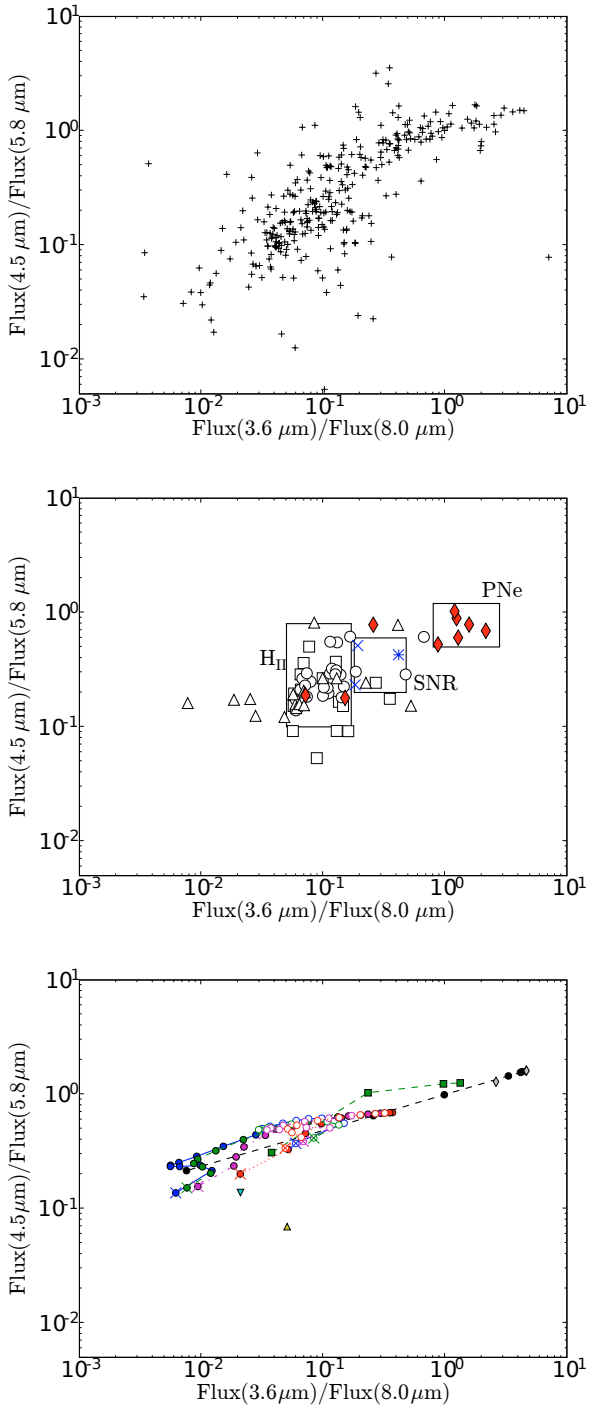

Fig. 13. Same as Fig. 12, but for different IRAC flux ratios.

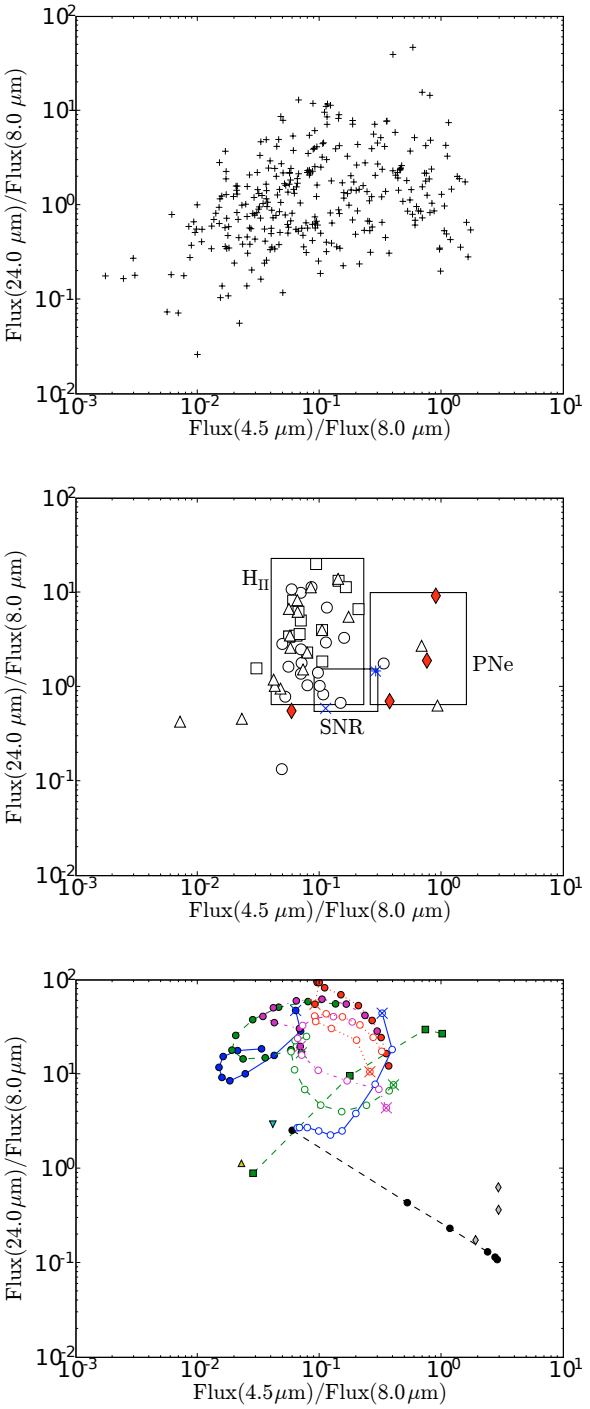

Fig. 14. Same as Fig. 12, but now including the MIPS 24 μm flux ratio.

On the negative side, the *DUSTY* model predictions in the IRAC/MIPS-24 diagram are not easily distinguishable from Cloudy predictions. Moreover, even the highly embedded clusters do not occupy a distinct region in the colour diagrams. This makes the use of IRAC bands necessary, in order to better separate high extinction regions from optically thin ones.

5.2. Observational diagnostic diagrams

A comparison of the IRAC colours of the models+templates vs. observations of the different kinds of nebulae of Sect. 4 is shown in Figs. 12 and 13. Diagnostic diagrams using IRAC colours were presented by Reach et al. (2006) (focusing on SNRs emission mechanisms) and by Cohen et al. (2007). We present two versions of the IRAC diagram, in order to better assess the diagnostic value of the different ratios. We also propose in Fig. 14 a new diagnostic diagram involving the 24 μm MIPS channel which allows us to disentangle some degeneracies present when using only IRAC colours. In the next section, will use both the theoretical colour diagnostics and the observed colours of known-type objects to investigate the nature of sources selected at 24 μm.

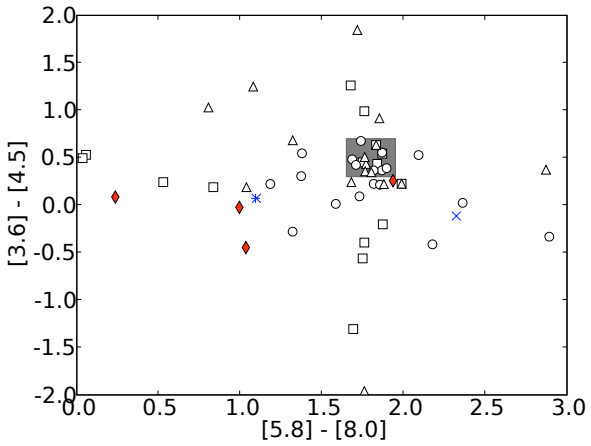

Fig. 15. Diagnostic diagrams in magnitude, for comparison with Cohen et al. (2006). The open symbols represent the HII regions selected in IR (squares), radio (triangles) and optical (circles). The (blue) crosses represent the SNRs optically selected and the (blue) plus the SNRs radio selected. The filled (red) diamonds represent the PNe. Two radio HII regions are lying outside the limits of the displayed plot.

5.2.1. HII regions

In the first IRAC colour diagram (see the middle panels of Figs. 12 and 13), we find a concentration of HII regions in the zone dominated by PAH emission (see Reach et al. 2006). In the same zone, lie the reflection nebulae NGC 7023 and the diffuse Galactic ISM as well. The dispersion in the colours of HII regions makes it difficult to separate them from SNRs and PNe. Statistically, the HII regions are more concentrated near the regions defined by low values of the two shortest IRAC channels and/or equivalently high values of the two longer IRAC wavelengths. The most intense PAH bands (6.2, 7.7, 8.6 μm) are located in the 5.8 and 8.0 μm channels and this may explain the colours of HII regions.

We compared the IRAC colours of our catalogued HII regions with the diffuse HII regions studied by Cohen et al. (2006). Upon conversion to their magnitude scale (Pahre et al. 2004), we find the IRAC-colour distributions to be mutually consistent.

5.2.2. Supernovae remnants

As a word of caution, since (especially young) SNRs are often associated with HII regions, they are often hard to discern and to measure photometrically given the crowding and confusion in the field. In the colour diagrams, the few detected SNRs lie between the HII regions and the PNe, generally closer to the HII regions.

Since the colours of pure synchrotron emission are never observed, there are several alternative emission mechanisms for the IR radiation that have been proposed by Reach et al. (2006) such as shocked molecular lines, shocked ionic lines, and PDR PAH emission. About half of their SNRs have colours consistent with molecular shocks, 17% are consistent with ionic shocks, and 22% with PAH emission from unshocked ISM. The others are thought to represent a mixture of shock types. All our 4 SNRs appear to belong to the class of shocked molecular emission (see the – grey – filled rectangle in the middle panel of Fig. 12), that is shocked molecular gas cooling mainly via MIR emission lines. Also, optically, SNRs appear as shock-heated emission nebulae (Gordon et al. 1999), confirming the prevalence of the two shock mechanisms described by Reach et al. (2006). The colours of our SNRs are also close to the colours of some HII regions. Note that the colours of the SNRs could depend of the epoch at which the SNR is observed (for instance because of the onset or decrease of shocks as they expand into the ISM).

5.2.3. Planetary nebulae

With few exceptions, catalogued PNe are confined to a region characterised by low values of the 5.8 and 8.0 μm emission, the bandpasses where PAHs are believed to contribute substantially to the IR emission. Indeed, PNe spectra usually show an absence or very weak presence of PAH, as noted by Bernard-Salas et al. (2002) with *ISO* and by Bernard-Salas et al. (2004) and with Bernard-Salas et al. (2006) *Spitzer*. In the 4.5 μm band, the [Mg iv] 4.485 μm and [A vi] 4.530 μm lines could give an additional contribution for high-excitation PNe (Cohen et al. 2005). Thus, in absence of detailed spectral information *Spitzer* colours can provide some diagnostics to help to identify PNe candidates (see also Hora et al. 2004).

6. The 24 μm sources in M 33

Spitzer images provide a unique opportunity to compile vast catalogues of MIR discrete sources down to stellar luminosities for galaxies in the Local Group. In the present section we describe and discuss some features of the catalogue of 24 μm sources (24Ss) which we have generated for M 33. In the first subsection, we describe the source selection criterion and flux measurements; in the second subsection, we investigate their nature in light of both theoretical and observational diagnostic diagrams; in the last subsection we present their luminosity function.

6.1. 24 μm source catalogue

To select and measure individual sources from the 24 μm image, we used the SExtractor software (Bertin & Arnouts 1996). Using a convolution with a Gaussian filter we claim a detection when the source area is larger than 10 pixels and the peak signal-to-noise ratio is at least 10 times the local background. Guided by the galaxy pattern traced by the 24 μm diffuse emission, we removed spurious sources such as foreground stars or artifacts due to map edge effects. The final catalogue comprises 515 objects; the positions are listed in Table 3. The brightest sources at 24 μm are located in the central region and along the spiral arms. Fainter sources are more smoothly distributed but still follow the flocculent pattern of the galaxy.

6.2. Nature of the 24 μm sources

Perhaps not surprisingly, sources in our 24 μm catalogue turn out to have a higher detection rate than any of the other kinds of objects considered in the previous sections. This is particularly marked at 5.8 μm where the detection rate for the 24 μm sample is much higher than for HII regions (see Fig. 7) although, as seen in Fig. 9, the averaged SED of the 24Ss is similar to the one of HII regions.

The position of the 24Ss in the colour diagrams are illustrated in the top panels of Figs. 12–14. In Fig. 12, the region with the highest concentration matches well the one of HII regions. However the distribution of 24 μm sources extends into the regions populated by SNRs and PNe. The comparison with the theoretical models indicates a paucity of sources with high

extinction. However, as Fig. 12 shows, neither a pure blackbody, Cloudy, or the two *DUSTY* models can alone reproduce the colour distribution of the 24 μm sources. Figure 13 shows a clear departure of the 24Ss sample from the expected narrow 4.5/5.8 colour dispersion. Such departure is particularly marked in the red tail of the distribution where both 24Ss and known-type sources tend to have colours similar to the PDR observed in the reflection nebulae NGC 7023.

The hybrid IRAC-24 μm MIPS colour diagnostics of the selected sources are illustrated in Fig. 14. No 24S displays a 24/8.0 μm flux ratio as high as the *DUSTY* models with shell inner temperature $T_{\rm in}$ = 300 K; the warmer models ($T_{\rm in}$ = 600 K) seem more appropriate to describe their physical conditions. The range spanned by the 24/8.0 ratio in the 24 μm sources is large but similar to the one covered by the catalogued HII regions, indicating that in both samples the contribution from PAH features may vary widely. So, 24Ss with both a low 4.5/8.0 and a low 24/8.0 ratio could well be HII regions with high PAH emission (see, for instance, the location of the radio-selected HII regions). The Cloudy HII region simulations seem to match well the colours of the 24Ss, in spite of their large scatter. On the contrary, the observations rule out most stellar colours: both pure blackbodies and the SB99 templates. However, as above, the general agreement between any single model and the 24Ss distribution in the colour diagrams is unsatisfactory; such a trend is probably due to a variable PAH component which is not considered in most of our templates (but see loci of NGC 7023 and the ISM). In the next section, we will select a subsample of 24Ss associated with the Hα emission. These sources, likely to be optically visible HII regions, achieve a better agreement with low-extinction models.

6.3. Luminosity function of 24 μm sources

The 24 μm emission of M 33 within an ellipse of major axis 40′ and axial ratio of 0.62 is 40.9 Jy. At a distance D = 840 kpc, such ellipse corresponds to a circle at galactocentric distance of 4.8 kpc inclined by 52° with respect to our line of sight. The 24 μm integrated emission is in good agreement with the value reported by Hinz et al. (2004) (see their Fig. 2) and implies a 24 μm luminosity ($L = \nu F_\nu \times 4\pi D^2$) of 4.3×10^{41} erg s^{-1}. The contribution of the 515 discrete 24Ss amounts to 1.4×10^{41} erg s^{-1}, hence the diffuse component accounts for two thirds of the 24 μm emission.

The cumulative luminosity function of the 515 discrete sources catalogued at 24 μm is shown in Fig. 16. In this figure, the abscissas are reported as flux density at 24 μm in mJy and also as total IR luminosity (TIR). To estimate the TIR luminosity, we follow the prescription of Calzetti et al. (2005) (see their Eq. (1)). The conversion involves the 24 μm and the 8 μm measurements. Since we do not have a detection at 8 μm for all 24Ss, we compute the average 8 μm/24 μm flux ratio for the sources detected in both bands: the average is close to unity and therefore, in the lower panel of Fig. 16, which includes all 24Ss, we use $\log L({\rm TIR}) = \log L(24\ \mu{\rm m}) + 0.908$. As a check, in the upper panel of Fig. 16, we plot the cumulative luminosity function only for the sources detected in both bands, using for each source the measured 8 μm/24 μm flux ratio: the shape and meaning (see below) of the two curves is quite compatible. The main effect, when using a constant average flux ratio, is a slight expansion of the range in L(TIR) by about 0.4 dex, together with a brightening by the same factor.

From the flattening of the faint end of the distribution, we estimate the completeness limit of the catalogue around 1 mJy, or an L(TIR) of 5×10^{37} erg s^{-1} on the averaged scale. That is the bolometric luminosity of a B1.5 V star (Cox 2000) and so our listing should be quite complete even for faint obscured HII regions. Apart from the levelling off at low fluxes, as often observed for HII regions, open clusters, and associations (McKee & Williams 1997), the luminosity function displays a double slope behaviour, markedly steeper at the high luminosity tail. The change of slope, in the simplest scenarios, represents the change of regime between poor and rich clusters, where rich means numerous enough to represent fairly the high-mass IMF (Oey & Clarke 1998). In this framework, the transition point between the two regimes marks the luminosity of the single brightest star; below this value, the observed statistics is modified by the sampling variance. We find that the transition point occurs around $F_\nu(24\ \mu{\rm m})$ = 70 mJy, that is, in the averaged scale, an $L({\rm TIR}) \simeq 5 \times 10^{39}$ erg s^{-1} which, still bolometrically, corresponds to an O3 V star (Vacca et al. 1996). This implies: first, that most of the bright 24Ss are in fact luminous young stellar clusters and, second, that our L(TIR) scale cannot be grossly mistaken. From $F_\nu(24\ \mu{\rm m})$ = 1 to $F_\nu(24\ \mu{\rm m})$ = 70 mJy we fit a power index -0.55 ± 0.01 (plain – red – line) and, for larger values an index -1.09 ± 0.08 (dotted – green – line). It is easily shown that an index about unity, in the log-log cumulative distribution, implies for the rich galactic clusters a distribution $N(L){\rm d}L \propto L^{-2}{\rm d}L$ or, equivalently, $N(n_*){\rm d}n_* \propto n_*^{-2}{\rm d}n_*$, n_* being the number of stellar members. Again, this is precisely the slope observed in the luminosity function of HII regions in late spirals (Caldwell et al. 1991), as well as the slope determined for Galactic clusters and associations, e.g. McKee & Williams (1997).

The brightest source reported in Fig. 16, at $F_\nu(24\ \mu{\rm m}) \simeq$ 1.8 Jy, would be roughly equivalent to an open cluster with around $3.5 \times 10^7\ L_\odot$; assuming that all members (0.06 to 90 $M_\odot$) are on the main sequence, this makes a cluster of some $10^5\ M_\odot$, more than 10^6 members, and more than 1000 ionising (>15 $M_\odot$) stars. On the other side, the faintest detected discrete 24Ss have $F_\nu(24\ \mu{\rm m})$ of 0.1−0.2 mJy, that is $L({\rm TIR}) \simeq 10^{37}$ erg s^{-1}. This is about the bolometric luminosity of zero age main sequence B2 stars (Panagia 1973); so it is possible that these objects are also (the faintest) HII regions and our luminosity distribution appears to precisely match the whole range expected for ionised regions and their complexes. Anyway at low luminosity, especially below $10^4\ L_\odot$, the situation may be more intricate since also evolved stars can contribute substantially, more or less depending on the history of the region, to the population of IR sources; carbon giants, for example, at the distance of M 33 are expected to emit an average $F_\nu(24\ \mu{\rm m}) \simeq 0.25$ mJy (Groenewegen et al. 2007). The nature of the 24Ss will be further explored, by investigating their spatial location within the galaxy and IR colours, in a forthcoming paper.

7. Star formation

7.1. Global star formation rates

In regions of moderate visual extinction, Hα line emission is expected to be a reliable indicator of recent star formation. M 33 has globally a low extinction rate and therefore we can assess the performance of MIR emission as a star formation tracer, by comparing the SFR inferred from MIR emission with that derived from Hα emission.

Hα fluxes were measured on the map of Hoopes & Walterbos (2000) cited earlier (Sect. 2.3) and converted to SFR following Kennicutt (1998). We find a total SFR from Hα, within 5 kpc

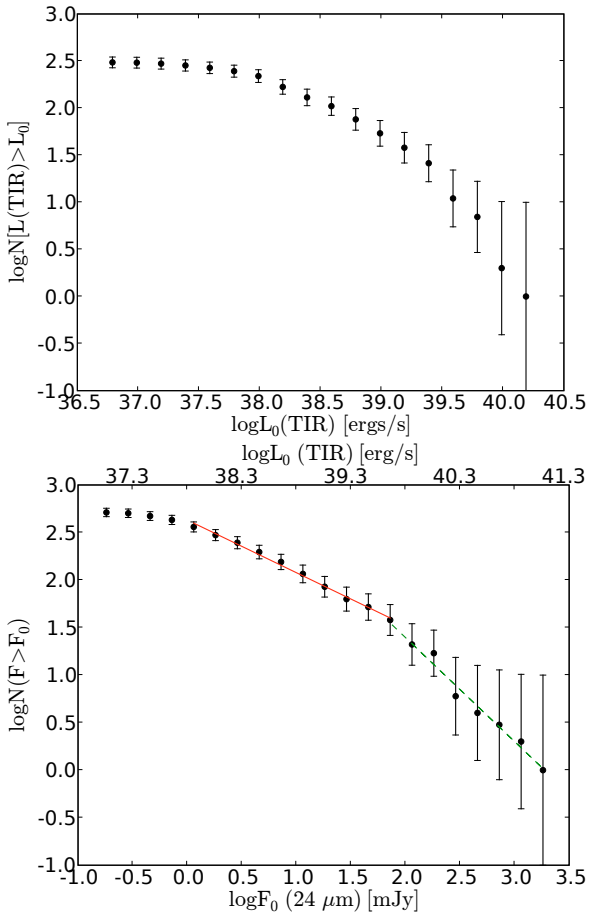

Fig. 16. *Bottom panel*: cumulative distribution of the 24 μm sources. The 24 μm fluxes are reported F_ν(24 μm) (bottom axis), as well as the TIR luminosity L_ν(TIR) (top axis). The linear best fits are depicted by a (red) solid line for the F_ν(24 μm) fluxes between 1 and 70 mJy, and by a (green) dashed line for the F_ν(24 μm) fluxes greater than 70 mJy. *Top panel*: cumulative distribution of the 24 μm sources detected also at 8.0 μm, the TIR luminosity is calculated using for each source the effective 8 μm/24 μm flux ratio.

from the centre, of 0.22 $M_\odot$ yr^{-1} if no extinction corrections are taken into account. On average, this is a reasonable assumption since Tabatabaei et al. (2007b) found a perfect 3.6 cm-Hα correlation for the thermally emitting regions in M 33. In any case, given that the diffuse Hα emission amounts to 40% of the total (Hoopes & Walterbos 2000), an extinction correction of individual sources by $A_V = 1$ on average (as claimed by Devereux et al. 1997 and Israel & Kennicutt 1980), would increase the SFR in the same area to 0.3 $M_\odot$ yr^{-1}.

To estimate the SFR from the IR emission, we used two independent methods: we first estimate the TIR luminosity within a radius of 5 kpc using the data at 8.0 and 24 μm. With a flux of 47.3 Jy, the integrated 8.0 μm luminosity L_ν(8.0 μm) is 4.0 $\times$ 10^{28} erg s^{-1} Hz^{-1}, corresponding to $\nu L_\nu(8) = 1.5 \times 10^{42}$ erg s^{-1}. This is slightly higher than L_ν(24 μm) = 3.5 $\times$ 10^{28} erg s^{-1} Hz^{-1} (or $\nu L_\nu(24) = 4.4 \times 10^{41}$ erg s^{-1}). Such a difference in the 8 and 24 μm flux (47.3 vs. 40.9 Jy) is consistent with the IR SEDs measured in nearby galaxies (Dale et al. 2005), in which IR fluxes at 8.0 μm often exceed those at 24 μm. Using these values, Eq. (1) in Calzetti et al. (2005) yields an L(TIR) = 1.0 $\times$ 10^9 $L_\odot$. The IR SFR is usually computed from the FIR (40−120 μm) luminosity. Calzetti et al. (2000) found that the ratio $L_{\rm IR}(1-1000\ \mu{\rm m})/L_{\rm IR}(40-120\ \mu{\rm m})$ is about 1.75. In our case this translates into a FIR luminosity of 5.8 $\times$ 10^8 $L_\odot$ within a radius of 5 kpc in M 33. This is in good agreement with the value of 6.5 $\times$ 10^8 $L_\odot$ found from the total IRAS fluxes reported by Rice et al. (1990), especially considering that we are including only the central 10 kpc in our estimate. Following the precepts of Buat & Xu (1996) for late spirals, that is SFR [$M_\odot$ yr^{-1}] = 8 $\times$ 10^{-44} L(FIR) with uncertainties of around 50%, we obtain a SFR equal to $0.18^{+0.18}_{-0.07}$ $M_\odot$ yr^{-1}. Within the uncertainties this estimate is compatible with those derived from Hα emission (with and without extinction corrections). We obtain the same value from the TIR–SFR relation by Kennicutt (1998), taking into account the luminosity conversion (TIR vs. FIR).

The second method to derive the SFR from the IR emission involves the linear relation between radio and IR luminosities, and SFR (Yun et al. 2001). Wu et al. (2005) derived SFR directly from the 24 μm luminosity (see their Eq. (1)): in our case, this translates into a SFR of 0.17 $M_\odot$ yr^{-1}. Using the 8 μm luminosity (their Eq. (2)) gives a higher value of SFR, 0.26 $M_\odot$ yr^{-1}, even after subtracting the stellar contribution to the 8 μm flux, ∼10%. Although within the errors of the 24 μm and FIR results (from Rice et al. 1990), the 8 μm value is $\lesssim$40% higher than either the 24 μm or the Hα one. A similar trend was found by Calzetti et al. (2005) in which the 8 μm SFR estimate can be significantly larger in weakly ionized regions such as the disk of M 33 taken globally. This is because the 8 μm emission is produced by more than one mechanism, and thus does not trace SFR as accurately as other IR wavelengths.

In general then both MIR prescriptions for computing the SFR reach a satisfactory agreement with the Hα-derived value and, beyond confirming the adopted SFR computing scheme, implies: a) that actively star forming sites are the main contributors to the MIR emission; b) that mean extinction is low also in the inner HII regions; c) that highly obscured sources do not contribute significantly to the MIR emission.

7.2. Star formation rates in 24 μm sources

We then searched for Hα emission at the location of the 24Ss. This was done in order to compare locally the SFRs from Hα with those from the MIR, but also to check whether sources with and without an Hα counterpart have on average the same IR colours. On the narrow-band (continuum subtracted) Hα image, we performed the photometry of the 24Ss using the same technique described in Sect. 4.1. We find that 293 of the 24Ss are also detected in Hα (within 3.″6). An inspection of the Hα image shows that most bright 24Ss with no Hα counterpart actually lie near an HII region, with an offset which, though larger than the photometric errors, could still be accommodated in case of asymmetries of the Hα shell. This is the case, for example, of some sources along the spiral arms. Some faint 24Ss sources might instead really be absent in the Hα map. Indeed, the percentage of 24Ss undetected in Hα gets higher close to the completeness limit of our survey. We will analyse this finding in more detail in a forthcoming paper. We note however that the luminosity function of the 24Ss with Hα counterpart is totally compatible with the one for the whole sample presented in Sect. 6.3. This is because contamination of the 24 μm sample by non star forming regions happens mostly below the completeness limit of the derived luminosity function.

To estimate the SFR in discrete sources, we adopted the same conversion methods used for the global SFRs and, in order to estimate the TIR luminosity following Calzetti's formula, we restrict our sample of 293 sources to the 186 sources which are also detected in the IRAC bands. The resulting SFRs are compared in

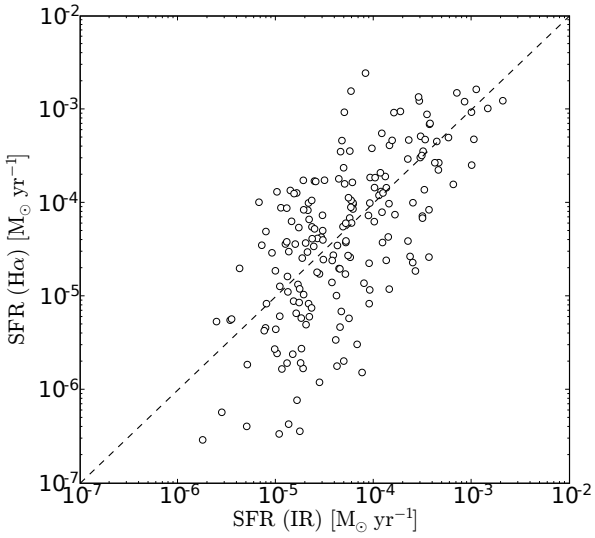

Fig. 17. Comparison of the SFR calculated from the Hα luminosity and from the IR emission based on the 8.0 and 24 μm emissions. The dashed line shows the SFR(Hα) = SFR(IR) relation.

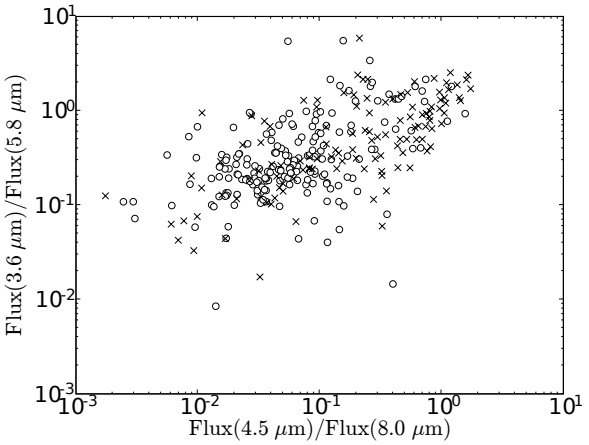

Fig. 18. Diagnostic diagram involving IRAC colours for the 24 μm sources having a Hα counterpart (open circles) and for the 24 μm sources with no Hα counterpart (crosses).

Fig. 17, where the SFR is derived from Hα without any average or individual extinction corrections and the FIR fluxes have been converted to SFR as in the previous subsection: SFR [$M_\odot$ yr^{-1}] = 8×10^{44} L(FIR). The scatter about the line of slope unity is large, roughly a factor of 5 (1σ), and it is difficult to assess the presence of any systematic deviation. The scatter itself, given its magnitude, cannot be imputed to extinction only. Most of the variance is likely linked to the uncertainties intrinsic to the methods used to infer SFRs. A very similar plot can be obtained using the SFR estimated only from the 24 μm emission (see previous subsection) of the discrete sources and is consequently not shown here.

We can compare the IR colours of the latter sample with those of the complementary sample made up by the 121 24Ss with no Hα counterpart, selecting sources detected in all IRAC and MIPS-24 bands. One such diagram is in Fig. 18 and should be compared with the equivalent diagnostic diagram of Sect. 5. The 24Ss without Hα actually seem to be less dusty sources than those emitting also in Hα, a trend confirming that 24Ss with no Hα are not more embedded into dust.

8. Summary and conclusions

This is the first in a series of papers aiming to investigate the star formation history in M 33 by means of the IR data from *Spitzer*. We retrieved and reduced IRAC and MIPS data producing maps roughly the size of the entire star forming galaxy disk. These were used to study the nature of the MIR emission, both globally (large scale structure of dust emission) and locally (by means of discrete sources). Our main results are the following:

- On large scales, the 3.6/4.5 and 5.8/8.0 ratios are remarkably constant. The 3.6 and 4.5 μm emission mainly arises from point sources while the 5.8 and 8.0 μm bands present more diffuse emission following the morphological pattern of the galaxy (spiral arms). The 8.0/24 ratio is also rather constant suggesting a tight link between PAH and VSG properties. On the other hand, the 3.6/5.8 and 4.5/8.0 ratios reveal the flocculent spiral structure in M 33, because of the increasing dominance of the ISM toward longer wavelengths. The distribution of cooler dust is investigated via the MIPS images: the 24 and 70 μm emissions match closely, while the 160 μm band reveals a more diffuse character in the cold-dust emission. The 24 and 70 μm are also more tightly correlated with the Hα emission.
- In the four IRAC and 24 μm MIPS bands, we performed photometry of catalogued discrete sources of various type, including HII regions, SNRs and PNe. We present the detection rates in each band for the various types of object, together with their IR SEDs. For all types of objects, a drop at 4.5 μm is observed, likely due to the contribution of emission features or to the decreasing contribution of photospheric emission from the central star.
- The IR colours of HII regions, SNRs and PNe are used to define diagnostic diagrams. We observe a continuity among the various types: the HII regions appear more dusty than the PNe, which behave more like stellar objects. We also compared these colours with colours predicted by models (such as Cloudy, *DUSTY*, SB99, pure blackbody emission). The diagnostics based on IRAC alone cannot disentangle the different theoretical models, but usage of hybrid IRAC+24 μm colours allows the removal of some of the degeneracies. HII regions are better modelled by pure Cloudy HII regions (including PAHs) and by *DUSTY* models with inner-shell temperatures around 600 K and low extinction.
- We have compared the colours of some of the known-type objects in M 33 with similar objects in our Galaxy (HII regions) or in the LMC (SNRs) and, although with some scatter, we found good agreement for the location of the sources in the colour diagrams.
- From our 24 μm image, we extracted a blind catalogue of 515 discrete sources, on which we performed photometry in the IRAC, and 24 μm MIPS bands and in Hα. Their colours match closely those of known-type sources, and in particular those of HII regions. Consequently, the models which better describe the nature of the 24 μm sources are also pure Cloudy HII regions and low-extinction warm ($T_{\rm in}$ = 600 K) *DUSTY* models.
- The total 24 μm flux of the 515 discrete sources amounts to 1.4×10^{41} erg s^{-1} while the diffuse emission, that is the residual flux, amounts to twice this value.
- We present the IR luminosity function of our 24 μm sources, as a function of the 24 μm flux and as well as a function of the total IR luminosity (estimated from the 8.0 and 24 μm bands). The luminosity ranges from values typical of the faintest ionising stars to those of very large star formation

complexes. The shape (double-sloped) is the same as that observed for Galactic HII regions and star complexes, though AGB stars could contribute significantly to the faintest bins.
– Within a radius of 5 kpc in M 33, we estimate a total IR luminosity of $1.0 \times 10^9\ L_\odot$ and the FIR luminosity is about $5.8 \times 10^8\ L_\odot$. This translates into an estimate of the SFR of $0.2\ M_\odot\ \mathrm{yr}^{-1}$, in very good agreement with the SFR inferred from Hα emission.
– The relation between 24 μm emission and HII regions is also investigated by searching directly for Hα counterparts of the 24 μm sources. About half of the 24 μm sources are very closely associated with Hα while the remaining ones are more distant from an Hα knot than the allowance by positional uncertainties. The SFR for the single sources in IR and Hα are consistent but the scatter is rather large and not imputable to extinction alone.
– The IR colours of the 24 μm sources with and without Hα counterparts are quite similar. If anything, upon comparison with the theoretical diagnostics, those with Hα appear more dusty than the others.

Acknowledgements. We would like to thank Rene Walterbos for providing us the Hα image of M 33, Laura Magrini for the complete list of optical HII regions, and Bruce Draine for the digital version of a diffuse ISM spectrum. The work of S. V. is supported by a INAF-Osservatorio Astrofisico di Arcetri fellowship. The Spitzer Space Telescope is operated by the Jet Propulsion Laboratory, California Institute of Technology, under contract with the National Aeronautics and Space Administration. This research has made use of the NASA / IPAC Extragalactic Database, which is operated by JPL /Caltech, under contract with NASA.

References

Allamandola, L. J., Tielens, G. G. M., & Barker, J. R. 1989, ApJS, 71, 733
Arendt, R. G. 1989, ApJS, 70, 181
Bernard-Salas, J., Pottasch, S. R., Feibelman, W. A., & Wesselius, P. R. 2002, A&A, 387, 301
Bernard-Salas, J., Houck, J. R., Morris, P. W., et al. 2004, ApJS, 154, 271
Bernard-Salas, J., Peeters, E., Sloan, G. C., et al. 2006, ApJ, 652, L29
Bertin, E., & Arnouts, S. 1996, A&AS, 117, 393
Borkowski, K. J., Williams, B. J., Reynolds, S. P., et al. 2006, ApJ, 642, L141
Buat, V., & Xu, C. 1996, A&A, 306, 61
Caldwell, N., Kennicutt, R., Phillips, A. C., & Schommer, R. A. 1991, ApJ, 370, 526
Calzetti, D., Kinney, A. L., Ford, H., Doggett, J., & Long, K. S. 1995, AJ, 110, 2739
Calzetti, D., Armus, L., Bohlin, R. C., et al. 2000, ApJ, 533, 682
Calzetti, D., Kennicutt, Jr., R. C., Bianchi, L., et al. 2005, ApJ, 633, 871
Churchwell, E., Whitney, B. A., Babler, B. L., et al. 2004, ApJS, 154, 322
Ciardullo, R., Durrell, P. R., Laychak, M. B., et al. 2004, ApJ, 614, 167
Cohen, M., & Barlow, M. J. 2005, MNRAS, 362, 1199
Cohen, M., Green, A. J., Roberts, M. S. E., et al. 2005, ApJ, 627, 446
Cohen, M., Green, A. J., Meade, M. R., et al. 2006, ArXiv Astrophysics e-prints
Cohen, M., Green, A. J., Meade, M. R., et al. 2007, MNRAS, 374, 979
Conti, P. S., & Crowther, P. A. 2004, MNRAS, 355, 899
Corbelli, E. 2003, MNRAS, 342, 199
Corbelli, E., & Salucci, P. 2000, MNRAS, 311, 441
Cox, A. N. 2000, Allen's astrophysical quantities, 4th edn. (New York: AIP Press; Springer), ed. A. N. Cox
Dale, D. A., Bendo, G. J., Engelbracht, C. W., et al. 2005, ApJ, 633, 857
Desert, F.-X., Boulanger, F., & Puget, J. L. 1990, A&A, 237, 215
Devereux, N., Duric, N., & Scowen, P. A. 1997, AJ, 113, 236
Dopita, M. A., Fischera, J., Crowley, O., et al. 2006, ApJ, 639, 788
Draine, B. T. 2003, ARA&A, 41, 241
Draine, B. T., & Lee, H. M. 1984, ApJ, 285, 89
Duric, N., Gordon, S. M., Goss, W. M., Viallefond, F., & Lacey, C. 1995, ApJ, 445, 173
Engargiola, G., Plambeck, R. L., Rosolowsky, E., & Blitz, L. 2003, ApJS, 149, 343
Fazio, G. G., Hora, J. L., Allen, L. E., et al. 2004, ApJS, 154, 10
Ferland, G. J. 2003, ARA&A, 41, 517
Ferland, G. J., Korista, K. T., Verner, D. A., et al. 1998, PASP, 110, 761
Freedman, W. L., Wilson, C. D., & Madore, B. F. 1991, ApJ, 372, 455
Fuente, A., Martin-Pintado, J., Rodriguez-Fernández, N. J., Cernicharo, J., & Gerin, M. 2000, A&A, 354, 1053
Garay, G., & Lizano, S. 1999, PASP, 111, 1049
Gerardy, C. L., Meikle, W. P. S., Kotak, R., et al. 2007, ArXiv Astrophysics e-prints
Giveon, U., Sternberg, A., Lutz, D., Feuchtgruber, H., & Pauldrach, A. W. A. 2002, ApJ, 566, 880
Giveon, U., Richter, M. J., Becker, R. H., & White, R. L. 2007, AJ, 133, 639
Gordon, S. M., Kirshner, R. P., Long, K. S., et al. 1998, ApJS, 117, 89
Gordon, S. M., Duric, N., Kirshner, R. P., Goss, W. M., & Viallefond, F. 1999, ApJS, 120, 247
Gorjian, V., Werner, M. W., Mould, J. R., et al. 2004, ApJS, 154, 275
Groenewegen, M. A. T., Wood, P. R., Sloan, G. C., et al. 2007, MNRAS, 376, 313
Helou, G., Roussel, H., Appleton, P., et al. 2004, ApJS, 154, 253
Heyer, M. H., Corbelli, E., Schneider, S. E., & Young, J. S. 2004, ApJ, 602, 723
Hinz, J. L., Rieke, G. H., Gordon, K. D., et al. 2004, ApJS, 154, 259
Hippelein, H., Haas, M., Tuffs, R. J., et al. 2003, A&A, 407, 137
Hoopes, C. G., & Walterbos, R. A. M. 2000, ApJ, 541, 597
Hora, J. L., Latter, W. B., Allen, L. E., et al. 2004, ApJS, 154, 296
Hunt, L., Bianchi, S., & Maiolino, R. 2005, A&A, 434, 849
Israel, F. P., & Kennicutt, R. C. 1980, Astrophys. Lett., 21, 1
Ivezic, Z., & Elitzur, M. 1997, MNRAS, 287, 799
Jones, T. J., Woodward, C. E., Boyer, M. L., Gehrz, R. D., & Polomski, E. 2005, ApJ, 620, 731
Kennicutt, Jr., R. C. 1998, ARA&A, 36, 189
Kessler, M. F., Steinz, J. A., Anderegg, M. E., et al. 1996, A&A, 315, L27
Kim, K.-T., & Koo, B.-C. 2001, ApJ, 549, 979
Kurucz, R. L. 1979, ApJS, 40, 1
Leger, A., & Puget, J. L. 1984, A&A, 137, L5
Leitherer, C., Schaerer, D., Goldader, J. D., et al. 1999, ApJS, 123, 3
Li, A., & Draine, B. T. 2001, ApJ, 554, 778
Magrini, L., Cardwell, A., Corradi, R. L. M., Mampaso, A., & Perinotto, M. 2001, A&A, 367, 498
Magrini, L., Corbelli, E., & Galli, D. 2007a, ArXiv e-prints, 704
Magrini, L., Vilchez, J. M., Mampaso, A., Corradi, R. L. M., & Leisy, P. 2007b, ArXiv e-prints, 705
Makovoz, D., & Khan, I. 2005, in Astronomical Data Analysis Software and Systems XIV, ed. P. Shopbell, M. Britton, & R. Ebert, ASP Conf. Ser., 347, 81
Mathis, J. S., Rumpl, W., & Nordsieck, K. H. 1977, ApJ, 217, 425
McKee, C. F., & Williams, J. P. 1997, ApJ, 476, 144
McQuinn, K. B. W., Woodward, C. E., Willner, S. P., et al. 2007, ApJ, 664, 850
Mercer, E. P., Clemens, D. P., Bania, T. M., et al. 2004, ApJS, 154, 328
Neugebauer, G., Habing, H. J., van Duinen, R., et al. 1984, ApJ, 278, L1
Oey, M. S., & Clarke, C. J. 1998, AJ, 115, 1543
Pahre, M. A., Ashby, M. L. N., Fazio, G. G., & Willner, S. P. 2004, ApJS, 154, 229
Panagia, N. 1973, AJ, 78, 929
Perez-Gonzalez, P. G., Kennicutt, Jr., R. C., Gordon, K. D., et al. 2006, ArXiv Astrophysics e-prints
Reach, W. T., Rho, J., Jarrett, T. H., & Lagage, P.-O. 2002, ApJ, 564, 302
Reach, W. T., Rho, J., Tappe, A., et al. 2006, AJ, 131, 1479
Regan, M. W., & Vogel, S. N. 1994, ApJ, 434, 536
Rice, W., Boulanger, F., Viallefond, F., Soifer, B. T., & Freedman, W. L. 1990, ApJ, 358, 418
Rieke, G. H., Young, E. T., Engelbracht, C. W., et al. 2004, ApJS, 154, 25
Saken, J. M., Fesen, R. A., & Shull, J. M. 1992, ApJS, 81, 715
Sloan, G. C., Kraemer, K. E., Price, S. D., & Shipman, R. F. 2003, ApJS, 147, 379
Tabatabaei, F. S., Beck, R., Krause, M., et al. 2007a, A&A, 466, 509
Tabatabaei, F. S., Beck, R., Krause, M., et al. 2007b, ArXiv Astrophysics e-prints
Vacca, W. D., Garmany, C. D., & Shull, J. M. 1996, ApJ, 460, 914
Werner, M. W., Roellig, T. L., Low, F. J., et al. 2004, ApJS, 154, 1
Whitney, B. A., Indebetouw, R., Babler, B. L., et al. 2004, ApJS, 154, 315
Williams, R. M., Chu, Y. ., & Gruendl, R. 2006, ArXiv Astrophysics e-prints
Willner, S. P., & Nelson-Patel, K. 2002, ApJ, 568, 679
Wu, H., Cao, C., Hao, C.-N., et al. 2005, ApJ, 632, L79
Yun, M. S., Reddy, N. A., & Condon, J. J. 2001, ApJ, 554, 803

Online Material

Table 2. Photometry of known type sources (the flag "−99.0" is used when the photometric centre is farther than 3.″6 from the nominal position).

Type	Num.	RA (J2000)	Dec (J2000)	3.6 μm		4.5 μm		5.8 μm		8.0 μm		24 μm		Hα	
		(°)	(°)	F_ν (mJy)	δr	F_ν (mJy)	δr	F_ν (mJy)	δr	F_ν (mJy)	δr	F_ν (mJy)	δr	F (10^{-14} erg s^{-1})	δr
ISO	1	01:33:59.3	30:35:49.2	2.779	2.38	2.248	2.06	24.410	1.86	21.504	1.77	86.133	1.33	161.110	1.01
ISO	2	01:33:09.8	30:27:25	4.570	1.60	3.640	1.47	13.660	1.63	46.120	0.57	106.790	1.73	59.330	0.60
ISO	3	01:33:44.5	30:44:38	3.350	1.14	1.507	1.39	9.098	1.16	24.896	0.95	204.660	0.41	89.796	0.86
ISO	4	01:33:45.5	30:36:51.1	2.000	1.97	3.220	1.51	11.200	2.11	30.649	1.93	57.035	1.94	62.180	1.39
ISO	5	01:33:35.5	30:39:30.5	1.598	1.30	1.566	1.20	10.291	1.53	27.896	1.43	95.377	0.88	18.056	0.76
ISO	6	01:33:35.5	30:39:30	4.060	1.23	1.566	0.79	10.291	1.12	27.896	1.02	95.377	0.49	18.056	0.60
ISO	7	01:33:28.8	30:40:24.7	4.303	1.31	4.589	1.28	21.656	1.81	65.556	1.17	331.663	0.61	84.178	1.47
ISO	8	01:33:33.9	30:41:28.3	6.338	1.89	6.683	1.57	125.460	2.38	71.506	2.21	1434.670	0.87	394.332	2.17
ISO	9	01:33:55.3	30:45:22	1.226	1.72	1.184	1.68	6.228	1.57	18.322	1.91	64.093	1.16	88.720	0.76
ISO	10	01:34:00.2	30:40:48.6	4.552	0.85	5.278	0.89	26.941	0.97	78.783	0.88	493.010	0.83	19.379	0.32
ISO	14	01:34:10.9	30:36:18.1	4.740	1.22	0.921	1.67	5.236	1.63	13.459	1.71	48.906	0.92	72.270	2.10
ISO	16	01:33:36.6	30:20:13.4	3.220	0.84	2.480	0.53	10.200	0.65	11.916	0.53	79.540	0.82	115.650	0.09
ISO	19	01:33:16.5	30:52:49.1	4.883	0.80	10.097	0.82	27.897	0.85	70.689	0.71	942.423	0.97	102.805	0.59
ISO	21	01:33:16.3	30:56:43.8	0.402	2.50	0.488	2.48	1.315	2.14	3.164	1.91	–99.0	–99.0	82.221	2.19
ISO	23	01:34:33.5	30:46:50.5	14.115	2.50	12.607	1.96	25.052	0.93	183.911	1.06	–99.0	–99.0	–99.0	–99.0
ISO	24	01:34:32.1	30:46:59.9	9.463	0.30	5.080	0.97	55.272	0.89	167.831	0.82	264.127	1.59	313.513	0.69
ISO	25	01:34:16.4	30:51:55.1	3.162	1.11	3.228	1.14	35.200	1.19	19.684	1.36	224.650	0.63	98.304	0.47
Hra	5	01:33:16.00	+30:56:45.9	4.570	2.62	3.640	2.47	13.660	1.26	46.120	1.15	106.790	0.92	59.330	1.13
Hra	7	01:33:33.62	+30:32:08.1	4.938	1.04	10.096	1.06	48.730	1.17	71.289	0.99	996.074	0.43	100.845	0.84
Hra	10	01:33:36.53	+30:20:14.4	1.598	0.70	1.542	0.75	9.788	0.91	27.048	0.66	94.753	0.30	18.056	0.85
Hra	11	01:33:39.18	+30:38:06.9	3.220	1.50	2.480	1.21	10.200	0.84	14.362	0.85	79.540	0.64	115.650	0.74
Hra	12	01:33:42.96	+30:44:40.6	0.106	0.59	0.177	0.61	0.227	0.65	0.258	0.88	0.704	1.59	–99.0	–99.0
Hra	13	01:33:43.64	+30:39:07.1	0.074	1.79	0.262	1.77	1.519	1.68	3.996	1.89	33.199	2.24	121.820	0.83
Hra	14	01:33:44.49	+30:44:38.4	1.424	1.50	1.130	1.10	7.748	2.09	23.673	2.44	22.730	0.56	38.496	0.07
Hra	16	01:33:47.86	+30:43:52.6	1.650	1.67	1.482	1.75	9.381	1.54	25.793	1.30	66.974	1.25	89.796	0.84
Hra	17	01:33:50.16	+30:33:46.8	0.768	1.47	0.684	1.55	5.613	1.96	15.975	1.78	16.387	0.60	124.330	0.38
Hra	19	01:33:51.34	+30:43:52.8	0.169	1.91	0.254	2.22	2.035	1.73	6.063	1.83	7.250	1.80	46.670	0.29
Hra	20	01:33:52.57	+30:39:18.4	2.219	1.63	2.290	2.32	11.435	1.57	31.355	1.33	48.001	0.61	39.910	2.83
Hra	22	01:33:57.47	+30:42:16.2	8.613	1.35	94.480	1.20	115.710	1.24	102.012	1.49	64.674	1.11	52.961	1.22
Hra	27	01:34:01.01	+30:43:55.4	2.779	2.78	2.248	2.45	8.453	2.23	21.504	1.96	86.133	1.37	161.110	1.11
Hra	28	01:34:02.21	+30:38:40.7	4.470	0.53	5.188	0.54	26.941	0.59	78.783	0.26	493.010	0.05	19.379	0.33
Hra	29	01:34:06.38	+30:41:45.6	1.266	0.70	1.155	0.61	6.595	0.91	50.250	1.07	23.085	0.72	23.758	0.70
Hra	33	01:34:13.73	+30:34:51.4	1.000	1.55	0.924	1.28	5.719	1.33	129.290	1.42	55.358	0.29	72.270	0.47
Hra	37	01:34:33.13	+30:46:57.3	7.970	0.58	0.848	0.68	5.545	0.77	15.175	0.70	101.800	0.18	122.040	1.47
Hra	40	01:34:41.04	+30:43:29.5	0.364	0.96	0.442	0.88	2.860	1.08	5.227	0.98	59.380	0.80	18.960	0.35
HII	1	1:32:29.5	30:36:07.9	0.119	1.95	0.181	1.92	0.330	1.27	0.915	1.47	–99.0	–99.0	8.850	0.46
HII	9	1:32:45.9	30:41:35.5	0.168	1.00	0.080	0.92	0.130	0.58	1.009	0.52	1.050	0.28	4.400	0.12
HII	17	1:33:10.8	30:18:08.5	0.080	0.96	0.050	0.55	0.090	0.98	0.700	0.78	–99.0	–99.0	4.080	0.25
HII	19	1:33:11.2	30:45:16.4	2.916	0.66	2.941	0.44	10.046	1.22	25.664	1.29	177.960	0.63	117.495	0.24
HII	26	1:33:19.0	30:58:14.3	0.199	0.68	0.088	0.39	0.448	0.25	1.800	1.06	0.242	1.01	4.171	0.22
HII	29	1:33:28.1	31:00:17.2	0.150	1.87	0.136	1.82	0.421	2.28	1.272	2.03	1.060	1.84	13.270	1.15
HII	30	1:33:29.0	30:40:24.8	4.137	1.62	4.457	1.34	21.040	1.72	63.637	1.78	633.390	1.69	82.292	0.24
HII	37	1:33:44.8	31:02:22.0	0.077	2.52	0.066	2.02	0.217	1.55	0.416	1.77	1.378	2.68	13.316	1.37
HII	39	1:33:46.3	30:52:15.0	0.204	0.56	0.195	0.63	1.063	0.69	2.775	0.63	6.940	0.64	5.044	0.31
HII	40	1:33:47.0	30:27:22.8	0.620	0.41	0.410	0.76	1.650	0.27	7.860	0.83	6.190	0.55	21.650	0.18
HII	47	1:33:59.9	30:32:44.3	0.903	0.36	0.950	0.10	3.600	0.20	13.374	0.35	24.020	1.21	40.020	0.30
HII	49	1:34:01.7	30:23:00.6	0.240	2.58	0.120	2.31	0.196	2.43	0.358	1.55	0.634	2.02	2.910	0.67
HII	51	1:34:04.3	31:02:17.9	0.044	1.43	0.031	1.43	0.166	2.35	0.442	1.82	0.610	2.05	4.421	0.38
HII	52	1:34:06.7	30:48:56.4	0.326	0.75	0.302	0.54	1.757	1.24	5.450	1.48	8.930	1.92	24.962	0.43
HII	53	1:34:09.4	30:34:17.0	0.820	1.61	0.597	1.66	2.728	2.19	7.538	2.41	–99.0	–99.0	23.980	0.31
HII	55	1:34:14.4	30:27:40.3	0.120	1.62	0.041	2.39	0.185	0.66	1.186	2.13	–99.0	–99.0	0.248	0.32
HII	62	1:34:36.1	30:45:59.6	0.168	1.50	0.110	1.20	0.488	1.20	1.137	1.15	1.609	2.38	4.619	2.12
HII	64	1:34:37.4	30:34:54.3	0.369	0.93	0.445	0.84	1.935	0.84	5.193	1.08	59.380	1.43	18.960	0.16
HII	65	1:34:38.5	30:32:52.3	0.034	0.35	0.027	0.12	0.149	0.61	0.240	0.53	0.710	1.01	1.080	0.34
HII	67	1:34:39.3	31:02:25.0	0.051	1.93	0.041	1.84	0.294	1.96	0.854	2.05	–99.0	–99.0	6.169	0.64
HII	68	1:34:39.5	30:31:14.2	0.128	0.83	0.116	0.76	0.684	0.66	1.972	0.31	21.350	1.02	1.090	0.33
HII	69	1:34:42.2	30:24:00.5	0.043	0.38	0.046	0.29	0.161	0.32	0.310	0.31	0.210	0.39	1.620	0.28
HII	70	1:34:42.5	30:55:44.5	0.410	0.59	0.440	0.89	1.410	0.15	3.199	0.72	–99.0	–99.0	1.999	0.12
HII	71	1:34:45.5	30:42:24.4	0.200	0.41	0.159	0.18	0.551	0.24	1.590	0.21	1.630	0.75	4.046	0.49
HII	72	1:34:49.2	30:37:27.5	0.052	0.85	0.041	0.81	0.278	0.74	0.831	1.08	2.370	1.40	0.430	0.63
HII	75	1:35:01.6	30:40:02.3	0.069	0.38	0.053	0.35	0.180	0.64	0.940	0.42	–99.0	–99.0	1.456	0.49
HII	76	1:35:02.4	31:00:43.4	0.067	1.17	0.044	1.00	0.153	1.03	0.141	1.16	–99.0	–99.0	2.687	0.70
SNo	25	1:33:23.8	30:26:11.6	0.550	1.40	0.380	0.96	0.890	0.81	1.325	1.87	1.947	1.55	3.310	0.95
SNo	43	1:33:41.7	30:21:01.8	3.590	2.56	2.090	2.21	4.060	2.09	18.670	0.61	11.060	0.54	14.907	1.82
SNo	53	1:33:54.5	30:33:47.7	0.134	2.67	0.070	2.84	0.300	2.71	0.733	2.85	–99.0	–99.0	–99.0	–99.0

Table 2. continued.

Type	Num.	RA (J2000)	Dec (J2000)	3.6 μm		4.5 μm		5.8 μm		8.0 μm		24 μm		Hα	
		(°)	(°)	F_ν (mJy)	δr	F_ν (mJy)	δr	F_ν (mJy)	δr	F_ν (mJy)	δr	F_ν (mJy)	δr	F (10^{-14} erg s^{-1})	δr
SNR	13	1:33:23.78	30:26:11.60	0.550	1.42	0.380	0.99	0.890	1.00	1.319	1.92	1.947	1.68	3.310	0.97
PNe	4	01:32:39.80	+30:37:41.0	0.017	0.23	0.018	0.79	0.023	1.16	0.066	0.69	0.000	6.74	0.164	0.18
PNe	60	01:33:44.38	+30:20:23.7	0.050	2.64	0.035	2.41	0.058	2.73	0.039	2.45	0.361	0.81	0.220	0.19
PNe	79	01:33:54.93	+30:47:13.4	0.156	1.61	0.084	1.46	0.107	1.86	0.099	1.01	0.000	7.18	–99.0	–99.0
PNe	85	01:33:58.38	+30:55:05.2	0.050	2.34	0.041	1.71	0.217	1.61	0.698	1.75	0.389	1.29	0.676	0.87
PNe	106	01:34:12.15	+30:28:57.1	0.160	2.65	0.090	2.85	0.130	2.56	0.074	2.90	0.379	3.43	0.181	1.37
PNe	112	01:34:15.15	+30:44:57.4	0.189	2.04	0.224	2.10	0.251	2.15	0.152	2.34	0.000	7.62	0.185	0.06
PNe	128	01:34:25.55	+30:40:10.9	0.248	0.71	0.157	0.65	0.153	0.39	0.207	0.28	0.394	0.42	0.275	0.37
PNe	133	01:34:31.49	+31:05:24.0	0.023	0.54	0.012	0.69	0.067	0.48	0.152	0.07	0.000	6.63	0.148	0.17
PNe	139	01:34:37.89	+30:27:00.7	0.140	2.20	0.060	2.20	0.114	1.73	0.160	0.88	0.113	0.60	0.210	0.20

Table 3. Photometry of 24 μm sources (the flag "–99.0" is used when the photometric centre is farther than 3.″6 from the nominal position).

Num.	RA (J2000)	Dec (J2000)	3.6 μm		4.5 μm		5.8 μm		8.0 μm		24 μm		Hα	
	(°)	(°)	F_ν (mJy)	δr	F_ν (mJy)	δr	F_ν (mJy)	δr	F_ν (mJy)	δr	F_ν (mJy)	δr	F (10^{-14} erg s^{-1})	δr
1	23.3749767	30.3099105	0.2	2.846	0.13	2.799	0.76	2.934	2.71	2.762	23.59	0.022	–99.0	–99.0
2	23.3614272	30.2907556	0.06	0.646	0.069	0.54	0.33	0.824	1.46	0.956	0.75	0.0	0.32	0.2
3	23.3721103	30.3016896	0.21	1.196	0.1	1.001	0.58	0.522	2.27	0.796	4.59	0.022	5.583	0.24
4	23.3329204	30.3053012	–99.0	–99.0	–99.0	–99.0	0.364	0.527	0.963	1.04	1.286	0.122	–99.0	–99.0
5	23.3358182	30.3040334	0.021	0.72	0.052	0.73	0.105	0.652	–99.0	–99.0	0.7	0.073	–99.0	–99.0
6	23.4435711	30.3038256	0.046	0.592	0.04	0.586	0.148	0.62	0.14	0.643	0.29	0.002	–99.0	–99.0
7	23.4487444	30.3048739	–99.0	–99.0	–99.0	–99.0	–99.0	–99.0	–99.0	–99.0	0.67	0.077	–99.0	–99.0
8	23.4024463	30.3367871	3.22	0.433	2.48	0.557	4.57	0.989	11.998	0.954	79.54	0.001	53.569	0.424
9	23.3768792	30.3196512	0.051	1.954	0.042	2.02	0.21	1.599	2.33	0.926	0.82	0.204	1.16	2.558
10	23.3843288	30.3366678	0.205	2.028	0.191	1.907	1.951	1.054	5.84	0.756	4.258	0.16	2.59	1.505
11	23.48185	30.330103	0.16	0.647	0.14	0.489	0.62	0.823	2.13	1.002	3.64	0.031	11.01	0.243
12	23.4718432	30.3314455	0.074	1.463	0.053	1.31	0.11	0.56	0.47	0.774	5.24	0.016	–99.0	–99.0
13	23.3860886	30.3334663	–99.0	–99.0	0.027	0.932	0.26	1.079	2.06	1.164	3.54	0.121	1.6	1.766
14	23.4064918	30.3470677	0.65	2.978	0.22	2.634	2.52	0.68	14.48	0.386	16.9	0.229	72.49	0.929
15	23.3513249	30.3401814	0.23	2.685	0.16	1.825	0.137	0.609	0.14	0.456	1.05	0.001	–99.0	–99.0
16	23.3882322	30.3414916	–99.0	–99.0	–99.0	–99.0	0.28	0.32	2.08	0.519	0.9	0.002	4.189	0.71
17	23.4370169	30.3513656	1.15	1.087	0.86	0.966	1.4	0.939	1.374	1.071	2.04	0.003	2.951	2.055
18	23.4379955	30.3604276	0.48	1.602	0.4	1.196	1.39	1.172	4.22	1.186	17.56	0.009	22.336	0.215
19	23.410961	30.3512346	0.669	0.362	0.765	0.311	1.17	0.594	1.4	0.622	3.05	0.043	–99.0	–99.0
20	23.2919766	30.3854636	–99.0	–99.0	0.7	2.58	4.79	0.849	15.14	2.412	25.14	0.329	21.901	0.777
21	23.3234794	30.3571074	0.65	1.11	0.49	0.847	0.19	0.281	1.9	0.639	1.02	0.11	0.056	0.51
22	23.414503	30.3611675	0.22	0.289	0.24	0.483	0.2	0.562	0.29	0.613	0.7	0.002	–99.0	–99.0
23	23.4145537	30.3787926	0.47	1.408	0.42	1.42	4.67	1.413	3.556	1.234	19.4	0.041	3.49	1.477
24	23.4855241	30.3733786	–99.0	–99.0	–99.0	–99.0	1.43	2.456	11.96	2.034	4.17	0.055	10.07	0.242
25	23.4387472	30.3656494	–99.0	–99.0	–99.0	–99.0	0.208	0.814	0.52	0.854	1.49	0.002	–99.0	–99.0
26	23.3056383	30.3771194	0.11	2.189	0.07	2.383	1.11	1.69	11.45	2.584	9.12	0.029	9.58	2.557
27	23.5564787	30.3681733	0.12	2.343	0.048	0.428	0.05	0.339	0.234	0.381	1.03	0.001	–99.0	–99.0
28	23.2961441	30.3771633	–99.0	–99.0	–99.0	–99.0	0.56	2.7	5.5	2.201	1.11	0.097	–99.0	–99.0
29	23.2797677	30.3863205	–99.0	–99.0	–99.0	–99.0	–99.0	–99.0	7.93	1.122	6.74	0.037	31.62	2.011
30	23.4006862	30.3774629	–99.0	–99.0	–99.0	–99.0	0.16	0.3	0.69	0.453	2.0	0.001	0.472	1.303
31	23.5000231	30.37729	0.13	0.697	0.12	0.685	0.4	1.315	0.96	1.426	0.38	0.001	–99.0	–99.0
32	23.2887017	30.3916345	0.56	0.913	0.42	1.35	1.203	0.875	3.357	0.7	19.81	1.467	17.273	2.536
33	23.3178801	30.3847881	3.3	0.921	2.22	0.893	1.82	0.948	1.84	0.824	2.72	0.001	0.86	0.899
34	23.3616848	30.3870248	0.89	0.621	1.34	0.575	1.8	0.603	2.15	0.638	2.08	0.032	–99.0	–99.0
35	23.4989082	30.3848985	0.116	0.891	0.069	0.948	0.197	1.048	0.61	1.738	0.3	0.002	2.6	2.811
36	23.2737497	30.3907547	–99.0	–99.0	–99.0	–99.0	–99.0	–99.0	2.46	1.249	3.27	0.077	–99.0	–99.0
37	23.3498559	30.4274082	–99.0	–99.0	–99.0	–99.0	–99.0	–99.0	–99.0	–99.0	97.33	0.006	–99.0	–99.0
38	23.5540474	30.3917149	–99.0	–99.0	–99.0	–99.0	–99.0	–99.0	–99.0	–99.0	0.35	0.001	–99.0	–99.0
39	23.4097494	30.3990514	0.14	0.179	0.07	0.535	0.64	0.651	2.42	0.709	2.92	0.025	0.65	0.32
40	23.2910806	30.4571431	4.57	0.885	3.64	0.82	13.66	2.357	45.75	1.143	106.79	2.577	59.33	0.5
41	23.2954134	30.4612809	3.41	1.515	2.61	1.567	16.95	1.522	50.78	1.518	85.82	0.127	29.423	1.511
42	23.4877339	30.4195854	–99.0	–99.0	–99.0	–99.0	–99.0	–99.0	1.003	0.653	0.53	0.117	2.98	2.508
43	23.5439212	30.432297	0.18	0.798	0.11	0.457	0.96	0.738	4.78	0.831	4.78	0.001	3.597	0.325
44	23.54527	30.4267949	0.038	0.739	0.027	0.725	0.19	0.432	1.8	0.526	1.15	0.055	1.457	2.145
45	23.5583747	30.4298619	0.5	0.861	0.38	0.859	1.39	1.087	1.495	1.186	3.05	0.033	3.42	2.687
46	23.397946	30.4325781	0.54	0.654	0.35	0.479	1.81	0.728	5.65	0.622	7.55	0.014	7.27	0.314
47	23.5581556	30.5800716	–99.0	–99.0	–99.0	–99.0	–99.0	–99.0	–99.0	–99.0	199.76	0.08	–99.0	–99.0
48	23.3472539	30.4430213	–99.0	–99.0	–99.0	–99.0	0.64	1.157	1.196	1.249	0.851	0.152	2.59	2.223
49	23.2869175	30.4975933	–99.0	–99.0	–99.0	–99.0	21.73	1.073	124.86	2.16	75.65	0.065	136.24	0.475
50	23.5539497	30.4581009	0.26	2.823	0.19	2.545	0.38	0.966	4.85	1.384	14.3	0.0	–99.0	–99.0
51	23.4121779	30.4713349	–99.0	–99.0	–99.0	–99.0	–99.0	–99.0	–99.0	–99.0	25.72	0.009	1.65	2.399
52	23.4840991	30.4526648	–99.0	–99.0	–99.0	–99.0	–99.0	–99.0	–99.0	–99.0	1.7	0.229	–99.0	–99.0
53	23.4456607	30.4564383	0.62	0.728	0.294	0.143	0.987	0.377	2.745	0.477	6.19	0.001	21.65	0.371
54	23.4854658	30.4547352	0.093	0.821	0.066	0.836	0.65	0.693	1.816	0.684	3.031	0.978	16.679	1.912
55	23.4825356	30.4578157	2.628	0.683	2.788	0.668	2.771	0.753	2.649	0.713	1.421	0.127	–99.0	–99.0
56	23.5652741	30.4626984	1.66	1.064	1.23	0.84	1.3	0.838	4.11	0.667	11.23	0.004	0.446	2.689
57	23.5485285	30.4544927	0.2	2.315	–99.0	–99.0	0.57	0.444	4.47	0.639	0.87	0.088	1.46	0.398
58	23.238228	30.457635	0.54	1.667	0.19	1.723	0.61	1.159	6.86	0.962	1.41	0.048	–99.0	–99.0
59	23.4668067	30.4518772	0.23	1.505	0.26	1.019	0.21	1.152	0.45	0.758	0.36	0.001	–99.0	–99.0
60	23.3902028	30.5356536	–99.0	–99.0	–99.0	–99.0	71.22	1.952	395.8	0.32	250.56	0.411	136.42	1.246
61	23.5639999	30.4711516	2.95	0.323	3.55	0.284	4.61	0.609	4.247	0.323	17.56	0.0	1.805	0.192
62	23.5964784	30.4621603	–99.0	–99.0	–99.0	–99.0	0.031	0.722	0.358	1.745	0.29	0.001	–99.0	–99.0
63	23.6059902	30.4649241	–99.0	–99.0	–99.0	–99.0	–99.0	–99.0	0.155	1.481	0.3	0.129	–99.0	–99.0
64	23.295885	30.4991531	–99.0	–99.0	–99.0	–99.0	5.68	0.751	15.95	0.573	23.08	0.162	–99.0	–99.0

Table 3. continued.

Num.	RA (J2000)	Dec (J2000)	3.6 μm		4.5 μm		5.8 μm		8.0 μm		24 μm		Hα	
	(°)	(°)	F_ν (mJy)	δr	F_ν (mJy)	δr	F_ν (mJy)	δr	F_ν (mJy)	δr	F_ν (mJy)	δr	F (10^{-14} erg s^{-1})	δr
65	23.4373183	30.6031596	–99.0	–99.0	–99.0	–99.0	75.28	0.166	–99.0	–99.0	163.3	0.05	–99.0	–99.0
66	23.6070908	30.4717673	0.08	0.558	0.13	0.564	0.192	0.795	0.16	0.728	0.78	0.001	–99.0	–99.0
67	23.5731509	30.4732955	0.25	0.953	0.12	0.584	0.169	0.68	0.63	0.318	1.11	0.001	–99.0	–99.0
68	23.2896084	30.4871826	0.29	1.955	0.16	1.435	1.36	0.659	1.911	0.672	3.099	0.097	0.4	0.392
69	23.3472862	30.5266611	0.74	0.692	0.51	0.801	5.48	0.346	6.445	0.784	14.31	0.407	12.63	0.447
70	23.3742461	30.530412	18.63	0.799	8.55	2.92	98.58	0.532	–99.0	–99.0	300.19	1.624	146.03	1.68
71	23.4139809	30.49824	0.27	2.12	0.09	1.431	1.32	1.484	10.17	1.014	3.82	0.186	–99.0	–99.0
72	23.4523366	30.6610505	175.3	1.792	102.97	2.683	148.28	1.079	–99.0	–99.0	281.52	0.302	–99.0	–99.0
73	23.266931	30.4825374	0.16	2.151	–99.0	–99.0	–99.0	–99.0	0.21	0.265	1.1	0.001	3.16	0.933
74	23.301739	30.5073557	–99.0	–99.0	–99.0	–99.0	–99.0	–99.0	–99.0	–99.0	31.08	1.263	–99.0	–99.0
75	23.4985862	30.5639235	–99.0	–99.0	–99.0	–99.0	–99.0	–99.0	–99.0	–99.0	40.67	0.82	104.46	2.004
76	23.4844389	30.4914555	1.14	1.222	0.73	1.264	1.04	1.36	7.74	1.289	5.23	0.017	–99.0	–99.0
77	23.39711	30.4975299	0.74	1.51	0.35	1.638	3.52	1.431	3.088	1.283	11.54	0.01	4.919	1.132
78	23.2681679	30.4922758	–99.0	–99.0	–99.0	–99.0	0.36	1.76	1.158	1.377	1.35	0.135	3.22	2.78
79	23.492846	30.5371378	–99.0	–99.0	–99.0	–99.0	14.97	0.719	115.19	0.405	28.05	0.367	10.484	2.145
80	23.2518713	30.512725	–99.0	–99.0	0.72	2.157	8.12	2.538	39.52	2.702	11.698	0.573	45.469	0.349
81	23.2813558	30.5168685	0.51	0.574	0.4	0.829	2.95	0.65	3.481	1.023	30.03	0.58	7.385	0.281
82	23.457549	30.4914213	2.25	1.105	1.7	1.165	1.5	1.155	4.58	0.942	1.42	0.098	5.62	1.089
83	23.4086361	30.504008	0.095	1.45	0.063	1.468	0.95	2.886	3.161	2.91	0.77	2.76	22.763	2.52
84	23.4698216	30.6532793	121.02	2.091	94.48	1.707	–99.0	–99.0	–99.0	–99.0	333.39	2.151	–99.0	–99.0
85	23.5536876	30.4938742	1.26	0.149	2.4	0.309	3.11	0.516	3.56	0.454	3.07	0.0	0.157	2.899
86	23.2613307	30.4928575	–99.0	–99.0	–99.0	–99.0	1.489	2.836	0.801	1.873	1.05	0.002	3.673	0.509
87	23.3278802	30.4928602	0.22	0.409	0.19	0.431	0.17	0.489	3.897	1.014	0.93	0.003	–99.0	–99.0
88	23.4088097	30.5005227	–99.0	–99.0	0.068	1.46	0.46	0.79	1.182	0.669	1.98	0.077	–99.0	–99.0
89	23.5064687	30.5122019	0.38	2.851	0.13	2.681	2.5	1.2	12.1	1.156	4.96	0.001	–99.0	–99.0
90	23.4154371	30.5039219	–99.0	–99.0	–99.0	–99.0	2.54	0.344	10.51	0.348	4.139	0.094	–99.0	–99.0
91	23.412667	30.5434291	0.252	0.653	0.219	0.585	29.66	0.305	74.77	1.577	61.36	0.496	65.3	1.3
92	23.3163221	30.500713	–99.0	–99.0	0.05	0.34	0.167	0.299	0.239	0.253	0.98	0.005	–99.0	–99.0
93	23.254073	30.5177006	0.88	0.747	0.61	0.305	4.86	0.919	16.64	1.419	9.227	0.043	53.9	2.256
94	23.2214737	30.4996198	–99.0	–99.0	–99.0	–99.0	0.276	1.945	0.265	1.559	0.46	0.001	5.129	1.937
95	23.508331	30.5014567	0.53	0.348	0.4	0.381	0.24	0.298	0.46	0.462	0.4	0.001	–99.0	–99.0
96	23.4122382	30.5205292	2.44	2.35	3.29	1.503	4.88	1.485	6.35	1.43	11.57	1.584	–99.0	–99.0
97	23.4749445	30.5517846	0.87	2.7	1.35	2.681	59.46	2.646	3.382	2.869	133.93	0.636	205.1	0.617
98	23.3537245	30.5146282	0.23	2.49	0.04	1.815	0.67	2.743	2.544	2.807	3.18	0.0	13.02	2.318
99	23.6647902	30.520899	0.35	1.869	0.16	1.439	2.59	1.599	9.37	1.683	21.35	0.011	1.09	0.833
100	23.4355158	30.5343999	5.25	2.317	1.65	2.619	8.89	1.388	40.76	2.247	14.65	0.014	2.438	1.65
101	23.5920186	30.5218368	–99.0	–99.0	–99.0	–99.0	1.79	1.288	6.79	1.17	8.89	0.001	–99.0	–99.0
102	23.4374512	30.518462	0.09	1.256	0.055	1.134	1.43	1.304	9.1	0.749	1.67	0.002	–99.0	–99.0
103	23.2701529	30.5158071	–99.0	–99.0	–99.0	–99.0	0.82	0.248	4.756	0.433	0.98	0.001	0.741	1.822
104	23.5721108	30.5620107	7.97	0.588	3.8	0.7	41.31	1.269	129.61	0.502	101.8	0.592	122.04	1.412
105	23.471327	30.5157448	0.32	2.923	–99.0	–99.0	0.59	0.764	0.819	0.474	1.04	0.001	0.303	2.72
106	23.4040552	30.5173943	0.43	0.348	0.96	0.49	1.73	0.681	1.743	0.632	1.98	0.001	–99.0	–99.0
107	23.2774335	30.5245107	0.27	0.952	0.12	0.606	0.84	0.494	2.131	0.537	2.41	0.059	2.571	1.092
108	23.3318144	30.5180844	0.204	0.275	0.32	0.115	0.33	0.268	0.46	0.754	0.72	0.002	–99.0	–99.0
109	23.5415395	30.5323582	1.29	0.773	0.63	0.671	2.65	1.491	15.73	0.612	8.95	0.014	15.72	0.604
110	23.2452382	30.5289389	–99.0	–99.0	–99.0	–99.0	1.44	2.648	9.04	1.004	2.88	0.003	–99.0	–99.0
111	23.4849398	30.521593	–99.0	–99.0	–99.0	–99.0	0.2	1.368	0.366	0.773	1.14	0.003	–99.0	–99.0
112	23.2703065	30.5205838	–99.0	–99.0	–99.0	–99.0	0.235	0.397	0.823	0.566	0.718	0.021	2.797	2.522
113	23.4444628	30.5437413	3.99	0.655	1.15	1.562	4.189	1.038	18.641	0.687	58.94	0.284	–99.0	–99.0
114	23.4990498	30.5459143	1.47	2.417	0.95	2.362	–99.0	–99.0	28.15	2.314	24.02	1.083	40.02	0.359
115	23.5569419	30.5620427	12.5	2.242	9.31	2.27	8.269	1.338	169.48	2.44	233.02	0.596	65.698	0.847
116	23.4184798	30.5264105	–99.0	–99.0	–99.0	–99.0	1.19	1.196	1.853	0.427	1.51	0.062	–99.0	–99.0
117	23.4358347	30.522334	0.176	0.92	0.174	1.434	0.726	0.214	1.997	0.365	0.842	0.125	–99.0	–99.0
118	23.5937772	30.5448368	–99.0	–99.0	–99.0	–99.0	–99.0	–99.0	–99.0	–99.0	15.66	0.015	3.548	2.293
119	23.5093193	30.52338	0.91	2.403	0.42	2.069	0.5	1.348	1.61	0.426	0.51	0.088	6.01	1.091
120	23.2567542	30.5312275	0.08	1.006	0.06	1.07	0.56	1.086	1.95	1.389	4.33	0.022	3.35	2.21
121	23.3110259	30.5437026	0.52	2.261	–99.0	–99.0	1.59	1.832	3.432	1.224	12.36	0.037	–99.0	–99.0
122	23.5068489	30.5970729	–99.0	–99.0	–99.0	–99.0	10.42	1.884	6.396	1.662	26.69	0.191	11.229	0.393
123	23.2406684	30.533238	0.22	1.363	–99.0	–99.0	–99.0	–99.0	–99.0	–99.0	2.44	0.003	–99.0	–99.0
124	23.4307023	30.5298609	0.523	2.306	0.36	2.593	0.88	1.034	2.48	0.53	2.02	0.014	1.364	0.741
125	23.2699196	30.5323766	0.26	0.612	0.1	0.5	1.36	1.135	3.942	0.646	2.99	0.032	6.592	0.363
126	23.2724933	30.5273496	1.833	0.442	1.516	0.443	1.43	0.386	1.059	0.518	0.38	0.001	–99.0	–99.0
127	23.4488423	30.551252	5.29	1.189	3.36	1.408	7.312	0.333	17.945	0.126	81.43	0.001	35.135	0.844
128	23.2576171	30.5424959	0.35	2.146	0.23	0.985	5.13	0.685	4.473	0.338	5.36	0.134	–99.0	–99.0
129	23.5013484	30.5725881	4.3	2.432	2.81	2.333	27.58	1.469	–99.0	–99.0	3.08	2.746	81.834	0.589
130	23.6751983	30.5403655	0.1	0.355	–99.0	–99.0	0.45	0.443	2.91	0.375	1.155	0.049	2.22	2.378

Table 3. continued.

Num.	RA (J2000)	Dec (J2000)	3.6 μm		4.5 μm		5.8 μm		8.0 μm		24 μm		Hα	
	(°)	(°)	F_ν (mJy)	δr	F_ν (mJy)	δr	F_ν (mJy)	δr	F_ν (mJy)	δr	F_ν (mJy)	δr	F (10^{-14} erg s^{-1})	δr
131	23.4592086	30.5634396	1.53	0.83	1.11	1.136	2.234	0.508	15.067	0.757	6.838	0.551	28.327	0.405
132	23.2326878	30.5413206	0.4	1.803	0.441	0.358	0.527	0.443	1.292	0.664	5.415	0.616	17.741	0.603
133	23.3254282	30.5561522	–99.0	–99.0	–99.0	–99.0	–99.0	–99.0	–99.0	–99.0	17.98	0.014	–99.0	–99.0
134	23.5330369	30.5465901	0.126	0.692	0.17	0.681	0.968	0.392	2.56	0.684	10.8	0.101	1.53	1.739
135	23.2550544	30.5461019	–99.0	–99.0	–99.0	–99.0	–99.0	–99.0	–99.0	–99.0	1.779	0.107	0.415	1.278
136	23.5951658	30.5693594	0.33	0.546	0.47	0.766	2.21	0.735	3.833	0.513	43.9	1.253	2.26	0.655
137	23.4600168	30.5420632	4.37	2.58	3.46	2.355	4.68	2.141	2.214	2.13	3.91	0.026	4.857	0.455
138	23.3221538	30.5362579	1.32	0.449	0.934	0.466	0.77	0.439	0.75	0.523	0.41	0.0	–99.0	–99.0
139	23.58378	30.5509049	–99.0	–99.0	–99.0	–99.0	–99.0	–99.0	13.8	0.907	6.49	0.033	–99.0	–99.0
140	23.6781752	30.5426413	0.116	1.248	0.173	1.347	0.369	0.767	0.868	0.823	1.241	0.123	–99.0	–99.0
141	23.2514388	30.5408204	0.21	1.598	–99.0	–99.0	1.79	0.267	10.33	0.771	1.37	0.001	–99.0	–99.0
142	23.2380036	30.5408871	–99.0	–99.0	–99.0	–99.0	–99.0	–99.0	0.467	1.858	0.76	0.001	–99.0	–99.0
143	23.3351058	30.5480067	0.16	1.257	0.06	1.493	3.59	1.726	3.51	1.283	4.55	0.001	9.62	1.985
144	23.4131379	30.6354521	0.245	1.131	0.57	1.02	1.519	1.131	3.996	1.327	33.199	1.682	71.21	1.508
145	23.2365346	30.5483727	0.51	1.229	0.49	1.106	1.13	1.16	–99.0	–99.0	2.56	0.028	8.238	0.801
146	23.3896177	30.5597423	–99.0	–99.0	–99.0	–99.0	3.13	2.283	2.16	0.405	3.71	0.001	94.63	1.289
147	23.6815822	30.5475032	0.019	0.262	0.014	0.666	0.112	0.448	0.28	0.381	2.22	0.001	–99.0	–99.0
148	23.660053	30.5477418	–99.0	–99.0	0.022	0.855	0.146	0.78	0.24	0.765	0.71	0.0	1.08	0.282
149	23.5934988	30.5555251	0.35	2.284	0.19	2.347	–99.0	–99.0	1.38	2.444	5.08	0.001	10.614	0.836
150	23.5349968	30.5499343	–99.0	–99.0	0.075	0.888	0.388	1.102	1.327	1.09	1.883	0.863	–99.0	–99.0
151	23.7138106	30.5466412	–99.0	–99.0	–99.0	–99.0	0.11	0.609	0.69	0.723	0.3	0.001	0.563	1.32
152	23.3790765	30.55941	–99.0	–99.0	0.15	1.976	1.86	2.021	10.23	1.952	9.73	0.014	19.34	1.787
153	23.6028416	30.5518649	0.18	0.737	0.12	0.801	0.111	0.7	0.173	0.495	2.72	0.002	0.701	0.4
154	23.216564	30.5486997	–99.0	–99.0	–99.0	–99.0	0.207	0.634	0.26	0.966	0.21	0.191	–99.0	–99.0
155	23.2525742	30.5664134	–99.0	–99.0	–99.0	–99.0	5.27	1.867	22.98	1.005	12.75	0.618	109.91	1.795
156	23.4787314	30.5667815	–99.0	–99.0	–99.0	–99.0	–99.0	–99.0	–99.0	–99.0	7.9	1.938	–99.0	–99.0
157	23.2583902	30.5803033	1.79	1.774	0.35	1.622	3.36	2.692	41.51	1.56	24.69	0.453	32.504	0.664
158	23.3874995	30.5626085	0.958	2.659	1.213	2.681	1.234	2.615	1.087	2.398	3.595	0.406	11.577	1.594
159	23.3038175	30.5704297	0.52	0.946	0.51	0.783	1.07	0.826	1.908	0.629	7.58	0.128	–99.0	–99.0
160	23.2514615	30.5531872	0.16	0.757	0.22	0.701	0.26	0.707	0.39	0.695	0.57	0.001	0.726	0.49
161	23.2925744	30.554711	1.6	1.969	1.04	1.991	0.63	2.41	0.88	2.073	0.38	0.124	–99.0	–99.0
162	23.6074399	30.555159	0.05	0.752	0.1	0.451	0.219	0.591	0.31	0.351	0.38	0.001	–99.0	–99.0
163	23.2525361	30.5729212	1.26	2.459	–99.0	–99.0	1.039	1.077	2.977	1.039	13.33	0.429	13.304	1.826
164	23.7041713	30.5580431	0.19	0.532	0.23	0.416	0.22	0.385	0.29	0.622	0.55	0.0	–99.0	–99.0
165	23.4966018	30.5968722	9.53	1.065	6.8	1.018	24.41	1.07	24.015	0.747	89.879	0.041	59.847	0.813
166	23.4772433	30.5775154	–99.0	–99.0	–99.0	–99.0	–99.0	–99.0	–99.0	–99.0	12.26	0.011	7.657	1.866
167	23.6714293	30.5595353	0.014	0.541	0.015	0.573	0.144	0.799	0.32	0.922	0.47	0.001	0.075	0.599
168	23.3970484	30.6078945	7.15	0.111	4.01	0.35	6.802	0.84	19.633	0.828	17.062	1.374	60.9	1.895
169	23.3008364	30.5746583	0.15	0.97	0.067	1.242	1.284	1.296	3.218	1.223	4.63	0.352	–99.0	–99.0
170	23.6638671	30.5627627	0.15	0.638	0.15	0.618	–99.0	–99.0	0.86	0.513	0.34	0.001	–99.0	–99.0
171	23.6552803	30.5817449	0.68	0.929	0.55	0.829	2.86	1.088	11.94	1.018	59.38	0.003	18.96	1.197
172	23.425105	30.5730196	–99.0	–99.0	–99.0	–99.0	0.701	0.502	3.624	0.288	15.285	0.454	–99.0	–99.0
173	23.5763911	30.5756712	–99.0	–99.0	–99.0	–99.0	–99.0	–99.0	0.254	1.221	2.22	0.001	23.882	1.264
174	23.5456241	30.6048973	4.74	0.758	3.65	0.518	28.73	0.574	13.459	1.784	105.67	0.189	33.12	0.764
175	23.2466984	30.5796258	0.84	1.197	0.73	1.046	1.23	0.305	8.37	1.342	5.24	0.49	13.045	2.382
176	23.4222639	30.5715262	0.21	2.946	–99.0	–99.0	0.77	0.317	2.86	0.775	0.8	0.292	0.8	0.396
177	23.4678741	30.5759677	–99.0	–99.0	–99.0	–99.0	0.62	2.329	2.425	1.738	58.26	0.721	–99.0	–99.0
178	23.2181368	30.584627	0.24	1.853	0.14	2.035	1.85	0.451	6.66	0.973	8.74	0.56	46.81	2.917
179	23.3957336	30.5732324	0.062	2.789	0.053	0.667	0.2	0.592	0.557	0.413	0.91	0.061	–99.0	–99.0
180	23.3483409	30.5743059	0.28	0.881	0.31	0.659	0.188	0.463	0.67	0.402	1.66	0.038	–99.0	–99.0
181	23.2877777	30.5827724	0.19	2.588	0.13	2.173	0.82	2.023	4.12	2.096	3.74	1.764	–99.0	–99.0
182	23.3859728	30.6155237	0.81	1.825	1.64	1.776	10.11	1.326	4.592	0.667	35.84	0.064	9.0	0.433
183	23.2423017	30.5802227	–99.0	–99.0	–99.0	–99.0	0.215	1.322	0.704	1.471	11.369	1.11	–99.0	–99.0
184	23.3909423	30.6915587	24.63	2.767	23.3	2.096	–99.0	–99.0	–99.0	–99.0	1434.67	0.929	–99.0	–99.0
185	23.4390916	30.6136023	4.74	0.545	3.22	1.017	23.3	0.646	30.405	0.622	136.49	0.047	24.692	0.546
186	23.274171	30.5832355	0.019	2.686	–99.0	–99.0	0.92	2.668	1.651	2.699	1.76	0.022	–99.0	–99.0
187	23.5647071	30.6200833	2.92	0.863	2.67	1.006	7.34	2.571	4.592	2.638	216.15	0.426	63.908	0.404
188	23.6333844	30.5817639	0.19	0.374	0.22	0.308	0.24	0.553	0.48	0.295	1.16	0.052	–99.0	–99.0
189	23.3151417	30.5847772	0.55	1.589	0.52	1.067	1.41	0.813	1.948	1.513	2.4	0.264	0.101	1.19
190	23.2808383	30.587491	–99.0	–99.0	–99.0	–99.0	1.65	2.953	3.556	2.474	2.97	0.022	1.965	1.134
191	23.404885	30.5862258	–99.0	–99.0	0.31	1.08	1.62	0.437	8.176	0.316	1.48	0.002	4.148	1.275
192	23.4580465	30.5838051	0.16	0.334	0.06	0.46	1.558	1.445	1.5	2.902	0.75	0.002	–99.0	–99.0
193	23.3949208	30.6182892	3.89	1.172	3.49	0.829	20.17	1.772	18.729	0.788	56.527	0.121	61.5	0.969
194	23.5957164	30.5871002	0.24	2.87	0.05	2.883	0.26	0.848	1.83	0.463	1.03	0.259	2.13	1.331
195	23.5453392	30.5978751	0.43	0.448	1.0	0.662	5.14	0.529	5.926	0.465	19.58	0.093	11.23	2.186
196	23.5929936	30.5886504	–99.0	–99.0	–99.0	–99.0	–99.0	–99.0	–99.0	–99.0	1.721	0.074	–99.0	–99.0

Table 3. continued.

Num.	RA (J2000)	Dec (J2000)	3.6 μm		4.5 μm		5.8 μm		8.0 μm		24 μm		Hα	
	(°)	(°)	F_ν (mJy)	δr	F_ν (mJy)	δr	F_ν (mJy)	δr	F_ν (mJy)	δr	F_ν (mJy)	δr	F (10^{-14} erg s^{-1})	δr
197	23.2319069	30.5933869	0.24	0.252	0.09	0.096	0.35	0.738	1.48	1.431	5.63	0.016	4.73	2.611
198	23.50982	30.6456077	64.19	1.915	–99.0	–99.0	–99.0	–99.0	239.2	2.931	258.82	2.863	67.405	0.8
199	23.4978759	30.599838	0.67	0.361	0.686	0.388	5.627	0.23	16.026	0.234	39.301	0.292	–99.0	–99.0
200	23.6299726	30.5893845	0.011	0.371	0.01	0.571	0.333	0.947	1.08	1.048	0.72	0.0	–99.0	–99.0
201	23.4588671	30.6248737	2.93	0.973	2.29	1.09	16.63	1.449	28.476	0.821	100.66	1.428	39.91	2.579
202	23.2861385	30.5906052	0.98	0.598	1.23	0.714	1.47	0.577	2.03	0.596	1.25	0.003	–99.0	–99.0
203	23.4793863	30.5914266	–99.0	–99.0	–99.0	–99.0	0.38	1.047	1.166	0.876	0.71	0.003	–99.0	–99.0
204	23.4017975	30.5921185	4.78	0.902	2.74	0.916	2.0	0.931	1.66	0.729	0.47	0.001	–99.0	–99.0
205	23.3237072	30.5951935	0.2	1.553	0.09	1.175	0.57	0.185	4.1	0.362	0.23	0.171	0.36	1.812
206	23.4515238	30.5964118	–99.0	–99.0	–99.0	–99.0	–99.0	–99.0	–99.0	–99.0	0.58	0.006	–99.0	–99.0
207	23.2377615	30.5997876	–99.0	–99.0	–99.0	–99.0	0.372	0.365	1.92	0.707	1.04	0.001	12.01	2.376
208	23.3562276	30.5978429	0.77	0.492	1.28	0.508	1.54	0.463	1.84	0.41	1.35	0.0	–99.0	–99.0
209	23.4639265	30.5974045	0.17	1.778	0.176	1.791	0.29	0.494	1.8	0.309	0.46	0.002	1.67	0.151
210	23.4319437	30.6509415	–99.0	–99.0	–99.0	–99.0	–99.0	–99.0	–99.0	–99.0	187.31	1.931	197.57	2.463
211	23.2292997	30.5976103	–99.0	–99.0	–99.0	–99.0	–99.0	–99.0	–99.0	–99.0	0.606	0.176	5.143	0.751
212	23.2416602	30.6017643	1.186	1.504	0.663	1.527	0.759	1.507	1.259	1.48	1.088	0.089	–99.0	–99.0
213	23.4722505	30.6015189	–99.0	–99.0	–99.0	–99.0	0.22	1.041	25.631	0.368	0.92	0.081	–99.0	–99.0
214	23.2332881	30.5998748	0.378	1.271	0.418	1.391	0.381	1.613	0.52	0.71	0.434	0.114	–99.0	–99.0
215	23.4775595	30.6015451	0.05	2.912	0.093	2.704	0.468	2.795	–99.0	–99.0	1.091	0.038	–99.0	–99.0
216	23.4666875	30.611183	–99.0	–99.0	–99.0	–99.0	–99.0	–99.0	–99.0	–99.0	4.09	0.004	6.49	0.743
217	23.3404764	30.6065863	0.85	0.669	0.99	0.742	1.52	0.525	2.85	0.63	3.99	0.015	–99.0	–99.0
218	23.2833369	30.6042448	–99.0	–99.0	–99.0	–99.0	0.066	0.28	0.509	2.497	0.21	0.002	–99.0	–99.0
219	23.5263608	30.6283346	–99.0	–99.0	–99.0	–99.0	7.22	1.61	–99.0	–99.0	12.92	0.827	–99.0	–99.0
220	23.6274042	30.6098987	0.33	1.747	0.192	0.525	0.47	0.639	1.49	0.785	2.16	0.001	0.252	0.225
221	23.3639789	30.6081481	0.17	1.616	0.105	2.48	0.3	0.595	2.415	0.544	0.75	0.002	0.047	2.58
222	23.5300461	30.60892	0.43	1.354	0.12	2.643	1.849	0.813	2.59	1.838	0.99	0.003	7.11	1.103
223	23.4475332	30.6187409	–99.0	–99.0	–99.0	–99.0	3.11	0.555	3.388	2.834	5.22	0.003	0.967	1.79
224	23.3134189	30.6111006	0.16	2.218	–99.0	–99.0	0.78	0.779	12.37	1.73	1.15	0.0	0.161	0.419
225	23.3702028	30.6733838	4.117	0.621	4.589	0.608	36.54	1.197	65.556	0.527	633.39	0.017	158.22	2.251
226	23.50066	30.6797439	4.39	0.682	5.146	0.663	26.189	0.641	76.676	0.479	1000.35	0.274	18.689	0.531
227	23.498594	30.6198509	1.11	2.732	–99.0	–99.0	7.61	2.254	–99.0	–99.0	7.28	0.004	–99.0	–99.0
228	23.2437321	30.6103843	0.09	0.502	0.03	0.437	0.54	0.516	3.48	0.623	0.97	0.001	1.09	0.93
229	23.5626519	30.6269113	1.17	0.742	2.05	0.488	10.17	0.908	7.407	0.734	21.243	0.038	–99.0	–99.0
230	23.5074748	30.6226856	–99.0	–99.0	0.23	2.296	3.17	2.106	–99.0	–99.0	6.56	0.001	9.177	1.012
231	23.306399	30.6582237	0.84	0.928	0.66	1.451	8.71	1.534	7.003	1.096	34.39	0.035	3.433	0.507
232	23.3802176	30.6340207	0.45	1.462	0.27	1.313	11.15	0.514	2.329	0.944	27.57	0.007	22.82	1.972
233	23.2292626	30.61458	0.52	1.111	0.34	0.844	0.26	0.847	1.26	1.02	0.74	0.002	3.815	2.972
234	23.3977557	30.6581247	4.06	0.501	3.11	0.338	9.788	0.678	27.048	0.422	194.41	0.081	18.056	0.777
235	23.5122553	30.6286521	0.91	2.567	0.7	1.64	4.26	0.763	7.66	1.218	5.76	0.002	11.722	2.571
236	23.2987395	30.6491089	1.69	0.713	1.208	1.39	9.21	1.068	31.79	1.332	27.994	0.161	41.971	0.319
237	23.7037368	30.6246831	–99.0	–99.0	–99.0	–99.0	0.18	2.776	0.86	2.633	3.19	0.379	0.43	1.646
238	23.1891098	30.648771	–99.0	–99.0	–99.0	–99.0	–99.0	–99.0	–99.0	–99.0	61.68	1.53	368.95	1.037
239	23.4483822	30.6444345	0.669	2.756	0.606	2.751	6.135	2.951	16.634	2.544	82.36	0.453	124.33	0.148
240	23.5373803	30.6525042	–99.0	–99.0	1.23	0.464	8.07	0.492	24.91	1.143	81.69	0.036	–99.0	–99.0
241	23.2781665	30.6289551	0.06	1.39	0.055	1.33	0.33	1.478	2.07	1.113	4.33	0.023	–99.0	–99.0
242	23.5853333	30.6329828	0.18	1.909	0.035	1.001	–99.0	–99.0	14.94	0.506	4.89	0.001	20.11	1.336
243	23.5361604	30.6274222	–99.0	–99.0	–99.0	–99.0	–99.0	–99.0	6.712	1.728	1.38	0.003	–99.0	–99.0
244	23.6966122	30.6321576	0.3	0.355	0.17	0.446	1.23	0.477	5.31	0.658	5.09	0.069	4.57	0.366
245	23.2178479	30.6211361	0.08	1.645	–99.0	–99.0	0.206	0.851	0.66	0.661	0.18	0.001	1.34	0.353
246	23.5156327	30.6313122	1.251	0.883	1.145	0.816	0.907	0.814	0.818	0.821	1.562	0.084	–99.0	–99.0
247	23.5022229	30.6357354	–99.0	–99.0	–99.0	–99.0	9.34	1.734	31.27	1.492	8.899	0.061	17.95	0.153
248	23.4862749	30.6250972	0.57	1.484	0.46	1.412	1.277	1.475	4.051	2.724	1.304	0.441	–99.0	–99.0
249	23.3670659	30.6257606	0.15	2.989	0.1	2.719	–99.0	–99.0	–99.0	–99.0	0.39	0.003	0.055	1.631
250	23.5408285	30.6375233	1.01	0.862	1.5	0.802	3.05	0.799	8.87	0.26	11.76	0.01	0.2	0.412
251	23.3032423	30.6451688	3.86	2.367	3.09	2.304	2.518	1.353	17.14	2.974	35.19	0.261	14.732	0.688
252	23.3588787	30.6304911	–99.0	–99.0	–99.0	–99.0	5.559	1.418	1.611	2.255	0.74	0.073	–99.0	–99.0
253	23.3605019	30.6506041	2.03	2.931	–99.0	–99.0	–99.0	–99.0	0.727	1.155	17.68	0.564	6.937	1.766
254	23.3648166	30.6287867	–99.0	–99.0	–99.0	–99.0	1.039	0.337	2.472	0.719	1.276	0.147	–99.0	–99.0
255	23.6939075	30.637165	0.31	0.577	0.12	0.684	1.28	0.681	2.748	0.072	2.226	0.126	4.922	0.723
256	23.455278	30.6333584	–99.0	–99.0	0.32	0.549	1.45	1.161	4.75	0.753	4.55	0.019	–99.0	–99.0
257	23.3618237	30.6449707	1.34	1.011	0.64	0.771	2.126	0.487	6.18	0.2	17.28	0.38	13.11	1.429
258	23.5539412	30.6350589	0.45	0.841	0.83	0.636	1.2	0.544	1.09	0.546	1.39	0.046	–99.0	–99.0
259	23.5738589	30.634089	0.5	1.565	0.22	1.541	–99.0	–99.0	–99.0	–99.0	0.59	0.003	–99.0	–99.0
260	23.2934401	30.6466653	0.46	0.329	0.73	0.235	0.87	0.306	2.45	0.463	11.18	0.055	–99.0	–99.0
261	23.5768249	30.6354645	1.881	1.239	1.08	1.183	0.947	1.147	0.983	1.166	0.487	0.255	–99.0	–99.0
262	23.3230689	30.6363488	0.28	0.687	0.23	0.625	0.206	0.759	0.94	0.715	1.31	0.001	–99.0	–99.0

Table 3. continued.

Num.	RA (J2000)	Dec (J2000)	3.6 μm		4.5 μm		5.8 μm		8.0 μm		24 μm		Hα	
	(°)	(°)	F_ν (mJy)	δr	F_ν (mJy)	δr	F_ν (mJy)	δr	F_ν (mJy)	δr	F_ν (mJy)	δr	F (10^{-14} erg s^{-1})	δr
263	23.2229493	30.6375472	0.289	0.495	0.346	0.568	0.423	0.645	–99.0	–99.0	2.639	1.203	–99.0	–99.0
264	23.2215632	30.6358148	0.23	0.291	0.27	0.267	–99.0	–99.0	0.4	0.262	0.79	0.181	–99.0	–99.0
265	23.6530394	30.6374993	–99.0	–99.0	–99.0	–99.0	0.112	2.684	–99.0	–99.0	1.0	0.071	1.01	2.789
266	23.5325477	30.653787	0.343	0.392	0.339	0.217	2.436	0.274	6.768	0.151	14.889	0.147	–99.0	–99.0
267	23.4320263	30.6833536	55.4	2.729	3.25	2.228	41.51	1.861	7.808	1.384	46.14	0.145	13.007	1.355
268	23.3737535	30.6429053	–99.0	–99.0	0.033	1.193	0.44	1.176	5.924	0.886	0.95	0.063	–99.0	–99.0
269	23.4835742	30.6530796	–99.0	–99.0	–99.0	–99.0	–99.0	–99.0	1.722	2.778	4.2	0.011	–99.0	–99.0
270	23.3420438	30.6461182	0.41	0.257	0.82	0.826	1.69	0.984	3.53	0.985	1.91	0.003	–99.0	–99.0
271	23.5435613	30.6544413	–99.0	–99.0	0.143	0.909	6.21	2.38	9.295	2.452	9.04	0.115	11.267	0.185
272	23.3503725	30.6532	–99.0	–99.0	–99.0	–99.0	–99.0	–99.0	2.279	2.06	0.46	1.056	–99.0	–99.0
273	23.407445	30.6596327	0.274	0.567	0.23	0.562	2.401	0.863	6.703	0.499	6.978	0.039	3.566	0.279
274	23.3403854	30.6495644	0.673	0.431	0.556	0.36	0.708	0.383	2.172	0.565	2.416	0.204	–99.0	–99.0
275	23.4880319	30.6493804	–99.0	–99.0	–99.0	–99.0	1.51	0.433	4.166	1.053	0.99	0.121	–99.0	–99.0
276	23.4900755	30.7053428	1.925	0.568	3.88	1.248	25.06	1.298	37.937	0.372	95.97	0.085	90.55	1.81
277	23.6492502	30.6738673	0.39	1.872	–99.0	–99.0	4.22	0.621	3.133	1.089	15.21	1.223	0.361	0.694
278	23.2647003	30.6511552	0.27	0.52	0.37	0.57	0.54	0.617	0.81	0.746	1.91	0.035	–99.0	–99.0
279	23.3465799	30.6508679	–99.0	–99.0	–99.0	–99.0	1.19	0.556	3.961	0.768	1.1	0.191	–99.0	–99.0
280	23.4057678	30.6574906	0.61	2.36	0.3	1.523	1.63	0.848	–99.0	–99.0	10.303	0.973	–99.0	–99.0
281	23.6559155	30.670175	–99.0	–99.0	0.024	0.665	0.075	1.281	–99.0	–99.0	1.94	0.362	0.084	0.677
282	23.3305157	30.6582338	–99.0	–99.0	–99.0	–99.0	–99.0	–99.0	9.32	1.776	2.16	0.049	6.594	2.247
283	23.4265111	30.6685087	–99.0	–99.0	–99.0	–99.0	4.62	2.732	–99.0	–99.0	6.24	0.001	–99.0	–99.0
284	23.2787484	30.6528663	0.2	0.405	0.13	0.251	0.232	0.62	0.235	0.639	0.88	0.001	–99.0	–99.0
285	23.4972031	30.6574364	0.131	2.03	0.108	1.824	1.02	0.872	6.824	0.445	0.95	0.003	–99.0	–99.0
286	23.422845	30.6964213	0.622	2.564	2.4	0.952	–99.0	–99.0	–99.0	–99.0	104.03	1.32	155.37	1.731
287	23.5542603	30.7003956	0.56	2.609	0.37	2.637	–99.0	–99.0	99.52	2.491	36.19	0.252	5.406	2.558
288	23.5534039	30.6712449	0.5	2.402	0.6	2.409	–99.0	–99.0	–99.0	–99.0	5.65	0.014	8.56	1.102
289	23.6025439	30.6626101	0.39	2.229	0.1	2.093	0.59	1.855	–99.0	–99.0	2.98	0.039	–99.0	–99.0
290	23.2648052	30.6650077	0.1	2.258	0.08	1.927	1.71	1.624	5.44	0.763	4.33	0.021	7.953	2.37
291	23.2309423	30.6592021	0.22	1.376	0.05	1.053	0.23	0.728	1.88	1.509	1.08	0.001	3.93	0.897
292	23.4857212	30.6837624	1.737	0.977	0.991	0.564	12.07	0.049	13.102	0.571	8.785	0.274	12.81	0.048
293	23.6956205	30.6601853	–99.0	–99.0	–99.0	–99.0	–99.0	–99.0	0.056	1.867	0.772	0.03	–99.0	–99.0
294	23.1957872	30.66283	0.06	1.57	0.111	0.932	0.179	0.517	0.35	0.569	1.82	0.037	–99.0	–99.0
295	23.4160083	30.6686131	–99.0	–99.0	–99.0	–99.0	1.03	2.184	–99.0	–99.0	3.21	0.003	1.44	1.868
296	23.2580642	30.6641098	1.31	2.836	–99.0	–99.0	1.45	1.125	4.43	1.691	2.76	0.254	0.4	2.236
297	23.4612661	30.6889857	15.6	1.695	–99.0	–99.0	4.373	0.343	13.748	0.481	21.454	0.342	–99.0	–99.0
298	23.5288203	30.6961545	1.91	2.232	1.41	1.704	27.88	2.015	–99.0	–99.0	79.67	1.85	152.0	2.093
299	23.3258953	30.6893883	0.42	1.429	0.15	0.614	0.997	0.477	3.215	0.65	13.92	0.022	9.43	1.883
300	23.4075672	30.6798624	–99.0	–99.0	–99.0	–99.0	2.49	1.851	66.526	0.536	4.41	0.001	–99.0	–99.0
301	23.6259803	30.6768091	1.99	2.837	1.26	2.575	1.49	2.158	2.84	1.416	4.09	0.025	22.33	1.521
302	23.3743258	30.6801545	0.558	0.672	0.71	1.07	2.977	0.95	7.792	0.67	26.316	0.026	24.407	0.903
303	23.3199767	30.6738485	0.1	1.637	0.09	0.834	0.23	0.495	0.823	0.726	1.49	0.053	–99.0	–99.0
304	23.6790852	30.6756613	0.13	1.23	0.08	0.907	0.48	0.602	1.98	0.434	1.75	0.239	–99.0	–99.0
305	23.4159351	30.6854883	1.33	1.163	0.96	1.228	4.08	0.893	10.516	0.558	16.973	0.11	24.33	1.116
306	23.6778627	30.6804357	–99.0	–99.0	0.021	0.541	0.225	0.505	0.574	0.518	2.417	0.036	–99.0	–99.0
307	23.3278438	30.6767446	0.06	2.453	0.121	2.202	1.41	0.853	3.408	0.829	1.26	0.0	–99.0	–99.0
308	23.1794239	30.676677	0.05	0.695	0.096	0.396	0.15	0.613	1.73	0.853	1.01	0.129	4.74	1.418
309	23.5742394	30.6763032	–99.0	–99.0	–99.0	–99.0	–99.0	–99.0	–99.0	–99.0	0.67	0.004	0.03	2.943
310	23.1765675	30.6772942	–99.0	–99.0	–99.0	–99.0	–99.0	–99.0	–99.0	–99.0	1.346	1.003	–99.0	–99.0
311	23.3965969	30.6775016	0.13	1.057	0.38	1.017	0.63	1.198	1.17	0.749	0.77	0.066	–99.0	–99.0
312	23.6407516	30.6849669	0.37	1.025	0.27	0.963	1.65	0.948	3.21	0.972	7.06	0.029	3.23	0.946
313	23.4473536	30.688507	0.135	2.195	0.52	2.115	2.25	2.463	1.595	2.688	3.83	2.687	–99.0	–99.0
314	23.2617399	30.6859556	0.15	1.885	0.244	2.032	0.91	1.319	3.16	1.468	2.054	1.499	7.229	0.812
315	23.7281912	30.6883464	–99.0	–99.0	–99.0	–99.0	0.204	0.831	0.84	0.886	1.4	0.108	4.323	0.012
316	23.6269102	30.6896408	–99.0	–99.0	0.3	2.926	1.96	1.639	10.1	1.395	7.72	0.001	11.32	2.609
317	23.2460603	30.6929722	3.99	0.666	2.46	0.69	4.21	0.243	19.5	0.81	12.61	0.0	1.56	2.593
318	23.2774538	30.6813692	0.057	1.844	0.04	1.479	0.051	0.155	0.199	0.445	0.53	0.001	–99.0	–99.0
319	23.5451985	30.7056543	0.61	0.451	0.441	0.227	1.693	1.065	4.618	1.032	3.664	0.673	13.348	0.68
320	23.2564197	30.6849835	0.24	2.359	0.06	2.329	0.332	0.52	1.01	0.648	0.83	0.075	0.6	1.454
321	23.4181752	30.7654054	–99.0	–99.0	3.12	2.713	44.27	1.022	19.962	2.945	101.03	0.004	34.22	1.035
322	23.5696987	30.6886576	0.69	0.393	0.46	0.479	0.32	0.435	1.854	0.385	1.26	0.001	–99.0	–99.0
323	23.5191676	30.6870017	–99.0	–99.0	–99.0	–99.0	1.63	1.435	3.47	0.538	1.44	0.004	1.03	0.695
324	23.3100024	30.7547369	0.79	0.721	0.59	1.019	4.867	0.963	2.831	0.448	60.17	0.513	–99.0	–99.0
325	23.4830367	30.7221122	0.76	0.521	0.51	0.6	5.98	0.582	29.56	2.521	7.342	0.299	5.1	0.262
326	23.5563729	30.6925001	0.033	1.403	0.05	1.542	0.097	0.815	8.933	2.896	0.66	0.004	0.234	0.635
327	23.2018147	30.692144	–99.0	–99.0	0.023	0.489	0.296	0.616	0.49	0.671	0.8	0.001	0.137	0.39
328	23.191209	30.6932802	0.12	0.973	0.08	0.855	0.13	0.762	0.85	0.733	1.05	0.001	4.6	0.153

Table 3. continued.

Num.	RA (J2000)	Dec (J2000)	3.6 μm		4.5 μm		5.8 μm		8.0 μm		24 μm		Hα	
	(°)	(°)	F_ν (mJy)	δr	F_ν (mJy)	δr	F_ν (mJy)	δr	F_ν (mJy)	δr	F_ν (mJy)	δr	F (10^{-14} erg s^{-1})	δr
329	23.4626802	30.6976633	0.19	0.924	0.16	0.515	0.33	0.531	0.86	0.448	0.6	0.002	–99.0	–99.0
330	23.3636271	30.6999567	0.56	1.614	0.21	1.272	0.36	0.965	1.33	0.648	1.58	0.001	–99.0	–99.0
331	23.1789114	30.7000799	0.042	0.893	0.014	0.805	0.13	0.591	0.17	0.844	0.4	0.003	–99.0	–99.0
332	23.6862291	30.7104179	–99.0	–99.0	–99.0	–99.0	1.2	2.672	6.733	1.425	3.618	0.08	3.515	0.998
333	23.4186642	30.7178943	–99.0	–99.0	–99.0	–99.0	4.1	1.536	–99.0	–99.0	8.48	0.002	–99.0	–99.0
334	23.2837586	30.7067748	0.36	1.598	0.18	1.471	0.914	0.077	2.361	0.237	1.324	0.065	1.33	0.557
335	23.4353561	30.7437675	3.35	0.886	3.24	0.948	9.098	0.892	22.493	0.855	204.66	0.024	89.796	1.054
336	23.4823506	30.7140345	0.164	0.783	0.22	1.283	1.15	0.746	4.54	0.767	2.396	0.09	0.612	0.273
337	23.3705591	30.7047161	0.83	1.637	0.44	1.499	0.85	0.428	1.736	0.04	0.82	0.002	6.888	0.447
338	23.4410897	30.7128436	–99.0	–99.0	–99.0	–99.0	–99.0	–99.0	11.37	2.857	6.81	0.002	25.84	1.447
339	23.6892886	30.7068735	0.17	1.396	0.09	0.948	0.55	0.926	3.54	0.721	1.63	0.069	4.47	0.643
340	23.4813787	30.7577943	8.91	1.926	6.97	1.9	–99.0	–99.0	–99.0	–99.0	200.59	0.007	263.49	1.844
341	23.3779287	30.7073905	0.27	2.296	0.12	2.193	0.373	0.507	7.83	1.777	0.82	0.002	–99.0	–99.0
342	23.5046251	30.7315513	2.66	1.016	1.84	1.07	13.81	0.602	50.43	0.789	58.93	0.006	35.11	0.376
343	23.3284211	30.7127914	0.302	0.827	0.56	1.439	0.53	0.953	0.53	0.715	0.829	0.031	–99.0	–99.0
344	23.6847832	30.72261	0.18	0.335	0.031	0.496	0.444	0.251	1.82	0.158	3.46	0.006	1.75	2.513
345	23.4427305	30.7350593	1.92	2.677	1.42	0.641	6.53	1.924	20.49	1.623	21.62	0.409	–99.0	–99.0
346	23.2005507	30.7141313	0.27	0.769	0.14	0.762	0.143	0.349	0.104	0.788	0.21	0.001	–99.0	–99.0
347	23.3068917	30.7208665	0.07	0.748	0.072	0.801	0.45	0.973	2.14	1.127	2.71	0.029	0.764	0.755
348	23.2963855	30.7545119	2.96	0.201	2.964	0.404	21.28	0.789	72.63	0.832	177.96	0.11	196.41	0.792
349	23.588217	30.7268656	–99.0	–99.0	–99.0	–99.0	0.88	0.734	2.816	0.357	1.751	0.077	2.063	0.488
350	23.5853593	30.7249357	0.25	2.342	0.12	2.401	0.193	1.779	1.25	0.736	0.77	0.111	–99.0	–99.0
351	23.5722855	30.7303298	0.07	1.498	0.03	1.702	0.97	1.087	9.85	1.218	1.78	0.043	0.759	1.157
352	23.6159013	30.7278468	1.36	0.471	1.86	0.435	2.1	0.446	2.23	0.281	2.34	0.001	–99.0	–99.0
353	23.3367059	30.7268656	0.32	0.766	0.24	0.746	0.225	0.69	0.51	0.505	1.34	0.002	0.053	1.389
354	23.3398438	30.7280363	–99.0	–99.0	0.128	0.745	0.096	0.944	0.212	0.553	0.759	0.08	–99.0	–99.0
355	23.4290995	30.744778	2.63	1.304	1.95	1.101	7.748	1.563	23.673	1.903	49.43	0.048	38.495	0.366
356	23.5378834	30.7326145	0.2	0.465	0.335	0.474	0.8	0.517	1.37	0.383	2.66	0.02	–99.0	–99.0
357	23.5755386	30.7323384	–99.0	–99.0	0.034	0.303	0.897	1.137	2.695	0.639	0.562	0.081	–99.0	–99.0
358	23.712761	30.7324576	0.107	0.109	0.14	0.191	0.176	0.249	0.189	0.346	0.34	0.002	–99.0	–99.0
359	23.5783413	30.7355878	–99.0	–99.0	–99.0	–99.0	1.011	0.555	2.647	0.132	1.541	0.194	4.291	2.661
360	23.5028228	30.7421674	0.91	2.044	0.63	1.276	3.4	1.054	24.96	1.629	3.48	0.011	3.17	2.587
361	23.5066628	30.7488883	0.44	1.03	0.29	0.863	1.374	0.577	3.813	0.991	17.99	0.001	8.225	0.92
362	23.5556356	30.7450627	0.29	2.333	0.04	2.904	2.31	2.153	4.551	1.222	4.08	0.002	–99.0	–99.0
363	23.2441858	30.7422111	0.1	0.45	0.07	0.427	0.44	0.168	1.87	1.068	2.01	0.001	4.352	1.053
364	23.2183934	30.7403776	–99.0	–99.0	–99.0	–99.0	–99.0	–99.0	0.31	2.51	1.319	0.027	0.072	1.576
365	23.5405183	30.7389008	–99.0	–99.0	–99.0	–99.0	–99.0	–99.0	1.887	1.114	0.58	0.147	–99.0	–99.0
366	23.3949093	30.7454522	–99.0	–99.0	–99.0	–99.0	0.96	0.248	2.885	0.444	1.67	0.092	–99.0	–99.0
367	23.5446783	30.7487836	–99.0	–99.0	–99.0	–99.0	1.22	2.576	14.61	1.22	3.61	0.002	0.231	1.18
368	23.5526339	30.752373	–99.0	–99.0	–99.0	–99.0	1.64	1.793	9.16	0.878	2.61	0.044	7.821	0.745
369	23.5542291	30.7589305	–99.0	–99.0	–99.0	–99.0	–99.0	–99.0	4.463	2.273	9.31	0.181	–99.0	–99.0
370	23.2488596	30.7455636	–99.0	–99.0	–99.0	–99.0	0.135	0.596	0.316	1.048	0.39	0.001	–99.0	–99.0
371	23.266285	30.7481966	0.21	1.412	0.15	1.193	0.103	0.468	0.25	0.639	1.3	0.001	–99.0	–99.0
372	23.1921287	30.7461989	–99.0	–99.0	–99.0	–99.0	0.434	0.81	0.939	0.201	0.21	0.174	2.75	0.775
373	23.3634157	30.7510251	0.31	2.741	–99.0	–99.0	0.99	0.882	7.24	1.412	1.19	0.15	0.92	0.47
374	23.4470914	30.758189	–99.0	–99.0	–99.0	–99.0	5.97	2.357	33.36	2.188	6.95	0.028	–99.0	–99.0
375	23.2843986	30.7525087	0.11	1.955	0.027	0.142	0.26	0.391	0.6	0.328	0.77	0.001	0.243	0.824
376	23.2399159	30.7517994	–99.0	–99.0	–99.0	–99.0	0.045	0.542	0.113	0.434	0.34	0.001	–99.0	–99.0
377	23.2780267	30.7565926	–99.0	–99.0	–99.0	–99.0	0.561	1.311	–99.0	–99.0	0.76	0.005	–99.0	–99.0
378	23.6687258	30.7656076	–99.0	–99.0	–99.0	–99.0	–99.0	–99.0	3.8	1.629	7.49	0.001	1.53	0.47
379	23.3184471	30.7858609	0.59	1.068	0.3	1.059	3.05	0.919	2.796	1.254	9.91	1.357	4.992	0.499
380	23.2144993	30.7601547	–99.0	–99.0	–99.0	–99.0	0.033	0.888	0.077	0.542	0.54	0.001	0.442	2.745
381	23.4686411	30.7740396	0.32	1.351	0.36	0.58	2.57	1.061	21.45	1.999	7.82	0.002	5.64	2.665
382	23.280334	30.7619284	3.13	0.478	2.75	0.582	2.4	0.534	2.8	0.462	0.56	0.003	–99.0	–99.0
383	23.6238238	30.7650439	0.76	0.542	0.99	0.644	1.04	0.621	0.99	0.62	1.29	0.046	–99.0	–99.0
384	23.2076778	30.7654054	0.048	0.28	0.039	0.297	0.258	0.297	0.49	0.526	0.28	0.0	0.746	0.123
385	23.4941868	30.7732033	0.16	1.24	0.07	0.962	0.88	0.678	2.213	0.801	2.325	0.063	0.221	0.417
386	23.5321648	30.7702218	0.87	2.541	0.39	2.157	0.47	1.253	2.66	1.63	0.93	0.005	1.121	3.0
387	23.3923703	30.7910931	0.156	0.495	0.114	0.406	1.069	0.288	3.232	0.521	1.805	0.683	0.982	0.232
388	23.5520915	30.9057374	0.479	0.529	1.04	0.54	1.78	0.465	2.16	0.499	2.37	0.001	–99.0	–99.0
389	23.3708825	30.8078404	–99.0	–99.0	–99.0	–99.0	0.38	0.869	1.37	1.661	0.39	0.001	0.19	1.104
390	23.4955476	30.9254162	0.19	0.637	0.14	0.559	0.71	0.645	2.32	0.641	12.55	0.0	5.44	0.429
391	23.3663994	30.7953633	2.52	2.441	1.48	2.549	4.37	0.613	14.52	0.185	7.32	0.024	19.03	2.428
392	23.5688082	30.8649504	8.77	1.527	7.0	1.287	7.721	0.591	18.912	0.267	224.65	0.15	214.1	0.874
393	23.3814602	30.7914239	–99.0	–99.0	–99.0	–99.0	0.48	1.192	5.98	2.189	0.51	0.002	0.552	0.597
394	23.2177947	30.8619643	0.032	0.507	0.043	0.43	0.104	0.804	0.204	0.305	0.3	0.0	0.038	0.166

Table 3. continued.

Num.	RA (J2000)	Dec (J2000)	3.6 μm		4.5 μm		5.8 μm		8.0 μm		24 μm		Hα	
	(°)	(°)	F_ν (mJy)	δr	F_ν (mJy)	δr	F_ν (mJy)	δr	F_ν (mJy)	δr	F_ν (mJy)	δr	F (10^{-14} erg s^{-1})	δr
395	23.3784711	30.8173116	1.42	0.538	1.27	0.618	0.9	0.858	1.32	0.934	0.45	0.003	–99.0	–99.0
396	23.51218	30.8572721	0.5	2.392	0.13	0.738	1.57	0.313	13.36	1.906	7.46	0.007	50.09	0.349
397	23.4574031	30.8614626	0.118	2.448	0.161	1.895	0.15	0.764	1.75	1.148	1.13	0.052	11.474	0.803
398	23.5458523	30.8079254	0.11	2.147	–99.0	–99.0	–99.0	–99.0	–99.0	–99.0	15.57	0.848	–99.0	–99.0
399	23.6715006	30.8513604	–99.0	–99.0	–99.0	–99.0	–99.0	–99.0	–99.0	–99.0	0.75	0.001	–99.0	–99.0
400	23.5263124	30.8606255	–99.0	–99.0	0.09	2.719	1.646	1.588	3.841	0.876	5.19	0.033	8.74	2.26
401	23.4338307	30.8099453	0.42	0.377	0.22	0.316	1.81	0.49	4.591	0.373	4.91	0.02	3.16	0.142
402	23.55695	30.7896318	0.54	2.435	0.11	1.751	2.128	0.767	4.974	1.253	7.48	0.144	3.002	0.59
403	23.4949754	30.7908804	0.23	1.15	0.12	1.155	0.89	1.118	2.897	1.125	2.13	0.173	0.79	1.676
404	23.3089648	30.8568698	0.08	0.558	0.1	0.515	0.33	0.578	1.22	0.534	2.79	0.033	–99.0	–99.0
405	23.3987872	30.8482912	0.418	1.341	0.334	0.872	1.296	0.526	3.325	0.286	5.256	0.048	16.669	1.013
406	23.6087753	30.8166817	0.86	1.861	0.51	2.174	2.82	0.27	4.091	0.143	7.4	0.452	1.228	0.251
407	23.548629	30.8132312	0.1	1.895	0.066	2.115	–99.0	–99.0	–99.0	–99.0	2.85	0.179	–99.0	–99.0
408	23.3052668	30.8426466	0.34	1.057	0.23	0.655	1.94	0.651	7.54	1.407	6.27	0.017	13.91	0.292
409	23.3952365	30.8370405	0.24	0.936	0.13	1.057	–99.0	–99.0	3.34	2.97	9.0	0.015	11.1	2.414
410	23.4613394	30.7949125	–99.0	–99.0	–99.0	–99.0	–99.0	–99.0	–99.0	–99.0	1.59	0.003	–99.0	–99.0
411	23.4249291	30.7931596	0.93	0.691	0.58	0.628	5.52	0.686	5.086	1.031	15.48	0.132	5.864	0.312
412	23.4949753	30.8346301	0.36	0.562	0.32	0.516	0.22	0.482	1.84	0.785	1.84	0.001	0.314	2.053
413	23.3014687	30.821464	0.14	1.16	–99.0	–99.0	0.36	1.139	4.62	1.768	7.36	0.019	–99.0	–99.0
414	23.2957009	30.8095165	0.12	0.296	0.08	0.152	0.98	0.77	2.433	1.539	11.43	0.744	–99.0	–99.0
415	23.4019926	30.8439406	0.5	1.349	0.39	1.127	1.06	1.506	4.41	1.54	7.596	0.084	60.62	1.284
416	23.4841595	30.8511127	0.21	1.516	0.129	0.961	0.31	1.15	0.913	1.057	0.34	0.002	0.265	0.582
417	23.366927	30.8427976	0.054	1.423	0.063	1.383	0.087	0.883	0.267	0.669	0.75	0.001	–99.0	–99.0
418	23.2181081	30.8384177	0.24	1.441	0.17	0.961	0.56	0.534	1.58	0.643	7.24	0.033	1.57	0.729
419	23.4492321	30.8466044	0.52	0.091	0.34	0.399	1.01	2.326	–99.0	–99.0	4.96	0.042	31.62	2.827
420	23.5210173	30.8166038	–99.0	–99.0	–99.0	–99.0	1.14	1.911	4.995	0.037	3.34	0.129	–99.0	–99.0
421	23.1812805	30.8018275	–99.0	–99.0	0.06	1.459	0.16	1.266	0.57	1.309	3.93	0.033	0.73	2.044
422	23.4907269	30.7770533	–99.0	–99.0	–99.0	–99.0	2.286	1.997	7.231	2.274	1.236	0.37	2.971	1.111
423	23.4144609	30.7759326	–99.0	–99.0	–99.0	–99.0	–99.0	–99.0	–99.0	–99.0	0.64	0.001	–99.0	–99.0
424	23.6280097	30.8284288	–99.0	–99.0	–99.0	–99.0	0.33	0.524	1.41	0.894	1.288	0.01	0.37	0.124
425	23.3474003	30.8284719	0.134	1.964	0.099	1.606	0.434	0.921	0.944	0.896	3.049	0.073	0.356	0.475
426	23.4941016	30.8115477	1.637	0.432	1.98	0.432	5.577	0.661	80.06	1.543	82.0	0.115	9.615	0.505
427	23.495441	30.8197853	0.757	0.506	0.666	0.611	3.374	0.857	25.98	1.503	8.038	0.127	9.771	0.463
428	23.3024284	30.8107841	0.15	0.722	–99.0	–99.0	0.14	0.798	0.29	0.727	1.636	0.097	15.502	1.531
429	23.4907454	30.8176074	3.08	1.941	2.23	2.174	13.87	1.668	11.191	0.559	19.19	0.185	11.016	0.295
430	23.4626141	30.8213831	–99.0	–99.0	0.088	0.45	0.146	0.787	0.168	0.628	1.197	0.029	–99.0	–99.0
431	23.4990198	30.8227204	0.343	0.789	0.277	0.807	2.236	0.853	5.924	1.021	5.058	0.004	–99.0	–99.0
432	23.4840875	30.824481	–99.0	–99.0	–99.0	–99.0	0.29	0.75	1.173	0.998	0.47	0.001	0.125	0.68
433	23.3483471	30.8253958	–99.0	–99.0	–99.0	–99.0	0.21	1.746	0.85	0.886	0.42	0.022	–99.0	–99.0
434	23.5411217	30.8183276	0.35	1.125	0.1	1.116	0.44	0.539	5.944	1.288	0.947	0.296	–99.0	–99.0
435	23.3099436	30.8251711	0.34	2.647	–99.0	–99.0	–99.0	–99.0	0.63	1.862	0.692	0.027	–99.0	–99.0
436	23.5914998	30.8111663	1.69	1.447	1.1	1.375	24.74	1.399	12.172	1.879	48.87	0.276	25.02	2.509
437	23.6151254	30.8208454	0.076	1.288	0.061	1.187	0.392	0.726	1.709	1.013	0.71	0.003	0.218	0.398
438	23.5599839	30.8089016	–99.0	–99.0	–99.0	–99.0	18.0	2.567	40.29	2.944	24.17	0.846	–99.0	–99.0
439	23.4603869	30.8169624	–99.0	–99.0	0.18	2.645	0.191	1.75	0.329	0.879	0.65	0.002	0.236	2.077
440	23.4016647	30.8116122	1.95	2.072	1.27	1.429	10.93	1.73	3.673	0.651	18.29	0.018	8.97	2.965
441	23.5137195	30.8859375	0.25	0.249	0.12	0.356	0.7	0.795	2.74	1.114	2.13	0.001	3.89	0.234
442	23.3191453	30.7913209	0.27	0.298	0.23	0.016	0.92	0.462	1.5	0.687	2.59	0.159	–99.0	–99.0
443	23.6645764	30.800065	–99.0	–99.0	0.03	0.296	0.23	0.284	0.72	0.355	1.789	0.089	–99.0	–99.0
444	23.5321019	30.8054253	0.45	2.045	0.38	2.109	0.75	1.232	1.485	0.887	1.0	0.003	–99.0	–99.0
445	23.6687348	30.8042817	–99.0	–99.0	–99.0	–99.0	1.271	2.227	0.82	1.426	0.98	0.25	6.706	0.584
446	23.4427185	30.8706901	0.23	0.447	0.18	0.466	0.95	0.665	3.18	0.59	6.94	0.024	5.24	0.255
447	23.5480965	31.0422525	–99.0	–99.0	–99.0	–99.0	0.073	0.709	0.224	0.287	0.3	0.001	–99.0	–99.0
448	23.4258971	30.7960688	0.216	1.368	0.178	1.406	1.129	0.932	2.912	0.933	4.284	0.124	–99.0	–99.0
449	23.4382839	30.7943784	–99.0	–99.0	–99.0	–99.0	1.08	2.703	–99.0	–99.0	6.97	0.059	–99.0	–99.0
450	23.5158707	30.9160971	0.6	1.767	0.37	1.863	1.72	1.426	17.05	1.468	7.72	0.053	27.429	1.73
451	23.3907915	30.7865325	0.19	1.068	0.11	0.819	0.99	0.653	8.51	0.686	2.94	0.002	14.83	1.579
452	23.5494827	30.785238	–99.0	–99.0	–99.0	–99.0	1.82	1.353	12.783	0.828	1.02	0.071	–99.0	–99.0
453	23.5188945	30.9070833	0.14	2.792	–99.0	–99.0	0.33	1.566	–99.0	–99.0	0.51	0.156	–99.0	–99.0
454	23.5956995	30.7820692	0.31	2.004	0.23	1.713	0.59	0.941	3.23	0.994	1.84	0.046	13.87	1.38
455	23.569164	30.7810313	0.19	2.3	0.06	2.924	10.95	0.431	1.855	0.913	6.25	0.231	–99.0	–99.0
456	23.4667165	30.7878456	0.44	2.537	0.37	2.611	0.63	1.829	3.26	1.916	1.441	0.019	8.69	0.34
457	23.5455554	30.7764174	–99.0	–99.0	0.86	2.951	1.59	1.489	12.02	1.761	6.62	0.019	8.298	0.105
458	23.5743777	30.8800705	0.16	0.118	0.07	0.479	0.63	0.553	4.65	0.582	4.377	0.026	0.9	0.275
459	23.4482496	30.9017202	–99.0	–99.0	–99.0	–99.0	0.25	1.414	2.12	1.185	0.52	0.002	2.63	1.226
460	23.3412458	30.7959015	0.38	2.063	0.3	1.901	2.34	2.148	–99.0	–99.0	6.75	0.021	11.23	1.242

Table 3. continued.

Num.	RA (J2000)	Dec (J2000)	3.6 μm		4.5 μm		5.8 μm		8.0 μm		24 μm		Hα	
	(°)	(°)	F_ν (mJy)	δr	F_ν (mJy)	δr	F_ν (mJy)	δr	F_ν (mJy)	δr	F_ν (mJy)	δr	F (10^{-14} erg s^{-1})	δr
461	23.5113866	30.8281243	0.47	2.435	0.14	0.677	0.086	0.472	2.55	2.504	1.29	0.055	0.253	2.035
462	23.5086251	30.8769465	0.21	0.566	0.1	0.485	0.27	0.476	2.84	0.514	0.69	0.081	–99.0	–99.0
463	23.3723671	30.8372253	0.499	0.765	0.287	1.38	0.09	1.641	1.84	1.135	0.42	0.116	0.8	1.02
464	23.6725383	30.786192	0.22	2.399	–99.0	–99.0	4.71	2.752	21.68	2.751	9.34	0.0	–99.0	–99.0
465	23.6007448	30.9138192	0.3	1.951	0.16	2.19	0.32	0.695	2.12	0.316	4.74	0.045	12.847	1.013
466	23.6532015	30.8682463	0.25	2.433	0.17	1.909	–99.0	–99.0	0.27	0.712	0.32	0.112	–99.0	–99.0
467	23.4657954	30.8688818	0.159	0.468	0.1	0.524	0.102	0.57	0.44	0.523	0.71	0.001	–99.0	–99.0
468	23.4579162	30.8824059	–99.0	–99.0	–99.0	–99.0	0.56	0.874	1.183	1.022	1.351	0.17	2.424	0.128
469	23.511233	30.8969572	0.28	1.414	0.17	1.425	0.13	0.558	0.977	0.64	1.15	0.001	0.044	2.637
470	23.2262503	30.8403702	0.04	1.501	0.047	1.448	0.242	1.217	0.83	0.583	1.84	0.002	6.447	1.539
471	23.5508254	30.8873415	1.84	0.428	1.17	0.51	0.86	0.559	0.73	0.564	0.48	0.085	–99.0	–99.0
472	23.5687729	30.8724925	0.69	2.845	0.255	0.602	2.77	0.832	6.56	0.745	36.11	0.031	–99.0	–99.0
473	23.6242498	30.9545948	1.68	2.537	0.87	2.502	6.21	1.865	42.24	0.942	67.42	0.064	92.56	1.218
474	23.5446277	31.054989	0.14	1.366	0.03	0.722	0.21	1.143	1.53	1.486	1.89	0.002	1.92	1.437
475	23.6807839	30.8024574	–99.0	–99.0	0.05	0.144	0.111	0.406	0.252	0.398	1.13	0.003	0.074	2.947
476	23.5889273	30.9065559	0.47	1.073	0.3	1.382	0.89	0.623	3.041	0.495	1.87	0.002	5.4	0.669
477	23.5140251	30.9686822	0.032	1.334	0.02	1.396	0.158	1.37	0.45	1.225	1.89	0.156	–99.0	–99.0
478	23.4321075	31.0353863	0.31	1.995	0.41	0.839	0.8	0.788	2.2	0.588	17.38	0.007	–99.0	–99.0
479	23.3184214	30.8807218	8.25	1.224	13.58	1.228	48.73	1.55	154.18	1.415	1848.38	0.0	161.77	1.006
480	23.4796581	30.9040231	0.08	2.531	0.074	1.812	0.277	0.42	0.966	0.08	0.85	0.066	0.58	1.259
481	23.549858	30.9756237	–99.0	–99.0	0.033	0.786	0.106	0.639	0.11	0.789	0.21	0.156	–99.0	–99.0
482	23.4542822	30.8570718	–99.0	–99.0	0.37	1.38	1.21	1.655	4.08	1.438	3.79	0.001	–99.0	–99.0
483	23.5129404	31.0331657	0.14	1.093	0.078	1.101	0.116	0.982	0.072	1.052	0.31	0.124	–99.0	–99.0
484	23.5609306	30.8959397	0.79	1.157	0.34	1.324	0.8	1.116	4.38	1.324	1.38	0.002	2.27	2.53
485	23.4593204	30.9719328	0.044	1.653	0.08	0.654	0.18	0.8	0.58	0.804	0.21	0.001	–99.0	–99.0
486	23.5148818	30.802739	–99.0	–99.0	0.48	2.696	4.99	0.859	3.182	0.985	7.92	0.023	–99.0	–99.0
487	23.5609434	30.7914915	0.251	0.868	0.268	0.89	0.317	0.985	0.334	1.118	4.875	2.229	–99.0	–99.0
488	23.6074669	30.9219251	1.56	0.319	1.93	0.377	2.26	0.377	2.99	0.429	2.6	0.001	–99.0	–99.0
489	23.5117669	31.0475477	0.13	0.457	0.11	0.753	0.097	0.691	0.276	0.804	0.64	0.002	–99.0	–99.0
490	23.6169793	30.9334413	0.2	1.737	0.25	0.881	0.52	1.391	1.85	1.083	7.33	0.018	–99.0	–99.0
491	23.5572718	31.0671411	0.08	0.263	0.09	0.662	0.21	0.269	1.03	0.619	2.36	0.033	2.45	0.303
492	23.5794776	30.8082864	–99.0	–99.0	–99.0	–99.0	–99.0	–99.0	–99.0	–99.0	55.84	0.072	–99.0	–99.0
493	23.3667182	31.0053067	0.154	0.308	0.123	0.762	0.407	1.346	0.78	1.141	1.06	0.001	6.898	0.054
494	23.3163336	30.9456245	1.18	1.565	1.53	1.243	–99.0	–99.0	–99.0	–99.0	46.92	0.005	56.046	0.362
495	23.4443025	30.8555902	0.98	1.781	0.65	2.335	0.54	2.765	1.07	1.708	0.74	0.001	1.09	1.571
496	23.6318909	30.9570706	0.71	0.891	0.65	0.764	1.446	0.521	3.469	0.395	5.024	0.091	–99.0	–99.0
497	23.5328498	31.0325562	0.027	0.123	0.06	0.874	0.191	0.794	0.17	0.754	1.32	0.001	–99.0	–99.0
498	23.4575392	30.878299	3.58	0.95	3.6	0.806	3.39	0.831	3.73	0.753	1.31	0.003	–99.0	–99.0
499	23.5926926	30.945429	0.53	0.597	0.32	0.548	0.09	0.103	1.51	0.483	0.36	0.001	–99.0	–99.0
500	23.340851	30.9226573	0.27	0.799	0.27	0.51	–99.0	–99.0	0.49	0.375	1.89	0.001	–99.0	–99.0
501	23.5026165	30.7913101	0.36	2.145	0.08	2.057	0.78	1.265	2.432	1.272	0.4	0.0	–99.0	–99.0
502	23.5112777	30.8120784	–99.0	–99.0	–99.0	–99.0	–99.0	–99.0	6.05	1.368	1.59	0.07	0.212	2.052
503	23.5105026	30.9696764	0.212	0.391	0.187	0.461	1.156	0.406	2.851	0.413	5.448	0.033	2.363	0.523
504	23.5110998	30.918498	0.14	1.977	0.187	0.721	0.393	0.594	1.308	1.555	1.168	0.124	–99.0	–99.0
505	23.3607924	30.9540566	0.54	0.76	0.58	0.831	0.43	0.81	0.8	0.801	1.75	0.002	0.56	2.891
506	23.4756051	30.9593013	0.012	0.911	0.023	0.845	0.179	0.842	0.36	0.622	0.2	0.147	–99.0	–99.0
507	23.5273085	30.815905	0.48	1.315	0.29	1.214	1.42	1.729	5.51	1.819	8.93	0.194	31.03	1.072
508	23.561598	30.9585245	0.35	0.9	0.26	0.881	0.284	0.739	0.75	0.859	0.34	0.001	–99.0	–99.0
509	23.4573301	30.942474	0.08	0.852	0.1	0.865	0.188	1.013	0.23	0.779	0.51	0.089	–99.0	–99.0
510	23.3103693	30.8603881	0.149	1.476	0.112	1.256	0.679	0.919	1.936	1.08	1.321	0.352	8.289	0.738
511	23.5826128	30.816185	–99.0	–99.0	0.31	0.297	16.07	0.502	3.436	1.159	23.32	0.046	45.95	0.643
512	23.50917	30.8411049	0.77	1.973	0.49	1.56	1.65	0.91	7.34	1.051	3.89	0.0	5.11	0.429
513	23.3850146	31.0214745	0.042	0.811	0.035	0.832	0.178	0.505	0.48	0.663	0.23	0.001	–99.0	–99.0
514	23.59976	30.9504538	–99.0	–99.0	–99.0	–99.0	0.2	2.861	2.96	2.027	2.99	0.065	14.55	1.43
515	23.5390177	30.9218105	0.379	0.419	0.483	0.405	0.56	0.406	0.79	0.506	0.35	0.001	–99.0	–99.0